



# 1 **CANOPS-GRB v1.0: a new Earth system model for simulating the** 2 **evolution of ocean-atmosphere chemistry over geologic timescales**

3 Kazumi Ozaki<sup>1,2</sup>, Devon B. Cole<sup>3</sup>, Christopher T. Reinhard<sup>2,3,4</sup>, and Eiichi Tajika<sup>5</sup>

4 <sup>1</sup>Department of Environmental Science, Toho University, Funabashi, Chiba 274-8510, Japan

5 <sup>2</sup>NASA Nexus for Exoplanet System Science (NExSS)

6 <sup>3</sup>School of Earth and Atmospheric Sciences, Georgia Institute of Technology, Atlanta, GA 30332, USA

7 <sup>4</sup>NASA Interdisciplinary Consortia for Astrobiology Research (ICAR), Alternative Earths Team, Riverside, CA, USA

8 <sup>5</sup>Department of Earth and Planetary Science, The University of Tokyo, Bunkyo-ku Tokyo 113-0033, Japan

9 *Correspondence to:* Kazumi Ozaki (kazumi.ozaki@sci.toho-u.ac.jp)

## 10 **Abstract**

11 A new version of the Earth system model of intermediate complexity (CANOPS-GRB) was developed for use  
12 in quantitatively assessing the dynamics and stability of atmospheric and oceanic chemistry over geologic  
13 timescales. The new release is designed to represent the coupled major element cycles of C, N, P, O, and S,  
14 as well as the global redox budget (GRB) in Earth's exogenic (ocean-atmosphere-crust) system, using a  
15 process-based approach. This framework provides a mechanistic model of the evolution of atmospheric and  
16 oceanic O<sub>2</sub> levels on geologic timescales and enables comparison with a wide variety of geological records to  
17 further constrain the processes driving Earth's oxygenation. A complete detailed description of the resulting  
18 Earth system model and its new features are provided. The performance of CANOPS-GRB is then evaluated  
19 by comparing a steady-state simulation under present-day conditions with a comprehensive set of oceanic data  
20 and existing global estimates of bio-element cycling. The dynamic response of the model is also examined by  
21 varying phosphorus availability in the exogenic system. CANOPS-GRB reliably simulates the short- and long-  
22 term evolution of the coupled C-N-P-O<sub>2</sub>-S biogeochemical cycles and is generally applicable across any period  
23 of Earth's history given suitable modifications to boundary conditions and forcing regime. The simple and  
24 adaptable design of the model also makes it useful to interrogate a wide range of problems related to Earth's  
25 oxygenation history and Earth-like exoplanets more broadly. The model source code is available on GitHub,  
26 and represents a unique community tool for investigating the dynamics and stability of atmospheric and  
27 oceanic chemistry on long timescales.



## 28 **Short summary:**

29 A new biogeochemical model (CANOPS-GRB v1.0) for assessing the redox stability and dynamics of the  
30 ocean-atmosphere system on geologic timescales has been developed. In this paper, we present a full  
31 description of the model and its performance. CANOPS-GRB is a useful tool for understanding the factors  
32 regulating atmospheric O<sub>2</sub> levels and has the potential to greatly refine our current understanding of Earth's  
33 oxygenation history.

## 34 **1 Introduction**

35 A quarter century has passed since the first discovery of exoplanets (Mayor and Queloz, 1995). In the next  
36 quarter century, a full-scale search for signs of life—biosignatures—on Earth-like exoplanets is one of the  
37 primary objectives of the next generation of exoplanetary observational surveys (National Academies of  
38 Sciences and Medicine, 2019; The LUVOIR Team, 2019). The definition of biosignatures includes a variety  
39 of signatures that require biological activity for their origin (Des Marais et al., 2002; Lovelock, 1965; National  
40 Academies of Sciences and Medicine, 2019; Sagan et al., 1993; Schwieterman et al., 2018), but atmospheric  
41 composition has received the most interdisciplinary attention since the dawn of the search for life beyond our  
42 own planet (Hitchcock and Lovelock, 1967; Lovelock, 1972, 1965, 1975; Sagan et al., 1993) because of its  
43 potential for remote detectability. Indeed, it is likely that deciphering of exoplanetary atmospheric composition  
44 based on spectroscopic information will, at least for the foreseeable future, be our only promising means for  
45 life detection beyond our solar system. However, the detection of atmospheric composition cannot  
46 immediately answer the question of the presence or absence of a surface biosphere because significant gaps  
47 remain in our understanding of the relationships between atmospheric composition and biological activity  
48 occurring at the surface on life-bearing exoplanets. Many of these gaps arise from a lack of robust theoretical  
49 and quantitative frameworks for the emergence and maintenance of remotely detectable atmospheric  
50 biosignatures in the context of planetary biogeochemistry.

51

52 It is also important to emphasize that the abundance of atmospheric biosignature gases of living planets will  
53 evolve via an intimate interaction between life and global biogeochemical cycles of bio-essential elements  
54 across a range of timescales. Indeed, the abundances of biosignature gases such as molecular oxygen (O<sub>2</sub>) and



55 methane (CH<sub>4</sub>) in Earth's atmosphere have evolved dramatically through coevolutionary interaction with  
56 Earth's biosphere for nearly 4 billion years—through remarkable fluctuations in atmospheric chemistry and  
57 climate (Catling and Kasting, 2017; Catling and Zahnle, 2020; Lyons et al., 2014). To the extent that the  
58 coupled evolution of life and the atmosphere is a universal property of life-bearing planets that maintain robust  
59 atmospheric biosignatures, the construction of a biogeochemical framework for diagnosing atmospheric  
60 biosignatures should be a subject of urgent interdisciplinary interest.

61

62 Establishing a mechanistic understanding of our own planet's evolutionary history is also an important  
63 milestone for the construction of a search strategy for life beyond our solar system, as it provides the first step  
64 towards understanding how remotely detectable biosignatures emerge and are maintained on a planetary scale.  
65 While numerous atmospheric biosignature gases have been proposed, the most promising candidates have  
66 been 'redox-based' species, such as O<sub>2</sub>, ozone (O<sub>3</sub>), and CH<sub>4</sub> (Krissansen-Totton et al., 2018; Meadows, 2017;  
67 Meadows et al., 2018; Reinhard et al., 2017a). In particular, O<sub>2</sub> is of great interest to astrobiologists because  
68 of its crucial role in metabolism on Earth. Thus, a considerable effort has been devoted over recent decades to  
69 quantitatively and mechanistically understand Earth's oxygenation history. In particular, a recent surge in the  
70 generation of empirical records for Earth's redox evolution has yielded substantial progress in our 'broad  
71 stroke' understanding of Earth's oxygenation history and has shaped our view of biological evolution (Kump,  
72 2008; Lyons et al., 2014). One of the intriguing insights obtained from the accumulated geochemical records  
73 is that atmospheric O<sub>2</sub> levels might have evolved more dynamically than previously thought—our current  
74 paradigm of Earth's oxygenation history suggests that atmospheric O<sub>2</sub> levels may have risen and then  
75 plummeted during the early Proterozoic, then remained low (probably <10% of the present atmospheric level;  
76 PAL) for much of the ~1 billion years leading up to the catastrophic climate system perturbations and the  
77 initial diversification of complex life during the late Proterozoic.

78

79 The possibility of low but 'post-biotic' atmospheric O<sub>2</sub> levels during the mid-Proterozoic has important  
80 ramifications not only for our basic theoretical understanding of long-term O<sub>2</sub> cycle stability on a planet with  
81 biological O<sub>2</sub> production, but also for biosignature detectability (Reinhard et al., 2017a). However, our  
82 quantitative and mechanistic understanding of the Earth's O<sub>2</sub> cycle in deep time is still rudimentary at present.



83 For example, one possible explanation for low atmospheric O<sub>2</sub> levels during the mid-Proterozoic is simply a  
84 less active or smaller biosphere (Crockford et al., 2018; Derry, 2015; Laakso and Schrag, 2014; Ozaki et al.,  
85 2019a). However, mechanisms for regulating biotic O<sub>2</sub> generation rates and stabilizing atmospheric O<sub>2</sub> levels  
86 at low levels on billion-year timescales remain obscure. As a result, the level of atmospheric O<sub>2</sub> and its stability  
87 during the early-mid Proterozoic are the subject of vigorous debate (Bellefroid et al., 2018; Canfield et al.,  
88 2018; Cole et al., 2016; Planavsky et al., 2018; Planavsky et al., 2016; Tang et al., 2016; Zhang et al., 2016).  
89 Perhaps even more importantly, a relatively rudimentary quantitative framework for probing the dynamics  
90 and stability of the oxygen cycle leads to the imprecision of geochemical reconstructions of ocean-atmosphere  
91 O<sub>2</sub> levels.

92

93 Planetary atmospheric O<sub>2</sub> levels are governed by a kinetic balance between sources and sinks. Feedback arises  
94 because the response of source/sink fluxes to changes in atmospheric O<sub>2</sub> levels is intimately interrelated to  
95 each other. Since the biogeochemical cycles of C, N, P, and S exert fundamental control on the redox budget  
96 through non-linear interactions and feedback mechanisms, a mechanistic understanding of these  
97 biogeochemical cycles is critical for understanding Earth's O<sub>2</sub> cycle. However, the wide range of timescales  
98 that characterize C, N, P, O<sub>2</sub> and S cycling through the reservoirs of the Earth system makes it difficult to fully  
99 resolve the mechanisms governing the dynamics and stability of atmospheric O<sub>2</sub> levels from geologic records.  
100 From this vantage, developing new quantitative tools that can explore biogeochemical cycles under conditions  
101 very different from those of the present Earth is an important pursuit.

102

103 This study is motivated by the conviction that an ensemble of 'open' Earth system modeling frameworks with  
104 explicit and flexible representation of the coupled C-N-P-O<sub>2</sub>-S biogeochemical cycles will ultimately be  
105 required to fully understand the dynamics and stability of Earth's O<sub>2</sub> cycle and its controlling factors. In  
106 particular, a coherent mechanistic framework for understanding the global redox (O<sub>2</sub>) budget (GRB) is critical  
107 for filling remaining gaps in our understanding of Earth's oxygenation history and the cause-and-effect  
108 relationships with an evolving biosphere. Here, we develop a new Earth system model, named CANOPS-  
109 GRB, which implements the coupled biogeochemical cycles of C-N-P-O<sub>2</sub>-S within the Earth's surface system  
110 (ocean-atmosphere-crust). The model design (such as the complexity of the processes and spatial-temporal



111 resolution of the model) is constrained by the requirement of simulation length (>100 million years) and actual  
112 model run-time. A lack of understanding of biogeochemistry in deep-time and availability and quality of  
113 geologic records also limit the model structure. With this in mind, we aim for a comprehensive, simple, yet  
114 realistic representation of biogeochemical processes in the Earth system, yielding a unique tool for  
115 investigating coupled biogeochemical cycles within the Earth system over a wide range of time scales. We  
116 have placed particular emphasis on the development of a global redox budget in the ocean-atmosphere-crust  
117 system given its importance in the secular evolution of atmospheric O<sub>2</sub> levels. CANOPS-GRB is an initial  
118 step towards developing the first large-scale biogeochemistry evolution model suited for the wide range of  
119 redox conditions, including explicit consideration of the coupled C-N-P-O<sub>2</sub>-S cycles and the major biogenic  
120 gases in planetary atmospheres (O<sub>2</sub> and CH<sub>4</sub>).



## 121 **2 Model description**

122 Here we present a full description of a new version of the Earth system model CANOPS—CANOPS-GRB—  
123 which is designed to facilitate simulation for a wide range of biogeochemical conditions so as to permit  
124 quantitative examination of evolving ocean-atmosphere chemistry throughout Earth’s history. Below we first  
125 describe the concept of model design (Sect. 2.1). Next, we describe the overall structure of the model and the  
126 basic design of global biogeochemical cycles (Sect. 2.2 and 2.3). That is followed by a detailed description of  
127 each sub-model.

### 128 **2.1 CANOPS-GRB in the hierarchy of biogeochemical models**

129 A full understanding of Earth’s evolving O<sub>2</sub> cycle requires a quantitative framework that includes mechanistic  
130 links between biological metabolism, ocean-atmosphere chemistry, and geologic processes. Such a framework  
131 must also represent the feedbacks between ocean-atmosphere redox state and biogeochemical cycles of redox-  
132 dependent bio-essential elements. Over recent decades, considerable progress has been made in quantifying  
133 the feedbacks between atmospheric O<sub>2</sub> levels and the coupled C-N-P-O<sub>2</sub>-S biogeochemical cycles over  
134 geological timescales (Belcher and McElwain, 2008; Berner, 2004b; Betts and Holland, 1991; Bolton et al.,  
135 2006; Colman et al., 2000; Holland, 1978; Lasaga and Ohmoto, 2002; Slomp and Van Cappellen, 2007; Van  
136 Cappellen and Ingall, 1994). Refinements to our understanding of mechanisms regulating Earth’s surface  
137 redox state have been implemented in low-resolution box models where the ocean-atmosphere system is  
138 expressed by a few boxes (Alcott et al., 2019; Bergman et al., 2004; Claire et al., 2006; Goldblatt et al., 2006;  
139 Handoh and Lenton, 2003; Laakso and Schrag, 2014; Lenton and Watson, 2000a, b; Petsch and Berner, 1998;  
140 Van Cappellen and Ingall, 1996). These models offer insights into basic system behavior and can illuminate  
141 the fundamental mechanisms that exert the most leverage on biogeochemical cycles because of their simplicity,  
142 transparency and low computational demands. However, these model architectures also have important  
143 quantitative limitations. For example, with low spatial resolution the modeler needs to assume reasonable (but  
144 *a priori*) relationships relating to internal biogeochemical cycles in the system. For instance, because of a lack  
145 of high vertical resolution, oceanic box models (Knox and McElroy, 1984; Sarmiento and Toggweiler, 1984;  
146 Siegenthaler and Wenk, 1984) usually overestimate the sensitivity of atmospheric CO<sub>2</sub> levels to biological  
147 activity at high-latitude surface ocean relative to projections by general circulation models (Archer et al.,



148 2000). Oceanic biogeochemical cycles and chemical distributions are also characterized by strong vertical and  
149 horizontal heterogeneities, which have the potential to affect the strength of feedback processes (Ozaki et al.,  
150 2011). In other words, the low-resolution box modeling approach might overlook the strength and response  
151 of the internal feedback loops. Thus, the development of an ocean model with high resolution of ocean interior  
152 and reliable representation of water circulation is required to investigate the mechanisms controlling  
153 atmospheric O<sub>2</sub> levels under conditions very different from those of the modern Earth.

154

155 In the last decade, comprehensive Earth system models of intermediate complexity (EMICs) have also been  
156 developed and extended to include ocean sediments and global C cycling (Lord et al., 2016; Ridgwell and  
157 Hargreaves, 2007). Such models can be integrated over tens of thousands of years, allowing experimentation  
158 with hypothetical dynamics of global biogeochemical cycles in the geological past (Olson et al., 2016;  
159 Reinhard et al., 2020). However, a key weakness of existing EMICs is the need to parameterize (or ignore)  
160 boundary (input/output) fluxes—either due to the computational expense of explicitly specifying boundary  
161 conditions or due to poorly constrained parameterizations. For example, the oceanic P cycle is usually treated  
162 as a closed system, limiting the model’s applicability to timescales less than the oceanic P residence time  
163 (~15–20 kyr). Further, boundary conditions such as continental configuration and oceanic bathymetry are  
164 variable or poorly constrained in deep time and the use of highly complex models is difficult to justify the  
165 computational cost. Finally, exploration of hypotheses concerning the biogeochemical dynamics in deep time  
166 often require large model ensembles across broad parameter space given the scope of uncertainty. This makes  
167 the computational cost of EMICs intractable at present for many key questions.

168

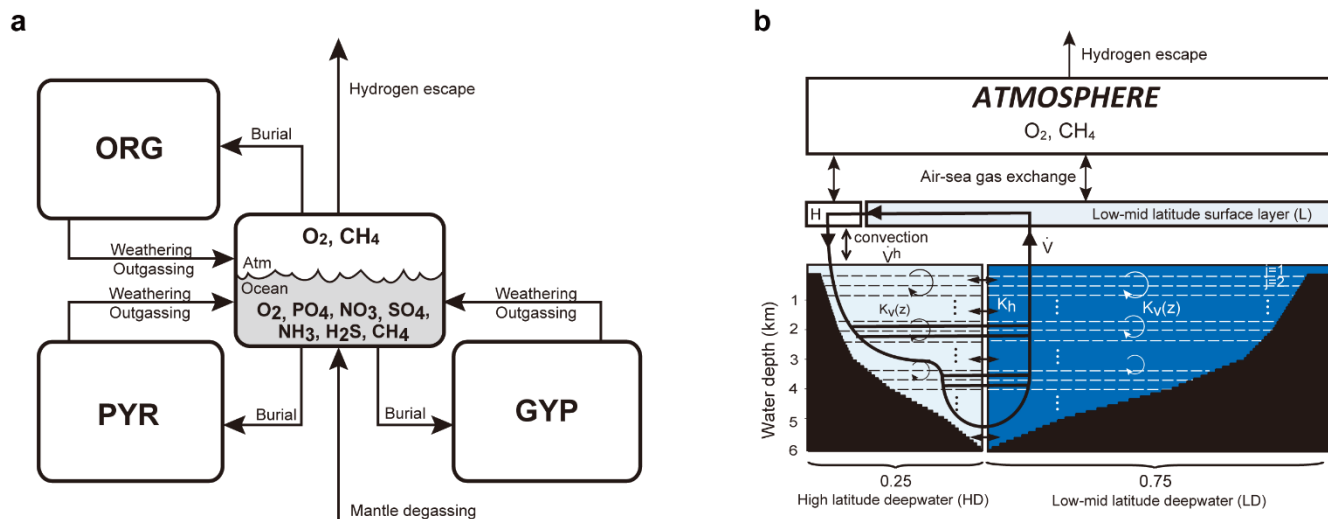
169 The CANOPS-GRB model is designed to capture the major components of Earth system biogeochemistry on  
170 timescales longer than a millennium, but is simple enough to allow for runs on the order of a billion model  
171 years. The model structure is also designed so that the model captures the essential biogeochemical processes  
172 regulating the global O<sub>2</sub> budget, while keeping the calculation cost as moderate as possible. For example, the  
173 simple relationships of biogeochemical transport processes at the interface of Earth system (hydrogen escape  
174 to space, early diagenesis in marine sediments, and weathering) are employed based on the systematic  
175 application of 1-D models in previous studies (Bolton et al., 2006; Claire et al., 2006; Daines et al., 2017;



176 Middelburg et al., 1997; Wallmann, 2003a), providing a powerful, computationally efficient means for  
177 exploring the Earth system under a wide range of conditions. The resultant CANOPS-GRB model can be run  
178 on a standard personal computer on a single CPU with an efficiency of approximately 6 million model years  
179 per CPU hour. In other words, model runs in excess of  $10^9$  model years are tractable with modest wall times  
180 (approximately 7 days). The model is thus not as efficient as simple box models, but is highly efficient relative  
181 to EMICs, making sensitivity experiments and exploration of larger parameter space over a billion years  
182 feasible, particularly with implementation on a high-performance computing cluster (see Cole et al., 2022).  
183 CANOPS-GRB thus occupies a unique position within the hierarchy of global biogeochemical cycle models,  
184 rendering it a useful tool for the development of more comprehensive, low- to intermediate-complexity models  
185 of Earth system on very long timescales.

## 186 **2.2 Overall model structure**

187 The overall structure of the model is shown in Fig. 1. The model consists of ocean, atmosphere and  
188 sedimentary reservoirs. The core of the model is an ocean model, comprising a high-resolution 1-D  
189 intermediate-complexity box model of the global ocean (Sect. 2.4). The ocean model is coupled to a  
190 parameterized marine sediment module (Sect. 2.4.4) and a one box model of the atmosphere (Sect. 2.6). The  
191 atmospheric model includes  $O_2$  and  $CH_4$  as chemical components, and abundances of these molecules are  
192 calculated based on the mass balance between sources and sinks (e.g., biogenic fluxes of  $O_2$  and  $CH_4$  from the  
193 ecosystems and photochemical reactions). The net air-sea gas exchange of chemical species ( $O_2$ ,  $H_2S$ ,  $NH_3$   
194 and  $CH_4$ ) is quantified according to the stagnant film model (Kharecha et al., 2005; Liss and Slater, 1974)  
195 (Sect. 2.4.5). The ocean and atmosphere models are embedded in a ‘rock cycle’ model that simulates the  
196 evolution of sedimentary reservoir sizes on geologic timescales (Sect. 2.5). Three sedimentary reservoirs  
197 (organic carbon, *ORG*; pyrite sulfur, *PYR*; and gypsum sulfur, *GYP*) are considered in the CANOPS-GRB  
198 model. These reservoirs interact with the ocean-atmosphere system through weathering, outgassing, and burial.  
199



200

201 **Figure 1** CANOPS-GRB model configuration. (a) The schematic of material cycles in the surface (ocean-  
 202 atmosphere-crust) system. Three sedimentary reservoirs, organic carbon (*ORG*), pyrite sulfur (*PYR*), and  
 203 gypsum sulfur (*GYP*), are considered. Sedimentary reservoirs interact with the ocean-atmosphere system via  
 204 weathering, volcanic degassing, and burial. No interaction with the mantle is included, except for the input of  
 205 reduced gases from the mantle. Total mass of sulfur is conserved in the surface system. (b) Schematic of ocean  
 206 and atmosphere modules. “L” and “H” denote the low-mid latitude mixed surface layer and high-latitude  
 207 surface layer, respectively. An ocean area of 10% is assumed for H. River flux for each region is proportional  
 208 to the areal fraction. Ocean interior is divided into two sectors, high-latitude deep water (HD) and low-mid  
 209 latitude deep water (LD), which are vertically resolved. The area of HD is 25% of the whole ocean. The deep  
 210 overturning circulation,  $\dot{V}$ , equals the poleward flow in the model surface layer (from L to H).  $K_v^l(z)$  and  
 211  $K_v^h(z)$  are the vertical eddy diffusion coefficients in the LD and HD regions, respectively.  $K_{hor}$  and  $\dot{V}_h$  are the  
 212 horizontal diffusion coefficient and polar convection, respectively. The black hatch represents the seafloor  
 213 topography assumed. The parameters regarding geometry and water transport are tabulated in Table 3.  
 214

215 The ocean model is a vertically resolved transport-reaction model of the global ocean, which was originally  
 216 developed by Ozaki et al. (2011) and Ozaki and Tajika (2013). The model consists of 122 boxes across two  
 217 regions; a low-mid latitude region and a high-latitude region (Fig. 1b). The ocean model describes water  
 218 transport processes as exchange fluxes between boxes and via eddy diffusion terms. More specifically, ocean  
 219 circulation is modelled as an advection-diffusion model of the global ocean—a general and robust scheme  
 220 that is capable of producing well-resolved modern profiles of circulation tracers using realistic parameter  
 221 values (the physical set up of the model can be found in Sect. 2.4.1 and 2.4.2). The biogeochemical sub-model  
 222 provides a mechanistic description of the marine biogeochemical cycles of C, P, N, O<sub>2</sub>, and S (Sect. 2.4.3).



223 This includes explicit representation of a variety of biogeochemical processes such as biological productivity  
 224 in the sunlit surface oceans, a series of respiration pathways and secondary redox reactions under oxic and  
 225 anoxic conditions (Sect. 2.4.3), and deposition, decomposition, and burial of biogenic materials in marine  
 226 sediments (Sect. 2.4.4), allowing a mechanistically based examination of biogeochemical processes. The suite  
 227 of metabolic reactions included in the model is listed in Table 1. Ocean biogeochemical tracers considered in  
 228 the CANOPS-GRB model are phosphate ( $\text{PO}_4^{3-}$ ), nitrate ( $\text{NO}_3^-$ ), total ammonia ( $\Sigma\text{NH}_3$ ), dissolved oxygen  
 229 ( $\text{O}_2$ ), sulfate ( $\text{SO}_4^{2-}$ ), total sulfide ( $\Sigma\text{H}_2\text{S}$ ), and methane ( $\text{CH}_4$ ). Ocean model performance was tested for the  
 230 modern-day ocean field observational data (Sect. 3). Simulation results were also compared to previously  
 231 published integrated global flux estimates.

232

233 Table 1: Biogeochemical reactions considered in the CANOPS-GRB model.

Process	Stoichiometry*	Reaction #
Ammonia assimilation	$\alpha\text{CO}_2 + \beta\text{NH}_4^+ + \text{H}_3\text{PO}_4 + \alpha\text{H}_2\text{O} \rightarrow \text{OM} + \alpha\text{O}_2$	R1
Nitrate assimilation	$\alpha\text{CO}_2 + \beta\text{NO}_3^- + \text{H}_3\text{PO}_4 + (\alpha + \beta)\text{H}_2\text{O} + 2\beta\text{H}^+ \rightarrow \text{OM} + (\alpha + 2\beta)\text{O}_2$	R2
Nitrogen fixation	$\text{N}_2 + 5\text{H}_2\text{O} \rightarrow 2\text{NH}_4^+ + 2\text{OH}^- + \frac{3}{2}\text{O}_2$	R3
Aerobic respiration	$\text{OM} + \alpha\text{O}_2 \rightarrow \alpha\text{CO}_2 + \beta\text{NH}_4^+ + \text{H}_3\text{PO}_4 + \alpha\text{H}_2\text{O}$	R4
Denitrification	$\text{OM} + \frac{4}{5}\alpha\text{NO}_3^- + \frac{4}{5}\alpha\text{H}^+ \rightarrow \alpha\text{CO}_2 + \beta\text{NH}_4^+ + \text{H}_3\text{PO}_4 + \frac{7}{5}\alpha\text{H}_2\text{O} + \frac{2}{5}\alpha\text{N}_2$	R5
Sulfate reduction	$\text{OM} + \frac{1}{2}\alpha\text{SO}_4^{2-} + \alpha\text{H}^+ \rightarrow \alpha\text{CO}_2 + \beta\text{NH}_4^+ + \text{H}_3\text{PO}_4 + \alpha\text{H}_2\text{O} + \frac{1}{2}\alpha\text{H}_2\text{S}$	R6
Methanogenesis	$\text{OM} \rightarrow \frac{1}{2}\alpha\text{CO}_2 + \frac{1}{2}\alpha\text{CH}_4 + \beta\text{NH}_4^+ + \text{H}_3\text{PO}_4$	R7
Nitrification	$\text{NH}_4^+ + 2\text{O}_2 \rightarrow \text{NO}_3^- + \text{H}_2\text{O} + 2\text{H}^+$	R8
Aerobic $\text{H}_2\text{S}$ oxidation†	$\Sigma\text{H}_2\text{S} + 2\text{O}_2 \rightarrow \text{SO}_4^{2-} + 2\text{H}^+$	R9
Aerobic $\text{CH}_4$ oxidation	$\text{CH}_4 + 2\text{O}_2 \rightarrow \text{CO}_2 + 2\text{H}_2\text{O}$	R10
Anaerobic $\text{CH}_4$ oxidation	$\text{CH}_4 + \text{SO}_4^{2-} \rightarrow \text{HS}^- + \text{HCO}_3^- + \text{H}_2\text{O}$	R11
Photooxidation of $\text{CH}_4$	$\text{CH}_4 + 2\text{O}_2 \rightarrow \text{CO}_2 + 2\text{H}_2\text{O}$	R12
Hydrogen escape to space	$\text{CH}_4 + \text{O}_2 \rightarrow \text{CO}_2 + 4\text{H} \uparrow$	R13

234 \*OM denotes organic matter,  $(\text{CH}_2\text{O})_\alpha(\text{NH}_4^+)_\beta\text{H}_3\text{PO}_4$

235 † $\Sigma\text{H}_2\text{S} = \text{H}_2\text{S} + \text{HS}^-$



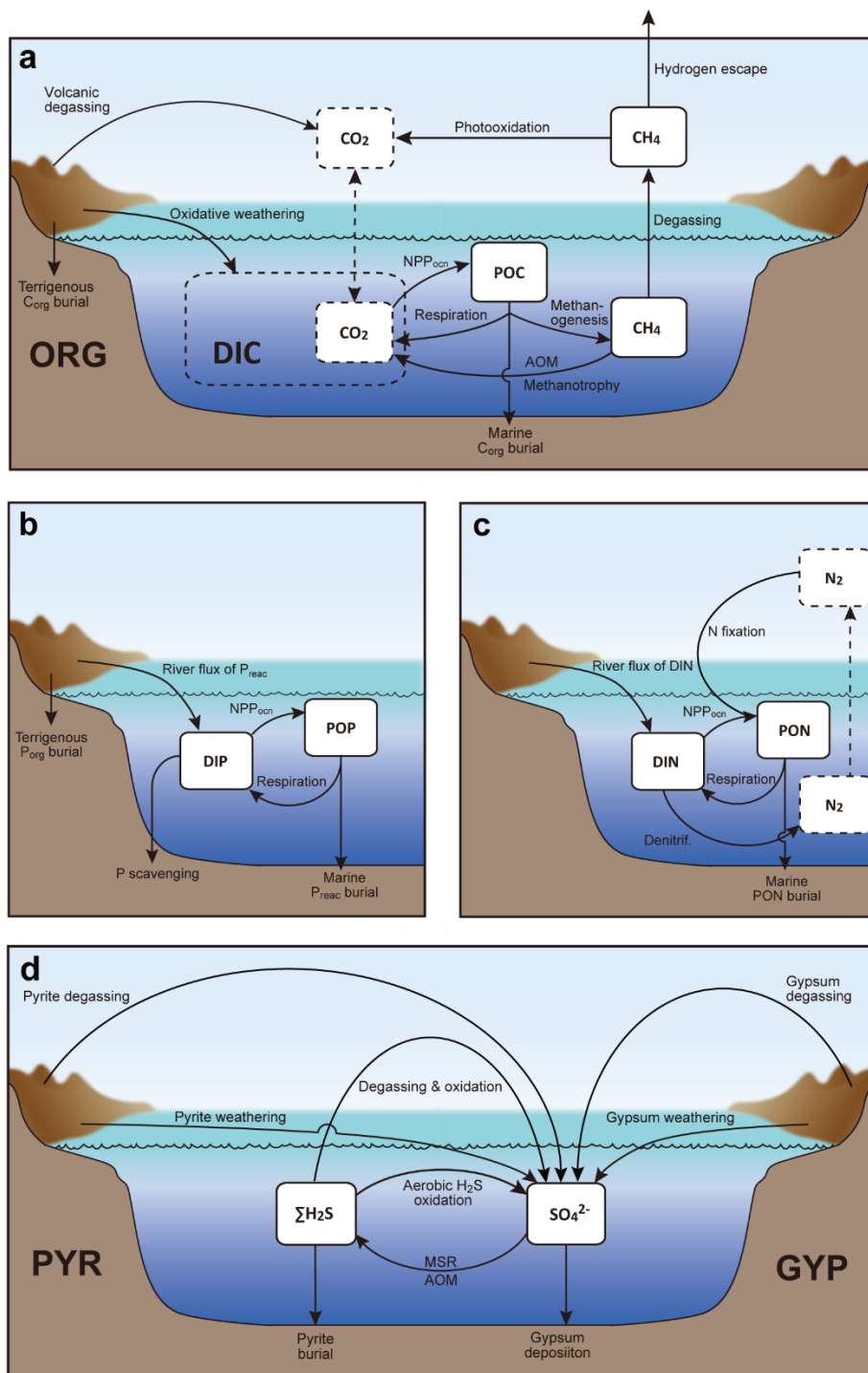
236

237 The CANOPS model has been extended and altered a number of times since first publication. The description  
238 of biogeochemical cycles in the original version of CANOPS (Ozaki and Tajika, 2013; Ozaki et al., 2011)  
239 does not include the S and CH<sub>4</sub> cycles because of their aims to investigate the conditions for the development  
240 of oceanic anoxia/euxinia on timescales less than a million years during the Phanerozoic. More recently, Ozaki  
241 et al. (2019) implemented an open system modeling approach for the global S and CH<sub>4</sub> cycles, enabling  
242 quantitative analysis of global redox budget for given atmospheric O<sub>2</sub> levels and crustal reservoir sizes. In this  
243 version of CANOPS atmospheric O<sub>2</sub> levels and sedimentary reservoirs are treated as boundary conditions  
244 because imposing them simplifies the model and significantly reduces computing time. However, this  
245 approach does not allow exploration of the dynamic behavior of atmospheric O<sub>2</sub> in response to other boundary  
246 conditions. In the newest version presented here, significant improvements in the representation of global  
247 biogeochemistry were achieved by (1) an explicit calculation of atmospheric O<sub>2</sub> levels based on atmospheric  
248 mass balance (Sect. 2.6), (2) expansion of the model framework to include secular evolution of sedimentary  
249 reservoirs (Sect. 2.5.5), and (3) simplification of the global redox budget between the surface (ocean-  
250 atmosphere-crust) system and the mantle (Sect. 2.3.5). These improvements are in line with the requirement  
251 of an ‘open’ Earth system model, which is necessary for a systematic, quantitative understanding of Earth’s  
252 oxygenation history.

### 253 **2.3 Global biogeochemical cycles**

254 We construct a comprehensive biogeochemical model in order to investigate the interaction between dynamic  
255 behaviors of Earth’s oxygenation history and its biogeochemical processes, as well as redox structure of the  
256 ocean. Here we provide the basic implementation of global biogeochemical cycles of C, P, N, and S, with  
257 particular emphasis on processes of mass exchange between reservoirs that play a critical role in global redox  
258 budget (Fig. 2). Our central aim here is to make the overall design of biogeochemical cycles clear. The details  
259 of each sub-model are provided in the following sections.

260





262 **Figure 2** Schematics of global biogeochemical cycles. **(a)** Global C cycle. The primary source of C for the  
263 ocean-atmosphere system is volcanic degassing and oxidative weathering of sedimentary organic carbon,  
264 whereas primary sink is burial of marine and terrigenous organic matter into sediments. Inorganic carbon  
265 reservoirs (depicted as dashed boxes) and DOC are not considered.  $NPP_{ocn}$  = marine net primary production.  
266 DIC = dissolved inorganic carbon. POC = particulate organic carbon. MSR = microbial sulfate reduction.  
267 AOM = anoxygenic oxidation of methane. CANOPS-GRB includes  $CH_4$  generation via methanogenesis and  
268 its oxidation reactions via methanotrophy and AOM in the ocean interior, as well as  $CH_4$  degassing flux to the  
269 atmosphere and its photooxidation. The rates of  $CH_4$  photooxidation and hydrogen escape to space are  
270 calculated based on parameterizations proposed by previous studies (Claire et al., 2006; Goldblatt et al., 2006).  
271 Note that  $CH_4$  flux from land biosphere is not shown here. **(b)** Global P cycle schematic. Weathering of  
272 reactive P ( $P_{react}$ ) is the ultimate source, whereas burial in sediments is the primary sink. A part of the weathered  
273 P is buried as terrigenous organic P, and the remaining is delivered to the ocean. The redox-dependent P burial  
274 in marine sediments is modelled by considering three phases (organic P, Fe-sorbed P, and authigenic P). DIP  
275 = dissolved inorganic phosphorus. POP = particulate organic phosphorus. The hypothetical P scavenging via  
276 Fe-species in anoxic-ferruginous waters is depicted, but it is not modelled in our standard model configuration.  
277 **(c)** Global N cycle schematic. Two inorganic nitrogen species (ammonium and nitrate), which are lumped into  
278 DIN (dissolved inorganic nitrogen), are transformed each other via denitrification and nitrification. The  
279 primary source is nitrogen fixation and riverine flux, whereas primary sink is denitrification and burial in  
280 marine sediments. PON = particulate organic nitrogen. The nitrogen weathering/riverine flux is assumed to  
281 be equal to the burial flux so that there is no mass imbalance in global N budget. Aeolian delivery of N from  
282 continent to the ocean is not included. **(d)** Global S cycle schematic. Two sedimentary reservoirs (pyrite sulfur,  
283 PYR, and gypsum sulfur, GYP) and two sulfur species ( $SO_4^{2-}$  and  $\Sigma H_2S$ ) in the ocean are transformed each  
284 other via volcanic outgassing, weathering, burial, MSR, AOM, and sulfide oxidation reactions. Weathering  
285 and volcanic inputs are the primary source of S to the ocean, and burial of pyrite and gypsum in marine  
286 sediments is the primary sink. It is assumed that hydrogen sulfide escaping from the ocean to the atmosphere  
287 is completely oxidized and returns to the ocean as sulfate. The organic sulfur cycle is ignored in this study.

### 288 2.3.1 Carbon cycle

289 The CANOPS-GRB model includes particulate organic carbon (POC), atmospheric  $CH_4$ , dissolved  $CH_4$  in  
290 the ocean, and sedimentary organic carbon (ORG) as carbon reservoirs (Fig. 2a). Atmospheric  $CO_2$ , dissolved  
291 inorganic carbon (DIC), and dissolved organic carbon (DOC) are not explicitly modelled in the current version  
292 of the model. The primary sources of carbon for the ocean-atmosphere system are volcanic degassing and  
293 oxidative weathering of sedimentary organic carbon, while the primary sink is burial of marine and terrigenous  
294 organic matter in sediments.



## 295 **Organic carbon cycle**

296 The biogeochemical model is driven by the cycling of the primary nutrient phosphorus, which is assumed to  
297 be the ultimate limiting factor for biological productivity (see Sect. 2.4.3). Previous versions of CANOPS do  
298 not take into account the impact of the activity of terrestrial ecosystem on the global O<sub>2</sub> budget. In the  
299 CANOPS-GRB model, we improve on this by evaluating the activity levels of terrestrial and marine  
300 ecosystems separately: The global net primary production (NPP),  $J_{\text{NPP}}$  (in terms of organic C), is given as a  
301 sum of the oceanic ( $J_{\text{NPP}}^{\text{ocn}}$ ) and terrestrial ( $J_{\text{NPP}}^{\text{ld}}$ ) NPP:

$$J_{\text{NPP}} = J_{\text{NPP}}^{\text{ocn}} + J_{\text{NPP}}^{\text{ld}} \quad (1)$$

302 Biological production in the ocean surface layer depends on P availability while nutrient assimilation  
303 efficiency is assumed to be lower in the high latitude region (Sect. 2.4.3). Terrestrial NPP is affected by the  
304 atmospheric O<sub>2</sub> level (Sect. 2.5.1). In this study, the flux (in terms of moles per year) is expressed with a  
305 capital  $J$ , whereas the flux density (in terms of moles per square meter per year) is expressed with a lowercase  
306  $j$ .

307

308 In our standard model configuration, oceanic primary production follows canonical Redfield stoichiometry  
309 (C:N:P = 106:16:1) (Redfield et al., 1963). Flexible C:N:P stoichiometry of particulate organic matter (POM)  
310 can be explored by changing a user-flag. Nutrients (P and N) are removed from seawater in the photic zone  
311 via biological uptake, and exported as POM to deeper aphotic layers. The exported POM sinks through the  
312 water column with a speed of  $v_{\text{POM}}$  (the reference value is 100 m d<sup>-1</sup>). As it settles through water column, POM  
313 is subject to decomposition via a series of respiration pathways dependent on the redox state of proximal  
314 seawater (Sect. 2.4.3). This gives rise to the release of dissolved constituent species back into seawater. Within  
315 each layer a fraction of POM is also intercepted by a sediment layer at the bottom of each water depth.  
316 Fractional coverage of every ocean layer by seafloor is calculated based on the prescribed bathymetry (Sect.  
317 2.4.1). Settling POM reaching the seafloor undergoes diagenetic alteration (releasing additional dissolved  
318 species into seawater) and/or permanent burial. The ocean model has 2×60 sediment segments, and for each  
319 segment the rates of organic matter decomposition and burial are calculated by semi-empirical relationships  
320 extracted from ocean sediment data and 1-D modelling of early diagenesis (Sect. 2.4.4). Specifically, the



321 organic C ( $C_{\text{org}}$ ) burial at each water depth is calculated based on the burial efficiency ( $BE_{\text{org}}$ ), which is defined  
322 as the fraction of POC buried in sediments relative to that deposited on the seafloor at each water depth and  
323 is also a function of sedimentation rate and bottom water  $O_2$  levels. Organic matter not buried is subject to  
324 decomposition.

325

326 The key biogeochemical fluxes of our reference state (mimicking the present condition) are summarized in  
327 Table 2. The reference value for burial rate of terrigenous  $C_{\text{org}}$  is set at  $3 \text{ Tmol C yr}^{-1}$ , assuming that burial of  
328 terrigenous organic matter accounts for ~20% of the total burial. Combined with the burial rate of marine  $C_{\text{org}}$   
329 in our standard run, the total burial rate is  $14.3 \text{ Tmol C yr}^{-1}$ , representing the dominant  $O_2$  source flux to the  
330 modern ocean-atmosphere system. At steady-state, this is balanced by oxidative weathering and volcanic  
331 outgassing of sedimentary  $C_{\text{org}}$ : The reference value of oxidative weathering of organic matter is determined  
332 as  $13.0 \text{ Tmol C yr}^{-1}$  based on the global  $O_2$  budget (Sect. 2.3.5). Previous versions of CANOPS (Ozaki et al.,  
333 2019a) treat sedimentary reservoirs as a boundary condition. This model limitation is removed in the  
334 CANOPS-GRB model—the reservoir size of sedimentary  $C_{\text{org}}$  ( $ORG$ ) freely evolves based on the mass  
335 balance through burial, weathering, and volcanic outgassing (Sect. 2.5.5). We adopted an oft-quoted value of  
336  $1250 \text{ Emol (E = } 10^{18})$  for our reference value of the  $ORG$ , based on literature survey (Bernier, 1989; Garrels  
337 and Lerman, 1981).

338



339 Table 2: Key biogeochemical fluxes obtained from the reference run. \* denotes the reference value. Tmol =  
 340  $10^{12}$  mol.

Fluxes	Label	Value	Comments
<b>Carbon cycle (Tmol C yr<sup>-1</sup>)</b>			
Marine NPP	$J_{\text{NPP}}^{\text{ocn},*}$	3794	Simulated (Eq. 24)
Terrestrial NPP	$J_{\text{NPP}}^{\text{ld},*}$	5000	Prescribed (Prentice et al., 2001)
Marine organic C burial	$J_{\text{org}}^{\text{b,ocn},*}$	11.28	Simulated (Eq. 40)
Terrestrial organic C burial	$J_{\text{org}}^{\text{b,ld},*}$	3.0	Prescribed (This study)
Oxidative organic C weathering	$J_{\text{org}}^{\text{w},*}$	13.03	Tuned (Eq. 15)
Organic C degassing	$J_{\text{org}}^{\text{m},*}$	1.25	Prescribed (Bergman et al., 2004)
<b>Phosphorus cycle (Tmol P yr<sup>-1</sup>)</b>			
Reactive P weathering	$J_{\text{P}}^{\text{w},*}$	0.158	Eqs. (4, 84)
Terrestrial organic P burial	$J_{\text{P}}^{\text{b,ld},*}$	0.003	Eq. (85)
Riverine reactive P flux	$J_{\text{P}}^{\text{r},*}$	0.155	Tuned (This study)
Marine organic P burial	$J_{\text{Porg}}^{\text{b},*}$	0.0438	Simulated (Eq. 51)
Fe-sorbed P burial	$J_{\text{PFe}}^{\text{b},*}$	0.0323	Simulated (Eq. 53)
Ca-bound P burial	$J_{\text{PCa}}^{\text{b},*}$	0.0788	Simulated (Eq. 54)
<b>Nitrogen cycle (Tg N yr<sup>-1</sup>)</b>			
Nitrogen fixation	$J_{\text{Nfix}}^*$	180.5	Simulated
Denitrification in the water column	$J_{\text{deni}}^{\text{wc},*}$	102.5	Simulated
Benthic denitfircation	$J_{\text{deni}}^{\text{sed},*}$	62.4	Simulted (Eq. 55)
Marine organic N burial	$J_{\text{Norg}}^{\text{b},*}$	15.8	Simulated (Eq. 56)
Organic N weathering	$J_{\text{Norg}}^{\text{w},*}$	15.8	= $J_{\text{Norg}}^{\text{b},*}$
<b>Sulfur cycle (Tmol S yr<sup>-1</sup>)</b>			
Pyrite weathering	$J_{\text{pyr}}^{\text{w},*}$	1.0	Prescribed (This study)
Gypsum weathering	$J_{\text{gyp}}^{\text{w},*}$	1.6	Prescribed (This study)
Pyrite degassing	$J_{\text{pyr}}^{\text{m},*}$	0.3	Prescribed (This study)
Gypsum degassing	$J_{\text{gyp}}^{\text{m},*}$	0.5	Prescribed (This study)
Pyrite burial	$J_{\text{pyr}}^{\text{b},*}$	1.3	Simulated
Gypsum burial	$J_{\text{gyp}}^{\text{b},*}$	2.1	Prescribed (This study)



## 342 Methane cycle

343 The ocean model includes biogenic CH<sub>4</sub> generation via methanogenesis and its oxidation reactions via  
344 methanotrophy and anoxygenic oxidation of methane (AOM) in the ocean interior (R10 and R11 in Table 1),  
345 as well as CH<sub>4</sub> degassing flux to the atmosphere. The land model also calculates the biogenic CH<sub>4</sub> flux from  
346 the terrestrial ecosystem to the atmosphere using a transfer function (Sect. 2.5.2). The abundance of CH<sub>4</sub> in  
347 the atmosphere is explicitly modelled as a balance of its source (degassing from marine and terrestrial  
348 ecosystems) and sink (photooxidation and hydrogen escape), where CH<sub>4</sub> sink fluxes are calculated according  
349 to parameterized O<sub>2</sub> dependent functions proposed by previous studies. More specifically, the oxidation rate  
350 of CH<sub>4</sub> in the upper atmosphere is calculated based on the empirical parameterization obtained from a 1-D  
351 photochemistry model (Claire et al., 2006). The rate of hydrogen escape to space is evaluated with the  
352 assumption that it is diffusion limited and that CH<sub>4</sub> is a major H-containing chemical compound carrying  
353 hydrogen to the upper atmosphere (Goldblatt et al., 2006). No continental abiotic or thermogenic CH<sub>4</sub> fluxes  
354 are taken into account, because previous estimates of the modern fluxes are negligible relative to the biogenic  
355 flux, although we realize that it could have played a role in the global redox budget (<0.3 Tmol yr<sup>-1</sup>; Fiebig et  
356 al., 2009). We also note that the current version of the model does not include the possibility of aerobic CH<sub>4</sub>  
357 production in the sea (Karl et al., 2008). Our reference run calculates atmospheric CH<sub>4</sub> to be 0.16 ppmv (Sect.  
358 3.3), slightly lower than that of the preindustrial level of 0.7 ppmv (Etheridge et al., 1998; Raynaud et al.,  
359 1993), but we consider this to be within reasonable error given unknowns in the CH<sub>4</sub> cycle.

## 360 2.3.2 Phosphorus cycle

361 Phosphorus is an essential element for all life on Earth and it is regarded as the ‘ultimate’ bio-limiting nutrient  
362 for primary productivity on geologic time scales (Tyrrell, 1999). Thus, the P cycle plays a prominent role in  
363 regulating global O<sub>2</sub> levels. In the CANOPS-GRB model, we model the reactive (i.e., bioavailable) P (P<sub>react</sub>)  
364 cycling in the system and ignore non-bioavailable P. Specifically, dissolved inorganic P (DIP) and particulate  
365 organic P (POP) are explicitly modelled (Fig. 2b), whereas dissolved organic P (DOP) is ignored.

366



367 On geologic timescales, the primary source of P to the ocean-atmosphere system is continental weathering:  
368 Phosphorus is released through the dissolution of apatite which exists as a trace mineral in silicate and  
369 carbonate rocks (~0.1wt%; Föllmi, 1996). The total  $P_{\text{reac}}$  flux via weathering,  $J_P^w$ , is given as follows:

$$J_P^w = f_P f_R J_P^{w,*}, \quad (2)$$

370 where \* denotes the reference value, and  $f_P$  and  $f_R$  are parameters that control the availability of P in the system.  
371 Specifically,  $f_R$  is a global erosion factor representing the impact of tectonic activity on total terrestrial  
372 weathering rate, and  $f_P$  represents the availability of  $P_{\text{reac}}$ , which is used in a sensitivity experiment to assess  
373 the response of atmospheric  $O_2$  levels to changing  $P_{\text{reac}}$  availability (Sect. 4.1). A fraction of the weathering  
374 flux  $J_P^w$  is removed via burial on land, while the remainder is transported to the ocean (Sect. 2.5.2):

$$J_P^{\text{b,ld}} = k_{11} V J_P^w, \quad (3)$$

$$J_P^r = (1 - k_{11} V) J_P^w \quad (4)$$

375 where  $J_P^{\text{b,ld}}$  and  $J_P^r$  denote the burial rate of terrigenous organic P and riverine  $P_{\text{reac}}$  flux to the ocean,  
376 respectively,  $k_{11}$  is a reference value for the fraction of the total P flux removed by the terrestrial biosphere,  
377 and  $V$  denotes the vegetation mass normalized to the modern value. These treatments are based on the Earth  
378 system box model COPSE (Bergman et al., 2004; Lenton et al., 2016; Lenton et al., 2018; Lenton and Watson,  
379 2000b) which has been extensively tested and validated against geologic records during the Phanerozoic. In  
380 the CANOPS-GRB model,  $J_P^r$  is tuned so that modelled oceanic P inventory of the reference state is consistent  
381 with modern observations of the global ocean (Sect. 3.2.4). Our resulting tuned value is  $0.155 \text{ Tmol P yr}^{-1}$   
382 falling in the mid-range of published estimates of  $0.11\text{--}0.33 \text{ Tmol P yr}^{-1}$ , although previous estimates of the  
383 riverine  $P_{\text{reac}}$  flux show large uncertainty (Sect. 3.2.4).

384

385 Since atmospheric P inputs are equivalent to less than 10% of the continental P supply to the modern oceans  
386 and much of this flux is not bioavailable (Graham and Duce, 1979), we neglect the aeolian flux in this study.  
387 Therefore, riverine input is the primary source of  $P_{\text{reac}}$  to the ocean. We highlight that open-system modelling  
388 is crucial for realistic simulations of ocean biogeochemistry on timescales longer than the residence time of P  
389 in the ocean (15–20 kyr for the modern ocean) (Hotinski et al., 2000), and in this framework the riverine input



390 of  $P_{\text{reac}}$  must be balanced over the long-term by loss to sediments via burial. The change in total marine  $P_{\text{reac}}$   
391 inventory,  $M_P$ , is given as follows:

$$\frac{dM_P}{dt} = J_P^r - J_P^{\text{b,ocn}}, \quad (5)$$

392 where  $J_P^{\text{b,ocn}}$  denotes the total burial flux of  $P_{\text{reac}}$  in the marine system which is the sum of the burial fluxes of  
393 three reactive phases, i.e. organic P ( $P_{\text{org}}$ ), Fe-sorbed P ( $P_{\text{-Fe}}$ ), and Ca-bound P ( $P_{\text{-Ca}}$ ) (Sect. 2.4.4):

$$J_P^{\text{b,ocn}} = J_{P_{\text{org}}}^{\text{b}} + J_{P_{\text{-Fe}}}^{\text{b}} + J_{P_{\text{-Ca}}}^{\text{b}}, \quad (6)$$

394 O<sub>2</sub>-dependent P burial is taken into account using empirical relationships from previous studies (Slomp and  
395 Van Cappellen, 2007; Van Cappellen and Ingall, 1994, 1996). The burial of  $P_{\text{org}}$  at each water depth is a  
396 function of burial efficiency, which is controlled by the burial efficiency of organic matter, C/P stoichiometry  
397 of POM, sedimentation rate and bottom water [O<sub>2</sub>]. We note that the strength of anoxia-induced P recycling  
398 in marine sediments is very poorly constrained, especially in the Precambrian oceans (Reinhard et al., 2017b).  
399 Recent studies also suggest that the P retention potential in marine sediments could be affected not only by  
400 bottom water O<sub>2</sub> levels but by redox states (sulfidic vs. ferruginous) and the Ca<sup>2+</sup> concentration of bottom  
401 waters (Zhao et al., 2020). These are fruitful topics for future research.

402

403 We do not explicitly account for P removal via hydrothermal processes, because it is estimated that this  
404 contribution is secondary in the modern marine P cycle (0.014–0.036 Tmol P yr<sup>-1</sup>; Wheat et al., 1996; Wheat  
405 et al., 2003). We note, however, that the hydrothermal contribution to the total P budget in the geologic past  
406 remains poorly constrained. We also note that in anoxic, ferruginous oceans, P scavenging by Fe-minerals  
407 could also play an important role in controlling P availability and the overall budget (Derry, 2015; Laakso and  
408 Schrag, 2014; Reinhard et al., 2017b). Modern observations (Dellwig et al., 2010; Shaffer, 1986; Turnewitsch  
409 and Pohl, 2010) and modeling efforts (Yakushev et al., 2007) of the redoxcline in the Baltic Sea and the Black  
410 Sea suggest an intimate relationship between Mn, Fe, and P cycling. Trapping efficiencies of DIP by settling  
411 authigenic Fe and Mn-rich particles were found to be as high as 0.63 (the trapping efficiency is defined as the  
412 downward flux of P in Mn-, and Fe-oxides divided by the upward flux of DIP) (Turnewitsch and Pohl, 2010).  
413 Although coupled Mn-Fe-P dynamics might have been a key aspect of the biogeochemical dynamics in the  
414 Precambrian oceans, we exclude this process in our standard model due to poor constraints and provide a clear



415 and simplified picture of basic model behavior. The key features between the P availability and atmospheric  
416 O<sub>2</sub> levels are explored by changing  $f_P$  in this study (Sect. 4).

### 417 2.3.3 Nitrogen cycle

418 In the CANOPS-GRB model, two dissolved inorganic nitrogen (DIN) species (total ammonium  $\Sigma\text{NH}_4^+$  and  
419 nitrate  $\text{NO}_3^-$ ) and particulate organic nitrogen (PON) are explicitly calculated (Fig. 2c). Atmospheric nitrogen  
420 gas is assumed to never limit biospheric carbon fixation, and is not explicitly calculated. Dissolved organic N  
421 (DON) and terrestrial N cycling (e.g., N fixation by terrestrial ecosystems and riverine-terrestrial organic N  
422 transfer) are ignored.

423

424 In the surface ocean N assimilation via nitrate and ammonium depends on the availability of these compounds.  
425 If the N required for sustaining a given level of biological productivity is not available, the additional N  
426 required is assumed to be provided by atmospheric N<sub>2</sub> via nitrogen fixers. The ocean model explicitly  
427 calculates denitrification and nitrification reactions in the water column and marine sediments (R5 and R8 in  
428 Table 1). The benthic denitrification rate is estimated using a semi-empirical parameterized function obtained  
429 from a 1-D early diagenetic model (see Sect. 2.4.4), while nitrification is modelled as a single step reaction  
430 (R8). N<sub>2</sub>O and its related reactions, such as anammox, are not currently included.

431

432 The oceanic N cycle is open to external inputs of nitrogen. While the ultimate source of N to the ocean-  
433 atmosphere system is weathering of organic N, nitrogen fixation represents the major input flux to the ocean  
434 with the capacity to compensate for N loss due to denitrification. The time evolution of DIN inventory,  $M_N$ ,  
435 in the ocean can be written as follows:

$$\frac{dM_N}{dt} = (J_{\text{Nfix}} - J_{\text{deni}}^{\text{wc}} - J_{\text{deni}}^{\text{sed}}) + (J_{\text{Norg}}^{\text{w}} - J_{\text{Norg}}^{\text{b}}), \quad (7)$$

436 where  $J_{\text{Nfix}}$  denotes the N fixation rate, and  $J_{\text{deni}}^{\text{wc}}$  and  $J_{\text{deni}}^{\text{sed}}$  are denitrification rates in the water column and  
437 sediments, respectively. The first set of terms on the right-hand side represent the internal N cycle in the ocean-  
438 atmosphere system, while the second set of terms represent the long-term N budget which interacts with  
439 sedimentary reservoir. Ultimately, loss of fixed N from the ocean-atmosphere system only occurs via burial



440 of organic N ( $N_{\text{org}}$ ) in sediments,  $J_{\text{Norg}}^{\text{b}}$ . This loss is compensated for by continental weathering,  $J_{\text{Norg}}^{\text{w}}$ , which  
441 is assumed to be equal to the burial rate of  $N_{\text{org}}$  so that the N cycle has no impact on the global redox budget.  
442 In the current version of the model, we ignore aeolian flux and all riverine N fluxes other than weathering  
443 since these are minor relative to N fixation (Wang et al., 2019). As a result, modelled N fixation required for  
444 oceanic N balance can be regarded as an upper estimate.

### 445 2.3.4 Sulfur cycle

446 The original CANOPS ocean model (Ozaki and Tajika, 2013; Ozaki et al., 2011) treated two sulfur species,  
447  $\text{SO}_4^{2-}$  and  $\Sigma\text{H}_2\text{S}$ , in a closed system: Neither inputs to the ocean from rivers, hydrothermal vents, and  
448 submarine volcanoes, nor outputs due to evaporite formation and sedimentary pyrite burial were simulated.  
449 This simplification can be justified when the timescale of interest is less than the residence time of the S cycle  
450 (~10–20 Myr). The recently-revised CANOPS model (Ozaki et al., 2019a) extends the framework by  
451 incorporating the S budget in the ocean. In their model framework, the sedimentary S reservoirs are treated as  
452 boundary conditions: The size of sedimentary gypsum and pyrite reservoirs are prescribed and no explicit  
453 calculations of mass balance are performed. In CANOPS-GRB, we removed this model limitation and the  
454 sedimentary reservoirs are explicitly evaluated based on mass balance which is controlled by burial,  
455 outgassing and weathering (see Sect. 2.4). Specifically, seawater  $\text{SO}_4^{2-}$ ,  $\Sigma\text{H}_2\text{S}$ , and sedimentary sulfur  
456 reservoirs of pyrite sulfur (*PYR*) and gypsum sulfur (*GYP*) are explicitly evaluated in the current version of  
457 the model. No atmospheric sulfur species are calculated—all  $\text{H}_2\text{S}$  degassing from the ocean to the atmosphere  
458 is assumed to be oxidized to sulfate and return to the ocean. The organic sulfur cycle is not considered in this  
459 study.

460

461 Sulfur enters the ocean mainly from river runoff,  $J_{\text{S}}^{\text{r}}$ , with minor contributions from volcanic outgassing of  
462 sedimentary pyrite,  $J_{\text{pyr}}^{\text{m}}$  and gypsum,  $J_{\text{gyp}}^{\text{m}}$ . The reference value for the riverine flux is set at  $2.6 \text{ Tmol S yr}^{-1}$ ,  
463 consistent with the published estimate of  $2.6 \pm 0.6 \text{ Tmol S yr}^{-1}$  (Raiswell and Canfield, 2012). The riverine flux  
464 is written as the sum of gypsum weathering and oxidative weathering of pyrite:  $J_{\text{S}}^{\text{r}} = J_{\text{gyp}}^{\text{w}} + J_{\text{pyr}}^{\text{w}}$ . Sulfur  
465 weathering fluxes are also assumed to be proportional to the sedimentary reservoir size. Estimates of modern  
466 volcanic input fall within the range of  $0.3\text{--}3 \text{ Tmol S yr}^{-1}$  (Catling and Kasting, 2017; Kagoshima et al., 2015;



467 Raiswell and Canfield, 2012; Walker and Brimblecombe, 1985). We adopted a value of 0.8 Tmol S yr<sup>-1</sup> for  
468 this flux (Kagoshima et al., 2015). Our total input of 3.4 Tmol S yr<sup>-1</sup> is also within the range of the previous  
469 estimate of 3.3±0.7 Tmol S yr<sup>-1</sup> (Raiswell and Canfield, 2012). Sulfur is removed from the ocean either via  
470 pyrite burial,  $J_{\text{pyr}}^{\text{b}}$ , or gypsum deposition,  $J_{\text{gyp}}^{\text{b}}$  (Fig. 2d). The time evolution of the inventory of total S in the  
471 ocean can thus be written, as follows:

$$\frac{d(M_{\text{SO}_4} + M_{\text{H}_2\text{S}})}{dt} = (J_{\text{S}}^{\text{r}} + J_{\text{pyr}}^{\text{m}} + J_{\text{gyp}}^{\text{m}}) - (J_{\text{pyr}}^{\text{b}} + J_{\text{gyp}}^{\text{b}}), \quad (8)$$

472 where  $M_{\text{SO}_4}$  and  $M_{\text{H}_2\text{S}}$  denote the inventory of sulfate and hydrogen sulfide in the ocean, respectively. Two  
473 sulfur species ( $\text{SO}_4^{2-}$  and  $\Sigma\text{H}_2\text{S}$ ) are transformed via microbial sulfate reduction (MSR) (R6), AOM (R11),  
474 and aerobic sulfide oxidation reactions (R9). The above equation thus can be divided into following equations:

$$\frac{dM_{\text{SO}_4}}{dt} = J_{\text{S}}^{\text{r}} + J_{\text{pyr}}^{\text{m}} + J_{\text{gyp}}^{\text{m}} + J_{\text{H}_2\text{S}}^{\text{ox}} - J_{\text{MSR\&AOM}} - J_{\text{gyp}}^{\text{b}}, \quad (9)$$

$$\frac{dM_{\text{H}_2\text{S}}}{dt} = -J_{\text{H}_2\text{S}}^{\text{ox}} + J_{\text{MSR\&AOM}} - J_{\text{pyr}}^{\text{b}}, \quad (10)$$

475 where  $J_{\text{H}_2\text{S}}^{\text{ox}}$  denotes the oxidation of hydrogen sulfide and  $J_{\text{MSR\&AOM}}$  is sulfate reduction via MSR and AOM.  
476 Pyrite burial is represented as the sum of pyrite precipitation in the water column and sediments:  $J_{\text{pyr}}^{\text{b}} = J_{\text{pyr}}^{\text{b,wc}}$   
477  $+ J_{\text{pyr}}^{\text{b,sed}}$ , where the pyrite burial rate in marine sediments is assumed to be proportional to the rate of benthic  
478 sulfide production. The proportional coefficient, pyrite burial efficiency ( $e_{\text{pyr}}$ ), is one of the tunable constants  
479 of the model: For normal (oxic) marine sediments  $e_{\text{pyr}}$  is tuned such that the seawater  $\text{SO}_4^{2-}$  concentration for  
480 our reference run is consistent with modern observations (Sect. 2.4.3). Pyrite precipitation in the water column  
481 is assumed to be proportional to the concentration of  $\Sigma\text{H}_2\text{S}$ .

482

483 Although the present-day marine S budget is likely out of balance because of a lack of major gypsum formation,  
484 the S cycle can be considered to operate at steady state on timescales longer than the residence time of sulfur  
485 in the ocean. According to S isotope mass balance calculations, ~10–45% of the removal flux is accounted for  
486 by pyrite burial, and the remainder is removed via formation of gypsum/anhydrite in the near-modern oceans  
487 (Tostevin et al., 2014). Although gypsum deposition would have been strongly influenced by tectonic activity  
488 (Halevy et al., 2012), we assume that the rate of gypsum deposition on geologic time scales is proportional to



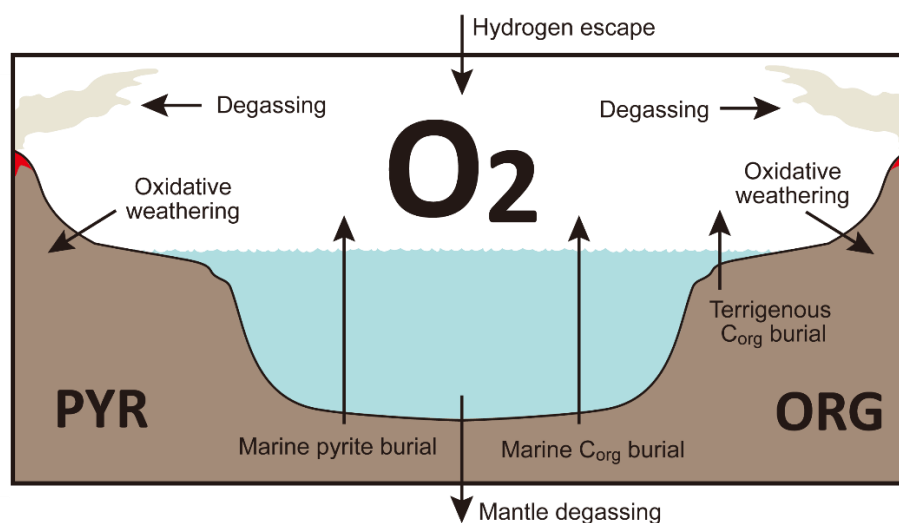
489 the ion product of  $\text{Ca}^{2+}$  and  $\text{SO}_4^{2-}$  (Berner, 2004a) in the low- to mid-latitude surface layer (L), and is defined  
 490 as follows:

$$J_{\text{gyp}}^{\text{b}} = \left( \frac{[\text{Ca}^{2+}]_l [\text{SO}_4^{2-}]_l}{[\text{Ca}^{2+}]^* [\text{SO}_4^{2-}]^*} \right) J_{\text{gyp}}^{\text{b},*} = f_{\text{Ca}} \left( \frac{[\text{SO}_4^{2-}]_l}{[\text{SO}_4^{2-}]^*} \right) J_{\text{gyp}}^{\text{b},*} \quad (11)$$

491 where  $l$  denotes the low- to mid-latitude surface layer and  $f_{\text{Ca}}$  is a parameter that represents the seawater  $\text{Ca}^{2+}$   
 492 concentration normalized by the present value ( $f_{\text{Ca}} = 1$  for the reference run). The reference value of gypsum  
 493 burial  $J_{\text{gyp}}^{\text{b},*}$  is determined by assuming that gypsum deposition accounts for ~60% of the total S removal from  
 494 the near-modern ocean.

### 495 2.3.5 Global redox budget

496 In the previous version of the CANOPS model (Ozaki et al., 2019a), the atmospheric  $\text{O}_2$  level was prescribed  
 497 as a boundary condition, rather than modeled in order to limit computational demands. In this study, we  
 498 remove this model limitation by introducing an explicit mass balance calculation of atmospheric  $\text{O}_2$  (Sect.  
 499 2.6.3). This improvement allows us to explore the dynamic response of  $\text{O}_2$  levels in the ocean-atmosphere  
 500 system (Sect. 4).



501

502 **Figure 3** Schematics of global redox ( $\text{O}_2$ ) budget. Arrows represent the  $\text{O}_2$  flux. The primary source is burial  
 503 of organic carbon and pyrite sulfur in sediments and hydrogen escape to space. The primary sink is volcanic  
 504 outgassing and weathering of crustal organic matter and pyrite. PYR = sedimentary reservoir of pyrite sulfur.  
 505 ORG = sedimentary reservoir of organic carbon. CANOPS-GRB tracks the global redox ( $\text{O}_2$ ) budget for each  
 506 simulation.



507

508 The newly released CANOPS-GRB is designed to be a part of a comprehensive global redox budget (GRB)  
509 framework (Fig. 3) (Catling and Kasting, 2017; Ozaki and Reinhard, 2021). Here GRB is defined for the  
510 combined ocean-atmosphere system. In this study we track GRB in terms of O<sub>2</sub> equivalents. The ultimate  
511 source of O<sub>2</sub> is the activity of oxygenic photosynthesis (and subsequent burial of reduced species, such as  
512 organic matter and pyrite sulfur, in sediments), whereas the primary sink of O<sub>2</sub> is the oxidative weathering of  
513 organic carbon and pyrite which are assumed to be O<sub>2</sub>-dependent (Sect. 2.5.3). On timescales longer than the  
514 residence time of O<sub>2</sub> in the ocean-atmosphere system, O<sub>2</sub> source fluxes should be balanced by sink fluxes.  
515 Specifically, the O<sub>2</sub> budget in the coupled ocean-atmosphere system can be expressed as follows:

$$\text{GRB} = \left( J_{\text{org}}^{\text{b,ocn}} + J_{\text{org}}^{\text{b,lnd}} - J_{\text{org}}^{\text{w}} - J_{\text{org}}^{\text{m}} \right) + 2 \left( J_{\text{pyr}}^{\text{b}} - J_{\text{pyr}}^{\text{w}} - J_{\text{pyr}}^{\text{m}} \right) + \left( J_{\text{Hesc}} - J_{\text{man}} \right), \quad (12)$$

516 where the first and second set of terms on the right-hand side represent the redox balance via organic carbon  
517 and pyrite sulfur subcycles, respectively.  $J_{\text{Hesc}}$  in the third term denotes hydrogen escape to space, representing  
518 the irreversible oxidation of the system. For well-oxygenated atmospheres this process plays a minor role in  
519 the redox budget, but for less oxygenated atmospheres with high levels of CH<sub>4</sub> this flux could lead to redox  
520 imbalance. In this study we include the input of reducing power (e.g., H<sub>2</sub> and CO) from the Earth's interior to  
521 the surface,  $J_{\text{man}}$ , which is assumed to be equal to the value of  $J_{\text{Hesc}}$  ( $J_{\text{man}} = J_{\text{Hesc}}$ ) to avoid redox imbalance in  
522 the exogenic system. In reality, mantle degassing and the rate of hydrogen escape are not necessarily equal,  
523 resulting in redox imbalance that may exert a fundamental control on atmospheric redox chemistry on geologic  
524 timescales (Canfield, 2004; Eguchi et al., 2020; Hayes and Waldbauer, 2006; Ozaki and Reinhard, 2021),  
525 however to maintain simplicity we have left this as a topic for future work. As a result, the terms on the right-  
526 hand side must be balanced at steady state. Our model can meet this criterion. Note that the effects of the Fe  
527 cycle on the O<sub>2</sub> budget (e.g., the oxidative weathering of Fe(II)-bearing minerals; Ozaki et al., 2019a) are not  
528 currently included for the sake of simplicity.

529

530 The CANOPS-GRB model also tracks the O<sub>2</sub> budgets for the atmosphere and ocean independently, and these  
531 can be evaluated by the following relationships:

$$\text{ARB} = \Phi_{\text{ex}}^{\text{air-sea}} + \left( J_{\text{org}}^{\text{b,lnd}} - J_{\text{org}}^{\text{w}} - J_{\text{org}}^{\text{m}} \right) - 2 \left( J_{\text{pyr}}^{\text{w}} + J_{\text{pyr}}^{\text{m}} \right) + \left( J_{\text{Hesc}} - J_{\text{man}} \right), \quad (13)$$



$$ORB = -\Phi_{\text{ex}}^{\text{air-sea}} + J_{\text{org}}^{\text{b,ocn}} + 2J_{\text{pyr}}^{\text{b}}, \quad (14)$$

532 where *ARB* and *ORB* denote the redox budget in the atmosphere and ocean, respectively,  $\Phi_{\text{ex}}^{\text{air-sea}}$  represents  
533 the net exchange of oxidizing power between the ocean and atmosphere via gas exchange ( $\text{O}_2$  with minor  
534 contributions of  $\text{NH}_3$ ,  $\text{H}_2\text{S}$  and  $\text{CH}_4$ ). These separate redox budgets are also tracked in order to validate global  
535 budget calculations.

536

537 For our reference condition, we obtain the reference value for the oxidative weathering rate of  $\text{C}_{\text{org}}$  ( $J_{\text{org}}^{\text{w},*}$ )  
538 using the redox budget via  $\text{C}_{\text{org}}$  subcycle:

$$J_{\text{org}}^{\text{w},*} = J_{\text{org}}^{\text{b,ocn},*} + J_{\text{org}}^{\text{b,lnd},*} - J_{\text{org}}^{\text{m},*}. \quad (15)$$

539 Given flux values based on the calculated ( $J_{\text{org}}^{\text{b,ocn},*} = 11.28 \text{ Tmol C yr}^{-1}$ ) and prescribed ( $J_{\text{org}}^{\text{b,lnd},*} = 3 \text{ Tmol}$   
540  $\text{C yr}^{-1}$ ,  $J_{\text{org}}^{\text{m},*} = 1.25 \text{ Tmol C yr}^{-1}$ ) values on the right-hand side,  $J_{\text{org}}^{\text{w},*}$  is estimated as  $13.03 \text{ Tmol C yr}^{-1}$  (Table  
541 2).

## 542 2.4 Ocean model

543 Here we undertake a thorough review, reconsideration and revision (where warranted), of all aspects of the  
544 ocean model, including bringing together developments of the model since the original paper (Ozaki and  
545 Tajika, 2013; Ozaki et al., 2011).

546

547 The ocean model includes exchange of chemical species with external systems via several processes such as  
548 air-sea exchange, riverine input, and sediment burial. The biogeochemical model also includes a series of  
549 biogeochemical processes, such as the ocean biological pump and redox reactions under oxic-anoxic-sulfidic  
550 conditions. Our ocean model is convenient for investigating Earth system changes on timescales of hundreds  
551 of years or longer and it can be relatively easily integrated, rendering the model unique in terms of  
552 biogeochemical cycle models. CANOPS is also well suited for sensitivity studies and can be used to obtain  
553 useful information upstream of more complex models.

554

555 Development of the ocean model included two initial goals: The first goal is to adopt a general and robust  
556 ocean circulation scheme capable of producing well-resolved modern distributions of circulation tracers, using



557 realistic ventilation rates with a limited number of free parameters. The model's output for circulation tracers  
558 are validated by comparison with modern observations (see Sect. 3). This confirms that our ocean circulation  
559 scheme is adequate for representing the global patterns of water mass transport. The second goal is to couple  
560 the circulation model with an ocean biogeochemical model, and to evaluate performance by comparison with  
561 modern ocean biogeochemical data (see Sect. 3.2). Examination of the distributions and globally-integrated  
562 fluxes of C, N, P, S, and O<sub>2</sub> for the modern ocean reveals that the ocean model can capture the fundamentals  
563 of marine biogeochemical cycling.

#### 564 **2.4.1 Structure**

565 CANOPS ocean model is a 1-D (vertically resolved) intermediate complexity box model of ocean  
566 biogeochemistry (see Fig. 1b for the schematic structure) originally developed by (Ozaki and Tajika, 2013;  
567 Ozaki et al., 2011). Our model structure is an improved version of the HILDA model (Joos et al., 1991; Shaffer  
568 and Sarmiento, 1995). Unlike simple one-dimensional global ocean models (e.g. Southam et al., 1982), the  
569 HILDA-type model includes explicit high-latitude dynamics whereby the high-latitude surface layer  
570 exchanges properties with the deep ocean. This treatment is crucial for simulating preformed properties and  
571 observed chemical distributions, especially for phosphate and dissolved O<sub>2</sub> in a self-consistent manner. Unlike  
572 simple box-type global ocean models, the model has high vertical resolution. This is needed for representing  
573 proper biogeochemical processes which show strong depth dependency. Furthermore, HILDA type models  
574 (Arndt et al., 2011; Shaffer et al., 2008), unlike multi-box-type global ocean models (Hotinski et al., 2000),  
575 use a small number of free parameters to represent ocean physics and biology. The simple and adaptable  
576 structure of the model should make it applicable to a wide range of paleoceanographic problems. It couples a  
577 diffusion-advection model of the global ocean with a biogeochemical model (Sect. 2.4.3) and a parameterized  
578 sediment model (Sect. 2.4.4).

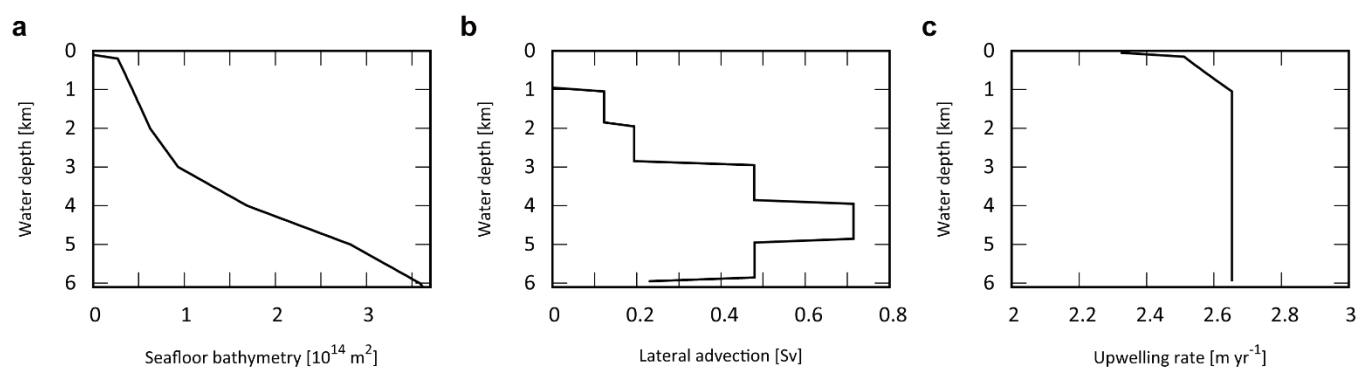
579

580 The ocean surface consists of a mixed layer at low-mid latitude (L) and high-latitude (H). Below the surface  
581 layers, we adopt the present-day averaged seafloor topography of (Millero, 2006) (Hypsometric profile is  
582 shown in Fig. 4a). Below the surface water layers, the ocean interior comprises two regions: the high-mid  
583 latitude region (HD) and low-mid latitude region (LD). Each region is subdivided vertically, with high



584 resolution ( $\Delta z = 100$  m). Each of the 60 ocean layers in each latitude region (120 total) is assigned ocean  
585 sediment properties. The cross-sectional area, volume, and sediment surface area of each box is calculated  
586 from the benthic hypsometry. Inclusion of the bathymetry allows evaluation of the flux of biogenic materials  
587 which settle on, and are buried in, seafloor sediments at each water depth (Sect. 2.3.3 and 2.3.4).

588



589

590 **Figure 4** Ocean bathymetry and water transport. (a) Seafloor topography (cumulative seafloor area) (Millero,  
591 2006) adopted in the CANOS-GRB model. (b) Lateral water advection from HD to LD section assumed in  
592 the standard run (in Sv). Total advection rate  $\dot{V}$  was set at 20 Sv. (c) Upwelling rate in the LD region (in  $\text{m}$   
593  $\text{yr}^{-1}$ ) of the standard run.

## 594 2.4.2 Transport

595 The ocean circulation model represents a general and robust scheme that is capable of producing well-resolved  
596 modern profiles of circulation tracers using realistic parameter values, and the coupled biogeochemical model  
597 (Sect. 2.4.3) and the parameterized sediment model (Sect. 2.4.4).

598

599 The time-space evolution of model variables in the ocean is described by a system of horizontally integrated  
600 vertical diffusion equations for non-conservative substances. The tracer conservation equation establishes the  
601 relationship between change of tracer concentration at a given grid point and the processes that can change  
602 that concentration. These processes include water transport by advection and mixing, and sources and sinks  
603 due to biological and chemical transformations. The temporal and spatial evolution of the concentration of a  
604 dissolved component in the aphotic zone is described by a horizontally integrated vertical diffusion equation,



605 which relates the rate of change of tracer concentration at a given point to the processes that act to change the  
606 tracer concentration:

$$\frac{\partial[X]}{\partial t} = \frac{\partial[X]}{\partial t} \Big|_{\text{trans}} + \Theta_{\text{bio}} + \Theta_{\text{react}}, \quad (16)$$

607 where  $[X]$  represents horizontally integrated physical variables (such as potential temperature, salinity or  $^{14}\text{C}$ )  
608 or concentration of a chemical component,  $t$  denotes time, and  $\Theta_{\text{bio}}$  and  $\Theta_{\text{react}}$  represents internal sources and  
609 sinks associated with the biological pump and chemical reactions, respectively. An external source/sink term  
610  $\Theta_{\text{ex}}$ , which represents riverine input and/or air-sea gas exchange, is added to the surface layers. The first term  
611 on the right hand side of equation (16) represents the physical transport:

$$\frac{\partial[X]}{\partial t} \Big|_{\text{trans}} = -A^{l,h}(z)w^{l,h}(z) \frac{\partial[X]}{\partial z} + \frac{\partial}{\partial z} \left( A^{l,h}(z)K_v^{l,h}(z) \frac{\partial[X]}{\partial z} \right) + K_{\text{hor}} \frac{\partial^2[X]}{\partial y^2}. \quad (17)$$

612 The terms on the right-hand side express (from left to right) the advection, vertical diffusion, and horizontal  
613 diffusion. Here,  $l$  and  $h$  indicate the LD and HD, respectively. The factors  $K_v^{l,h}(z)$ ,  $K_{\text{hor}}$ ,  $A^{l,h}(z)$ , and  $w^{l,h}(z)$   
614 denotes the vertical and horizontal diffusion coefficients, the areal fraction of the water layer at water depth  $z$   
615 to the sea surface area, and upwelling (for LD) or downwelling (for HD) velocity, respectively.

616

617 In the CANOPS ocean model, ocean circulation and mixing are characterized by five physical parameters: (1)  
618 water transport via thermohaline circulation,  $\dot{V}$ , associated with high latitude sinking and low-mid latitude  
619 upwelling; (2) constant horizontal diffusion between the aphotic zones,  $K_{\text{hor}}$ ; (3) strong, depth-dependent  
620 vertical diffusion between the aphotic zones in the high latitude region,  $K_v^h(z)$ ; (4) high latitude convection,  
621  $\dot{V}_h$ ; and (5) depth-dependent vertical diffusion in the low-mid latitude region,  $K_v^l(z)$ . These parameters are  
622 tuned to give tracer distributions consistent with present-day observations.

### 623 Advection

624 Advective water transport in the ocean model represents the major features of modern meridional overturning  
625 circulation. The rate of production of ventilated ocean waters ranges from 14 to 27 Sv ( $1 \text{ Sv} = 10^6 \text{ m}^3 \text{ s}^{-1}$ ) in  
626 the North Atlantic and from 18 to 30 Sv in the Southern Ocean (e.g., Doney et al., 2004; Lumpkin and Speer,



627 2007). The formation of deepwater effectively supplies “fresh” ventilated water to the abyss. We choose  $\dot{V} =$   
628 20 Sv as a reference value, giving a mean overturning time of about 2,140 yr, consistent with the ventilation  
629 time estimated from observations (Broecker and Peng, 1982).

630

631 The downwelling of the surface waters at H forms HD that flows into the intermediate to deep oceanic layers  
632 of LD, which, in turn, upwells over L (Fig. 1b). In many one-dimensional ocean models, downwelling water  
633 enters the ocean interior via the deepest model layer (e.g., Shaffer and Sarmiento, 1995; Southam et al., 1982;  
634 Volk and Hoffert, 1985). In the real ocean, downwelling waters are transported along isopycnal layers below  
635 approximately 1,000 m (e.g., Doney et al., 2004; Lumpkin and Speer, 2007; Shaffer and Sarmiento, 1995;  
636 Volk and Hoffert, 1985). Hence, we assume that high-latitude deep water flows into each ocean layer below  
637 1,100 m. While there is some uncertainty in the pattern of lateral advection, the flow is determined in our  
638 model assuming a constant upwelling rate below a depth of 1,100 m in the LD region. The  
639 upwelling/downwelling rate  $w^{l,h}(z)$  is then determined by the seafloor topography and the deep water lateral  
640 inflow, assuming continuity. Figure 4b shows the lateral advection of deep waters with a reference circulation  
641 rate  $\dot{V}$  of 20 Sv. This assumption provides a plausible upwelling rate, which is consistent with the oft-quoted  
642 value of 2–3 m yr<sup>-1</sup> (Broecker and Peng, 1982) (Fig. 4c).

### 643 **Vertical mixing**

644 Ocean circulation is dominated by turbulent processes driven by wind and tidal mixing. These processes occur  
645 as eddies which occur at a wide range of spatial scales, from centimeters to whole ocean basins. In numerical  
646 models of ocean circulation, turbulent mixing in the ocean interior is commonly represented as a diffusion  
647 process, characterized by an eddy diffusion coefficient. The vertical eddy diffusion coefficient  $K_v(z)$  is  
648 typically on the order of  $10^{-5}$  to  $10^{-4}$  m<sup>2</sup> s<sup>-1</sup> and it is common to assume a depth-dependence which smoothly  
649 increases from the thermocline ( $\sim 10^{-5}$  m<sup>2</sup> s<sup>-1</sup>) to the abyss ( $\sim 10^{-4}$  m<sup>2</sup> s<sup>-1</sup>) using an inverse or hyperbolic tangent  
650 function (e.g., Shaffer et al., 2008; Yakushev et al., 2007). To account for thermocline ventilation, we assumed  
651 a relatively high vertical diffusion coefficient in mid-water depth ( $K_l = 6.3 \times 10^{-5}$  m<sup>2</sup> s<sup>-1</sup> for water depth  
652 500–1500 m). We also adopted a higher value for the vertical diffusion coefficient ( $K_u = 1.6 \times 10^{-4}$  m<sup>2</sup> s<sup>-1</sup>) in



653 the upper most 500 m of the ocean in order to represent the highly convective Ekman layer in the upper part  
654 of the ocean.

$$K_v^1(z) = \begin{cases} K_u & (z \geq -500 \text{ m}) \\ K_1 & (-500 \geq z \geq -1500 \text{ m}) \\ \kappa^s + \frac{\kappa^d - \kappa^s}{2} \left( 1 + \tanh \left( \frac{z - z^1}{z^1} \right) \right) & (\text{otherwise}) \end{cases}, \quad (18)$$

655 where  $\kappa^s$  and  $\kappa^d$  are vertical mixing coefficients, and  $z^1$  is the transition length scale (Romaniello and Derry,  
656 2010). In the high latitude region where no permanent thermocline exists, more rapid communication with  
657 deep waters can occur. Previous studies have pointed out that the vertical diffusivities at high latitude can be  
658 very high (up to  $O(10^{-2} \text{ m}^2 \text{ s}^{-1})$ ) (e.g., Sloyan, 2005). To account for this we include high-latitude convection  
659 between H and YD ( $\dot{V}_h = 57.4 \text{ Sv}$ ) and higher vertical diffusion ( $K_v^h(z) = 2 \times K_v^1(z)$ ).

## 660 Horizontal diffusion

661 The horizontal diffusivity is included according to Romaniello and Derry (2010). On basin scales, the  
662 horizontal (isopycnal) eddy diffusivity is  $10^7$ – $10^8$  times larger than the vertical (diapycnal) eddy diffusivity  
663 due to anisotropy of the density field. For a spatial scale of 1,000 km, horizontal eddy diffusion is estimated  
664 to be  $O(10^3 \text{ m}^2 \text{ s}^{-1})$  (e.g., Ledwell et al., 1998). We adopt this value. As Romaniello and Derry (2010) did, we  
665 assume horizontal mixing follows the pathways of advective fluxes between laterally adjacent regions. The  
666 reciprocal exchange fluxes may be written as

$$J_{\text{hor}}^{\text{ex}} = K_{\text{hor}} A_{\perp} \frac{\partial[X]}{\partial y} = \frac{K_{\text{hor}} A_{\perp}}{L} \Delta[X], \quad (19)$$

667 where  $J_{\text{hor}}^{\text{ex}}$  denotes the exchange fluxes between the layers (in  $\text{mol yr}^{-1}$ ),  $A_{\perp}$  represents the cross-sectional  
668 area separating two adjacent reservoirs,  $L$  is a characteristic spatial distance separating the reservoirs,  $\Delta[X]$  is  
669 the difference in concentration between two reservoirs (Romaniello and Derry, 2010). By assuming that  $L$  is



670 of the same order as the length of the interface separating the two regions, we can approximate  $A_{\perp} \approx \Delta z \times O(L)$ ,  
 671 where  $\Delta z$  is the thickness of the interface separating the two regions. Then we obtain

$$J_{\text{hor}}^{\text{ex}} = K_{\text{hor}} \Delta z \Delta[X]. \quad (20)$$

672 Therefore, when we discretize the ocean interior at 100 m spacing approximately 0.1 Sv of reciprocal mixing  
 673 occurs between adjacent layers.

### 674 Ocean circulation tracers

675 We use potential temperature  $\theta$ , salinity  $S$ , and radioactive carbon  $^{14}\text{C}$ , as physical tracers. Distributions of  
 676 these tracers are determined by the transport mechanisms described above. In this study, we adopt the values  
 677 at the surface layers (L and H) as upper boundary conditions:  $\theta^l = 15^\circ\text{C}$ ,  $\theta^h = 0^\circ\text{C}$ ,  $S^l = 35$  psu,  $S^h = 34$  psu,  
 678  $\Delta^{14}\text{C}^l = -40\%$ , and  $\Delta^{14}\text{C}^h = -100\%$ . The radioactive decay rate for  $^{14}\text{C}$  is  $1.21 \times 10^{-4} \text{ yr}^{-1}$ . Although  $^{14}\text{C}$  can be  
 679 incorporated in the biogenic materials and transported into deep water, we ignore this biological effect for  
 680 simplicity. The associated error is  $\sim 10\%$  of the profiles produced by circulation and radioactive decay (Shaffer  
 681 and Sarmiento, 1995). The parameter values used in the ocean circulation model are listed in Table 3.

682 Table 3: Physical set-up of the ocean circulation model.

Parameters	Label	Value	Unit	Ref.
Ocean surface area	$A$	$3.62 \times 10^{14}$	$\text{m}^2$	(Ozaki and Tajika, 2013)
Surface area of high-latitude layer (H)	$A^h$	$0.362 \times 10^{14}$	$\text{m}^2$	(Ozaki and Tajika, 2013)
Depth of mixed layer	$h_m$	100	m	(Ozaki and Tajika, 2013)
Grid spacing	$\Delta z$	100	m	(Ozaki and Tajika, 2013)
Water depth of ocean bottom	$z_b$	6,100	m	(Ozaki and Tajika, 2013)
Ocean overturning rate	$\dot{V}$	20	Sv	(Ozaki and Tajika, 2013)
Vertical mixing coefficient ( $z < 500$ m)	$K_u$	5,000	$\text{m}^2 \text{ yr}^{-1}$	(Ozaki and Tajika, 2013)
Vertical mixing coefficient ( $500 \text{ m} < z < 1,500$ m)	$K_l$	2,500	$\text{m}^2 \text{ yr}^{-1}$	(Ozaki and Tajika, 2013)
Mixing coefficient	$\kappa_s$	473	$\text{m}^2 \text{ yr}^{-1}$	(Romaniello and Derry, 2010)
Mixing coefficient	$\kappa_d$	3,154	$\text{m}^2 \text{ yr}^{-1}$	(Romaniello and Derry, 2010)
Transition depth for vertical mixing coefficient	$z_l$	1,000	m	(Romaniello and Derry, 2010)
High-latitude convection rate	$\dot{V}_h$	57.4	Sv	(Ozaki and Tajika, 2013)
Horizontal diffusion coefficient	$K_{\text{hor}}$	1,000	$\text{m}^2 \text{ s}^{-1}$	(Romaniello and Derry, 2010)



### 683 2.4.3 Ocean biogeochemical framework

684 The ocean circulation model is coupled to a biogeochemical model, which includes an explicit representation  
 685 of a variety of biogeochemical processes in the ocean. The parameters used in the oceanic biogeochemical  
 686 model are listed in Table 4.

687 Table 4 Parameter values used in the oceanic biogeochemistry module of CANOPS-GRB.

Parameter	Label	Value	Unit	Ref.
Efficiency factor for phosphate uptake at L	$\varepsilon^l$	1.0	–	(Ozaki and Tajika, 2013)
Efficiency factor for phosphate uptake at H	$\varepsilon^h$	0.15	–	(Ozaki and Tajika, 2013)
Phosphate half saturation constant	$K_P$	$1 \times 10^{-6}$	mM	(Ozaki and Tajika, 2013)
Export ratio	$f_{exp}$	0.2	–	(Ozaki et al., 2019a)
Redfield C/P ratio	$\alpha^*$	106	mol mol <sup>-1</sup>	(Redfield et al., 1963)
Redfield N/P ratio	$\beta^*$	16	mol mol <sup>-1</sup>	(Redfield et al., 1963)
POM sinking velocity	$v_{POM}$	100	m d <sup>-1</sup>	(Ozaki et al., 2011)
Mass fraction of $G_1$	$m_1$	0.72	–	(Ozaki and Tajika, 2013)
Mass fraction of $G_2$	$m_2$	0.25	–	(Ozaki and Tajika, 2013)
Mass fraction of $G_3$	$m_3$	0.03	–	(Ozaki and Tajika, 2013)
Decomposition rate of $G_1$	$k_1$	0.6	d <sup>-1</sup>	(Ozaki et al., 2011)
Decomposition rate of $G_2$	$k_2$	0.1	d <sup>-1</sup>	(Ozaki et al., 2011)
Decomposition rate of $G_3$	$k_3$	0.0	d <sup>-1</sup>	(Ozaki et al., 2011)
Half saturation constant for aerobic respiration	$K_{O_2}$	$8 \times 10^{-3}$	mM	(Boudreau, 1996)
Half saturation constant for denitrification	$K_{NO_3}$	$3 \times 10^{-2}$	mM	(Boudreau, 1996)
Half saturation constant for MSR	$K_{MSR}$	0.2	mM	This study
Half saturation constant for AOM	$K_{AOM}$	0.093	mM	(Beal et al., 2011)
Aerobic oxidation rate of ammonium	$k_{R8}$	$1.825 \times 10^4$	mM <sup>-1</sup> yr <sup>-1</sup>	(Oguz et al., 2001)
Aerobic oxidation rate of sulfide	$k_{R9}$	$3.65 \times 10^3$	mM <sup>-1</sup> yr <sup>-1</sup>	(Oguz et al., 2001)
Aerobic methane oxidation rate	$k_{R10}$	$1 \times 10^7$	mM <sup>-1</sup> yr <sup>-1</sup>	(Van Cappellen and Wang, 1996)
Anaerobic methane oxidation rate	$k_{R11}$	$3 \times 10^{-4}$	yr <sup>-1</sup>	(Ozaki et al., 2019a)
Pyrite formation rate in the water column	$k_{pyr}^{wc}$	0.01	yr <sup>-1</sup>	This study
Reference value of seawater sulfate concentration	$[SO_4^{2-}]^*$	28.9	mM	(Ozaki et al., 2019a)



## 688 **Biological production**

689 The overall biogeochemical cycling scheme is based on the cycling of primary nutrient (phosphate;  $\text{PO}_4^{3-}$ ),  
690 which limits biological productivity—export production is related to the availability of P within the euphotic  
691 zone (Maier-Reimer, 1993; Shaffer et al., 2008; Yamanaka and Tajika, 1996):

$$j_{\text{exp}}^{\text{lh}} = \alpha^{\text{lh}} h_{\text{m}} \varepsilon^{\text{lh}} [\text{PO}_4^{3-}]^{\text{lh}} \frac{[\text{PO}_4^{3-}]^{\text{lh}}}{[\text{PO}_4^{3-}]^{\text{lh}} + K_{\text{p}}}, \quad (21)$$

692 where  $j_{\text{exp}}$  represents new/export production of POC (in unit of  $\text{mol C m}^{-2} \text{ yr}^{-1}$ ),  $\alpha$  denotes C:P stoichiometry  
693 of POM,  $h_{\text{m}}$  is the mixed layer depth,  $\varepsilon$  denotes the assimilation efficiency factor for P uptake, and  $K_{\text{p}}$  denotes  
694 the half-saturation constant. The value of  $\varepsilon$  for the low-mid latitude region is assumed to be 1. In contrast, we  
695 assume a lower efficiency for high latitude region because biological production tends to be limited by  
696 environmental factors other than phosphate availability (e.g., amount of solar radiation, mixed layer thickness,  
697 sea-ice formation, and iron availability). This is used as one of the fitting parameters in the model.  
698 Downwelling waters contain a certain level of nutrients (i.e., preformed nutrients).

699

700 In our standard run, the stoichiometry of organic matter is parameterized using the canonical Redfield ratio  
701 (C:N:P = 106:16:1) (Redfield et al., 1963). However, we note that flexible C:N:P stoichiometry has been the  
702 subject of recent discussion. In the modern oceans, C:N:P ratios of exported POM vary across latitude,  
703 reflecting ecosystem structure (Galbraith and Martiny, 2015). Local observations (and laboratory experiments)  
704 suggest that the C:N:P ratio of cyanobacteria is a function of seawater  $\text{PO}_4^{3-}$  concentration (Larsson et al.,  
705 2001). The evolutionary perspective has also been discussed (Quigg et al., 2003; Sharoni and Halevy, 2022).  
706 In the previous version of the CANOPS model, the C-N-P stoichiometry of primary producers responds  
707 dynamically to P availability in the surface layer (Reinhard et al., 2017b):

$$\alpha = \alpha^* + \frac{\alpha_{\text{max}} - \alpha^*}{2} \left( 1 + \tanh \left( \frac{\gamma_{\text{PO}} - [\text{PO}_4^{3-}]}{\gamma_{\text{PI}}} \right) \right), \quad (22)$$

$$\beta = \beta^* + \frac{\beta_{\text{max}} - \beta^*}{2} \left( 1 + \tanh \left( \frac{\gamma_{\text{PO}} - [\text{PO}_4^{3-}]}{\gamma_{\text{PI}}} \right) \right), \quad (23)$$



708 where  $\alpha$  and  $\beta$  represent the C/P ratio and N/P ratio of POM, \* denotes the canonical Redfield ratios, max  
709 denotes the maximum value ( $\alpha_{\max} = 400$  and  $\beta_{\max} = 60$ ), and  $\gamma_{P0}$  and  $\gamma_{P1}$  are tunable constants ( $\gamma_{P0} = 0.1 \mu\text{M}$   
710 and  $\gamma_{P1} = 0.03 \mu\text{M}$ ) (Kuznetsov et al., 2008). In the CANOPS-GRB model, this dynamic response of POM  
711 stoichiometry can be explored by changing the user-flag from the standard static response. In this study, we  
712 do not explore the impacts of flexible POM stoichiometry on global biogeochemistry (i.e.,  $\alpha_{\max} = \alpha^*$  and  $\beta_{\max}$   
713  $= \beta^*$ ).

714

715 Biological production in the surface mixed layer increases the concentration of dissolved  $\text{O}_2$  and reduces the  
716 concentrations of DIP and DIN according to the stoichiometric ratio (R1 and R2; Table 1). DIN consumption  
717 is partitioned between nitrate and ammonium, assuming that ammonium is preferentially assimilated.  
718 CANOPS-GRB evaluates the availability of fixed N in the surface ocean, and any N deficiency required for a  
719 given level of productivity is assumed to be compensated for on geologic time scales by N fixers. In other  
720 words, it is assumed that biological N fixation keeps pace with P availability, so that P (not N) ultimately  
721 determines oceanic biological productivity.

722

723 To date, models of varying orders of complexity have been developed to simulate oceanic primary production  
724 and nutrient cycling in the euphotic layer, from a single nutrient and single phytoplankton component system  
725 to the inclusion of multiple nutrients and trophic levels in the marine ecosystem, usually coupled to physical  
726 models (e.g., Oguz et al., 2000; Yakushev et al., 2007). To avoid this level of complexity, we introduce a  
727 parameter,  $f_{\text{exp}}$ , called export ratio (Sarmiento and Gruber, 2006), which relates the flux densities of export  
728 production and NPP, as follows:

$$j_{\text{NPP}}^{\text{ocn}} = \frac{j_{\text{exp}}}{f_{\text{exp}}}, \quad (24)$$

729 where  $j_{\text{NPP}}^{\text{ocn}}$  denotes the NPP in terms of  $\text{mol C m}^{-2} \text{yr}^{-1}$ . In the modern ocean globally averaged value of  $f_{\text{exp}}$   
730 is estimated at 0.2 (Laws et al., 2000), and we assumed this value in this study. The rate of recycling of organic  
731 matter in the photic zone is thus given by



$$j_{\text{recy}} = j_{\text{NPP}}^{\text{ocn}} - j_{\text{exp}} = \frac{1 - f_{\text{exp}}}{f_{\text{exp}}} j_{\text{exp}}. \quad (25)$$

732 The respiration pathway of  $j_{\text{recy}}$  depends on the availability of terminal electron acceptors ( $\text{O}_2$ ,  $\text{NO}_3^-$  and  $\text{SO}_4^{2-}$ ).  
733 Following exhaustion of these species as terminal electron acceptors, organic matter remineralization occurs  
734 by methanogenesis (R7). See below for the treatment of organic matter remineralization in the water column.

### 735 **Biological pump**

736 Most POM exported to the deep sea is remineralized in the water column before reaching the seafloor (e.g.,  
737 Broecker and Peng, 1982). Nutrients returning to seawater at intermediate depths may rapidly return to the  
738 surface ocean and support productivity. The remaining fraction of POM that reaches the sediment ultimately  
739 exerts an important control on oceanic inventories of nutrients and  $\text{O}_2$ . An adequate representation of the  
740 strength of biological pump is therefore critical to any descriptions of global biogeochemical cycles.

741

742 The governing equation of the concentration of biogenic particles  $G$  is

$$\frac{\partial G}{\partial t} + v_{\text{POM}} \frac{\partial G}{\partial z} = -rG \quad (26)$$

743 where  $r$  is a decomposition rate and  $v_{\text{POM}}$  is the settling velocity of POM in the water column. We assume a  
744 settling velocity of  $100 \text{ m d}^{-1}$  for our reference value (e.g., Suess, 1980), although a very wide range of values  
745 and depth-dependency have been reported (e.g., Berelson, 2001b). Therefore, the settling velocity is fast  
746 enough to neglect advective and diffusive transport of biogenic particles. Note that the settling velocity would  
747 affect the intensity of biological pump and chemical distribution in the ocean interior. Considering the ballast  
748 hypothesis in the modern ocean (Armstrong et al., 2001; Francois et al., 2002; Ittekkot, 1993; Klaas and Archer,  
749 2002), the settling velocity of POM in the geological past would have been different from the modern ocean.  
750 As Kashiyama et al. (2011) pointed out, there would be a critical aspect among sinking rate of POM, intensity  
751 of biological pump and chemical distribution in the ocean. The quantitative and comprehensive evaluation of  
752 their effect is an important issue for the future work (Fakhraee et al., 2020).

753



754 In order to solve equation (26) explicitly, a relatively small time step (~1 day) would be required. However,  
755 because the sinking velocity and remineralization of biogenic material are fast processes, we assume that the  
756 POM export and remineralization occurs in the same time step (ignoring the term  $\partial G/\partial t$ ). Then the  
757 concentration of biogenic particles can be solved as follows:

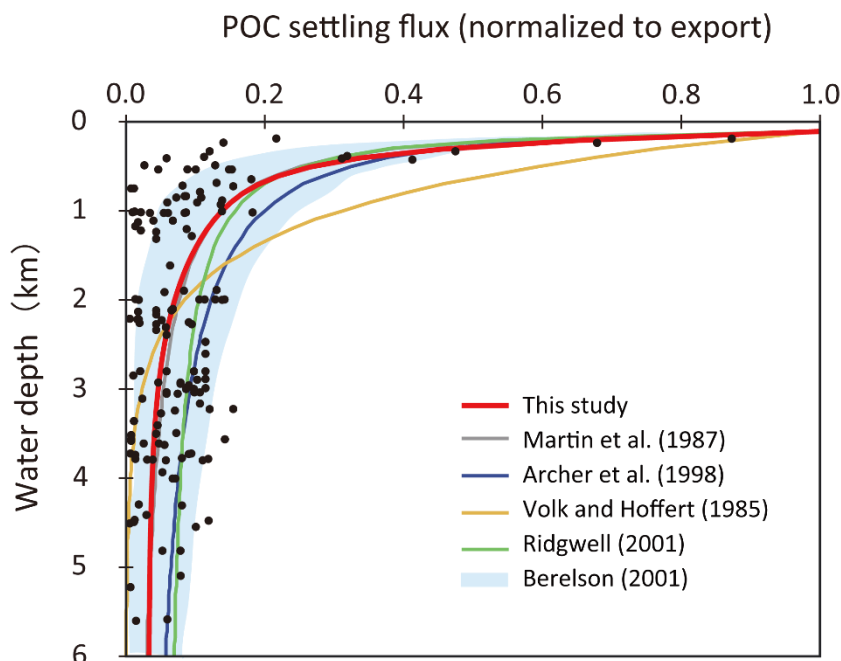
$$G(z + \Delta z) = G(z) \exp\left(-\frac{r\Delta z}{v_{\text{POM}}}\right). \quad (27)$$

758 where  $\Delta z$  is a spatial resolution of the model.

### 759 **Organic matter decomposition**

760 As POM settles through the water column, it is nearly entirely decomposed back to dissolved tracers.  
761 Therefore, decomposition of POM is a key process for modelling biogeochemistry in the ocean. To avoid the  
762 complex treatment of this process (such as repackaging and aggregation/dispersal of particles), various  
763 empirical schemes for POM sinking flux have been proposed, such as exponential (Volk and Hoffert, 1985)  
764 or power law (Martin et al., 1987) functions (Fig. 5). However, the estimation of Volk and Hoffert generally  
765 tends to overestimate in the upper water column (<1.5 km) and underestimate at depth. It is important to note  
766 that data series of sediment trap measurements were obtained from a limited geographic and depth range.  
767 Berelson (2001a) and Lutz et al. (2002) conducted further estimates of the sediment flux and found regional  
768 variability in the sinking flux. Broadly, these data indicate that commonly applied flux relationships generally  
769 tend to overestimate flux to depth.

770



771

772 **Figure 5** Empirical relationships between POC settling flux normalized to export production (Lutz et al.,  
773 2002) and water depth (Archer et al., 1998; Berelson, 2001a; Martin et al., 1987; Volk and Hoffert, 1985).  
774 The profile of the CANOPS-GRB model is depicted as a red line. The black dots represent observational data  
775 (Honjo, 1980; Honjo and Manganini, 1993; Lutz et al., 2002; Tsunogai and Noriki, 1991, and references  
776 therein).

777

778 The microbial degradation of different groups of organic matter with different labilities differs over timescales  
779 ranging from hours to millions of years. In order to represent the decrease in POM lability with time and water  
780 depth, we adopt the so-called multi-G model (Westrich and Berner, 1984) that describes the detailed kinetics  
781 of organic matter decomposition (Ozaki and Tajika, 2013; Ozaki et al., 2011). In the CANOPS model, POM  
782 is described using two degradable fractions ( $G_1$  and  $G_2$ ) and one inert ( $G_3$ ) fraction using different rate  
783 constants  $k_i$  ( $i=1, 2, 3$ ) for each component. Rate constants are tuned on the basis of consistency with the  
784 typical profile of the POM sinking flux estimated from sediment trap studies (Fig. 5). In this study, constant  
785 stoichiometries between C, N, and P during the remineralization of POM are assumed throughout the water  
786 column, taking values equal to those characterizing mean export production.

787



788 The electron acceptor used in the respiration reaction changes from dissolved  $O_2$  to other oxidants (e.g.,  $NO_3^-$   
789 and  $SO_4^{2-}$ ) as  $O_2$  becomes depleted. The respiration pathway is controlled by the free energy change per mole  
790 of organic carbon oxidized. The organic matter decomposition is performed by the oxidant which yields the  
791 greatest free energy change per mole of organic carbon oxidized. When the oxidant is depleted, further  
792 decomposition will proceed utilizing the next most efficient (i.e., the most energy producing) oxidant until  
793 either all oxidants are consumed or oxidizable organic matter is depleted (e.g., Berner, 1989; Froelich et al.,  
794 1979). In oxic waters, organic matter is remineralized by an aerobic oxidation process (R4). As dissolved  $O_2$   
795 is depleted,  $NO_3^-$  and/or  $SO_4^{2-}$  will be used (R5 and R6). Denitrification is carried out by heterotrophic bacteria  
796 under low concentrations of dissolved  $O_2$ , if there is sufficient nitrate. For anoxic, sulfate-lean oceans, organic  
797 matter production from carbon dioxide (methanogenesis) or fermentation of organic matter to produce  
798 methane and carbon dioxide will occur (R7). In the CANOPS-GRB model, we parameterized the dependence  
799 of decomposition of POM with a Michaelis-Menten type relationship with respect to the terminal electron  
800 acceptors:

$$R_4 = \frac{[O_2]}{K_{O_2} + [O_2]} (\sum k_i G_i) \quad (28)$$

$$R_5 = \frac{K'_{O_2}}{K'_{O_2} + [O_2]} \frac{[NO_3^-]}{K_{NO_3} + [NO_3^-]} (\sum k_i G_i) \quad (29)$$

$$R_6 = \frac{K'_{O_2}}{K'_{O_2} + [O_2]} \frac{K'_{NO_3}}{K'_{NO_3} + [NO_3^-]} \frac{[SO_4^{2-}]}{K_{MSR} + [SO_4^{2-}]} (\sum k_i G_i) \quad (30)$$

$$R_7 = \frac{K'_{O_2}}{K'_{O_2} + [O_2]} \frac{K'_{NO_3}}{K'_{NO_3} + [NO_3^-]} \frac{K'_{MSR}}{K'_{MSR} + [SO_4^{2-}]} (\sum k_i G_i) \quad (31)$$
$$= (1 - R_{O_2} - R_{NO_3} - R_{SO_4}) (\sum k_i G_i)$$

801 where  $K_{O_2}$ ,  $K_{NO_3}$ , and  $K_{MSR}$  are Monod constants, and  $K'_{O_2}$ ,  $K'_{NO_3}$ ,  $K'_{MSR}$  are inhibition constants. The Monod-  
802 type expressions are most widely used in mathematical models of POM decomposition processes (e.g.,  
803 Boudreau, 1996). The oxidants for organic matter decomposition change gradually, depending on the amount  
804 of each oxidant. The parameter values are based on the previous studies on early diagenetic processes in  
805 marine sediments (Boudreau, 1996; Van Cappellen and Wang, 1996).  $SO_4^{2-}$  has been one of the major



806 components of the Phanerozoic oceans and has been an important oxidizing agent in anaerobic systems. In  
807 the original CANOPS model (Ozaki and Tajika, 2013; Ozaki et al., 2011), it was assumed that the saturation  
808 constant  $K_{MSR}$  is zero, meaning that the  $SO_4^{2-}$  is never a limiting factor. In contrast, during the Precambrian,  
809 seawater  $SO_4^{2-}$  could have been extremely low (Lyons and Gill, 2010). The half saturation constant for MSR  
810 ( $K_{MSR}$ ) determines the degree to which MSR contributes to the total respiration rates. However, estimates for  
811  $K_{MSR}$  in natural environments and pure cultures vary over several orders of magnitude ( $\sim 0.002$ – $3$  mM) (Pallud  
812 and Van Cappellen, 2006; Tarpgaard et al., 2011). We assume a reference value of  $0.2$  mM for this study.

813

814 Finally, temperature may also have played an important role in organic matter decomposition rates. The  
815 dependence of ammonification on temperature is sometimes described by an exponential function or  $Q_{10}$   
816 function (e.g., Yakushev et al., 2007). While we recognize that the temperature dependency of organic matter  
817 decomposition might have played an important role in oceanic biogeochemical cycles in geological past  
818 (Crichton et al., 2021), these dynamics are not included in our standard model.

## 819 **Secondary redox reactions**

820 Total ammonia ( $\Sigma NH_3$ ), total sulfide ( $\Sigma H_2S$ ), and methane ( $CH_4$ ), produced during organic matter degradation,  
821 are subject to oxidation by  $NO_3^-$ ,  $SO_4^{2-}$ , and  $CO_2$  via a set of secondary redox reactions (Table 1). Rate  
822 constants for these reactions are taken from the literature. The ocean model includes nitrification (R8), total  
823 sulfide oxidation by  $O_2$  (R9), aerobic oxidation of  $CH_4$  by  $O_2$  (R10), and AOM by  $SO_4^{2-}$  (R11). Nitrification,  
824 the oxidation of ammonium to nitrate, occurs in several stages and is accomplished mainly by  
825 chemolithotrophic bacteria (Sarmiento and Gruber, 2006). In this study, we treat all nitrification reactions as  
826 a combined reaction (R8). The rate of this process is assumed to depend on the concentration of both oxygen  
827 and ammonia as follows:

$$R_8 = k_{R8} [NH_4^+] [O_2]. \quad (32)$$

828

829 The oxidation of sulfide formed in anoxic waters by MSR can also be written as a series of reactions (e.g.,  
830 Yakushev and Neretin, 1997), but we treat it as an overall reaction (R9). The rate of this secondary redox  
831 reaction is also formulated using bimolecular rate law:



$$R_9 = k_{R9}[\Sigma H_2S][O_2]. \quad (33)$$

832 The rate constant for this process has been shown to vary significantly as a function of several redox-sensitive  
833 trace metals which act as catalysts (Millero, 1991). Here we assume  $k_{R9} = 3650 \text{ mM}^{-1} \text{ yr}^{-1}$  based on the  
834 observations of suboxic layer of the Black Sea (Oguz et al., 2001).

835

836 In the original CANOPS model (Ozaki et al., 2019a; Ozaki and Tajika, 2013), syngenetic pyrite formation in  
837 the water column was not considered. In a more recent revision of the model, this process was added (Cole et  
838 al., 2022) and parameterized such that iron sulfide formation is assumed to be proportional to the hydrogen  
839 sulfide concentration:

$$R_{\text{pyr}}^{\text{wc}} = k_{\text{pyr}}^{\text{wc}}[\Sigma H_2S], \quad (34)$$

840 where  $k_{\text{pyr}}^{\text{wc}}$  is a model constant (its reference value is set at  $0.01 \text{ yr}^{-1}$ ). This constant is a function of the ferrous  
841 iron concentration in seawater, but it is the subject of large uncertainty. The total flux (in  $\text{mol S yr}^{-1}$ ) can be  
842 obtained by integrating the precipitation flux density over the whole ocean:

$$J_{\text{pyr}}^{\text{wc}} = \int R_{\text{pyr}}^{\text{wc}} \frac{dV}{dz} dz. \quad (35)$$

843

844  $\text{CH}_4$  can be oxidized not only by  $\text{O}_2$  in aerobic waters (R10) but by  $\text{SO}_4$  in anoxic waters (R11). The aerobic  
845 oxidation of  $\text{CH}_4$  is formulated using a bimolecular rate law:

$$R_{10} = k_{R10}[\text{CH}_4][\text{O}_2]. \quad (36)$$

846 The rates of AOM is formulated using a Monod-type law (Beal et al., 2011):

$$R_{11} = k_{R11}[\text{CH}_4] \frac{[\text{SO}_4^{2-}]}{K_{\text{AOM}} + [\text{SO}_4^{2-}]}. \quad (37)$$

847 Rate constants for above reactions are taken from the literature (Table 4). Secondary redox reactions were  
848 calculated implicitly with an operator splitting scheme (Steeffel and MacQuarrie, 1996) so as to maintain  
849 numerical stability.



#### 850 2.4.4 Sediment-water exchange

851 The burial of biogenic material in marine sediments plays a critical role in global biogeochemical cycles,  
 852 especially with respect to the marine budgets of nutrients, carbon, and sulfur. This is intimately linked to  
 853 atmospheric O<sub>2</sub> levels on geologic timescales. Specifically, the burial rate of C<sub>org</sub> in marine sediments exerts  
 854 a primary control on the evolution of atmospheric O<sub>2</sub> levels throughout Earth's history. Given the complexity  
 855 of biogeochemical processes within sediments and our limited knowledge on many of the early diagenetic  
 856 processes, we adopt some semi-empirical relationships extracted from ocean sediment data. This approach,  
 857 rather than explicit modelling, is also required to reduce the computational cost of the simulation on timescales  
 858 >100 Myr. The related parameter values are in Table 5.

859

860 Table 5: Parameters used in the sediment-water interface module of CANOPS-GRB.

Parameters	Label	Value	Unit	Ref.
Scale constant for benthic aerobic respiration	$k$	0.02	yr <sup>-1</sup>	(Ozaki et al., 2019a)
Burial efficiency of C <sub>org</sub> at zero sediment accumulation rate	$be_1$	5.0	%	(Dale et al., 2012)
Burial efficiency of C <sub>org</sub> at infinite sediment accumulation rate	$be_2$	75	%	(Dale et al., 2012)
Centre of the regression for burial efficiency of organic C	$a$	0.01	g cm <sup>-2</sup> yr <sup>-1</sup>	(Dale et al., 2012)
Pyrite burial efficiency in oxic sediments	$e_{\text{pyr}}^{\text{oxic}}$	0.117	–	This study
Pyrite burial efficiency in anoxic sediments	$e_{\text{pyr}}^{\text{anox}}$	1	–	(Ozaki et al., 2019a)
O <sub>2</sub> threshold value for P burial efficiency	$oxic$	0.25	mM	(Ozaki et al., 2011)
C <sub>org</sub> /N <sub>org</sub> ratio of buried sediments	(C <sub>org</sub> /N <sub>org</sub> ) <sub>b</sub>	10	mol mol <sup>-1</sup>	(Ozaki and Tajika, 2013)

#### 861 POM deposition

862 The fraction of settling POM that reaches the sediment surface,  $J_{\text{org}}^{\text{dep}}$  (in mol C yr<sup>-1</sup>) is a function of both the  
 863 settling flux density,  $j_{\text{org}}^{\text{dep}}$  (in mol C m<sup>-2</sup> yr<sup>-1</sup>), and topography (Fig. 4a):

$$J_{\text{org}}^{\text{dep}} = \int_{z_1}^{z_2} j_{\text{org}}^{\text{dep}}(z) \frac{dA}{dz} dz, \quad (38)$$

864 where the settling flux density can be written as follows:

$$j_{\text{org}}^{\text{dep}} = v_{\text{POM}} G. \quad (39)$$

865 where  $G$  is the concentration of POM, and  $v_{\text{POM}}$  denotes the sinking velocity.



## 866 Carbon cycling

867 Interactions between the ocean and underlying sediments play an important role in influencing whole-ocean  
868 chemical and nutrient inventories on geologic time scales. POM deposited to the seafloor is subject to  
869 decomposition during diagenetic processes associated with burial in marine sediments. Only a small fraction  
870 of organic matter will ultimately be buried and removed from the surface environment. However,  
871 understanding what factors control the preservation of organic matter in marine sediments has been a  
872 controversial topic, and we still lack a robust understanding of this process. With this issue in mind, we adopt  
873 an empirical approach obtained using the observational data from previous studies.

874

875 The burial flux density of  $C_{\text{org}}$  at each water depth,  $j_{\text{org}}^{\text{b,ocn}}$  (in terms of  $\text{mol C m}^{-2} \text{ yr}^{-1}$ ), is calculated based on  
876 burial efficiency,  $BE_{\text{org}}$ :

$$j_{\text{org}}^{\text{b,ocn}} = BE_{\text{org}} j_{\text{org}}^{\text{dep}}. \quad (40)$$

877 Burial efficiency is defined as the fraction of organic matter buried in sediments relative to the total  
878 depositional flux. Burial efficiency is described by simplified parametric laws based on empirical relationships  
879 from modern day observations. Previous studies demonstrate strong dependency of this term on total  
880 sedimentation rate,  $SR$  (e.g., Henrichs and Reeburgh, 1987). Figure 6 demonstrates the relationship between  
881  $BE_{\text{org}}$  and  $SR$  compiled from literature surveys. The sedimentation rate in the modern ocean varies over about  
882 five orders of magnitude, with a primary dependence on material supplied from the continents. There is a  
883 strong relationship, especially for  $SR$  less than  $0.01 \text{ cm yr}^{-1}$ . In contrast to the strong  $SR$  dependence under  
884 oxic conditions, anoxic settings show a much weaker dependence of  $BE_{\text{org}}$  on  $SR$  (Betts and Holland, 1991;  
885 Henrichs and Reeburgh, 1987) (Fig. 6). In this study, the following relationship proposed by (Henrichs and  
886 Reeburgh, 1987) is adopted for sediments underlying well-oxygenated bottom water ( $\text{O}_2$  concentration of  
887 bottom water,  $[\text{O}_2]_{\text{bw}} > 200 \mu\text{M}$ ):

$$BE_{\text{org}} = \frac{SR^{0.4}}{2.1}. \quad (41)$$

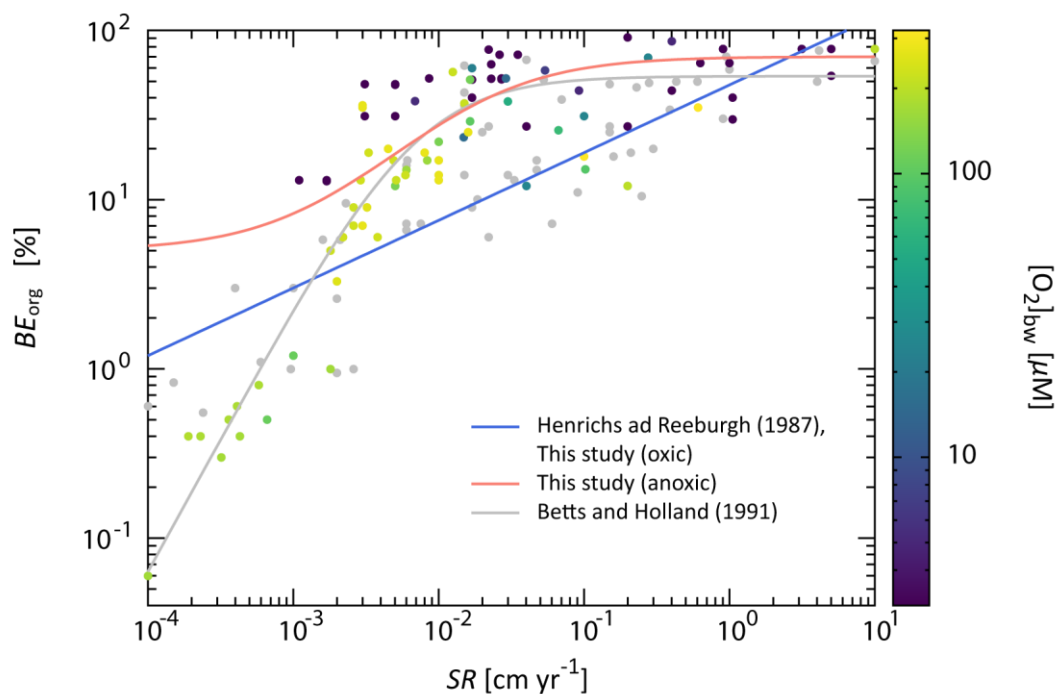
888 Given that  $BE_{\text{org}}$  depends on the  $[\text{O}_2]_{\text{bw}}$  (Katsev and Crowe, 2015; Lasaga and Ohmoto, 2002), we adopt the  
889 following formulation for sediments underlying less-oxygenated bottom waters ( $[\text{O}_2]_{\text{bw}} < 30 \mu\text{M}$ ) (Dale et al.,  
890 2012):



$$BE_{\text{org}} = b_2 + \frac{b_1 - b_2}{1 + SR/a}, \quad (42)$$

891 where  $a = 0.019$ ,  $b_1 = 0.05$ , and  $b_2 = 0.7$ , respectively. For intermediate  $[O_2]_{\text{bw}}$  levels,  $BE_{\text{org}}$  is evaluated as a  
 892 function of  $[O_2]_{\text{bw}}$  with a log-linear interpolation method. Note that the original CANOPS model (Ozaki and  
 893 Tajika, 2013; Ozaki et al., 2011) adopted Eq. (41) without considering the  $O_2$  dependency, whereas more  
 894 recent versions employ Eq. (42) for both oxic and anoxic sediments with different values of  $a$ ,  $b_1$  and  $b_2$ . In  
 895 the CANOPS-GRB, we adopted both equations, because of the sake of more accurate reproduction of  $C_{\text{org}}$   
 896 burial distribution in the modern ocean (Sect. 3.2.2).

897



898

899 **Figure 6** Burial efficiency of organic carbon ( $BE_{\text{org}}$ ) as a function of sedimentation rate ( $SR$ ). The dots denote  
 900 the observational data compiled from literature survey (Betts and Holland, 1991; Canfield, 1993; Hartnett et  
 901 al., 1998; Henrichs and Reeburgh, 1987; Tromp et al., 1995). The color represents the  $O_2$  concentration of  
 902 bottom water,  $[O_2]_{\text{bw}}$ , with grey dots for the unknown  $[O_2]_{\text{bw}}$  value. Black and grey solid lines are previously  
 903 proposed empirical relationships (Betts and Holland, 1991; Henrichs and Reeburgh, 1987), whereas blue and  
 904 red lines are the relationship for well-oxygenated ( $[O_2]_{\text{bw}} > 200 \mu\text{M}$ ) and anoxic ( $[O_2]_{\text{bw}} < 30 \mu\text{M}$ ) marine  
 905 sediments adopted in the CANOPS-GRB model.

906



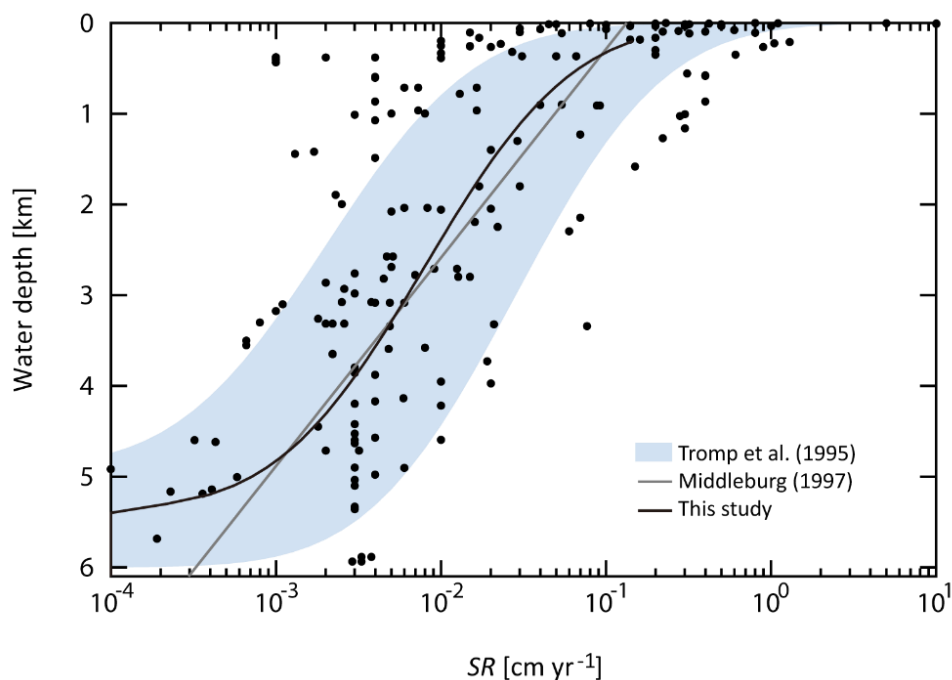
907 Sedimentation rate depends strongly on water depth and distance from shore (Hedges et al., 1999), and we  
908 apply the relationship between water depth,  $z$ , and the reference value of  $SR$  shown by Tromp et al. (1995)  
909 (Fig. 7).

$$z = 2700 \times \operatorname{erfc}(2.1 + \log SR^*). \quad (43)$$

910 Using these formulas with seafloor topography (Fig. 4a) and  $j_{\text{org}}^{\text{dep}}$  (Eq. 39), we can calculate  $j_{\text{org}}^{\text{b,ocn}}$  for each  
911 ocean depth. In the CANOPS-GRB model, we also introduce an erosion factor,  $f_R$ , representing the global  
912 weathering/sedimentation rate (Sect. 2.4.3). Given the intimate coupling between global erosion rate and mass  
913 transfer from continents to the ocean,  $SR$  scales with the erosion factor ( $f_R = 1$  for our reference run):

$$SR(z) = f_R SR(z)^*. \quad (44)$$

914



915

916 **Figure 7** Sedimentation rate as a function of water depth. Data (black dots) were compiled from literature  
917 survey (Baturin, 2007; Betts and Holland, 1991; Cha et al., 2005; Colman et al., 2000; Reimers et al., 1992;  
918 Tromp et al., 1995). Black line represents the relationship assumed in the CANOPS-GRB model. Previously  
919 estimated empirical relationships (Middelburg et al., 1997; Tromp et al., 1995) are also shown.

920



921 Organic matter that is not buried is subject to decomposition. The decomposition rate at each water depth is  
922 given as follows:

$$j_{\text{recy}}^{\text{sed}} = j_{\text{org}}^{\text{dep}} - j_{\text{org}}^{\text{b,ocn}} = (1 - BE_{\text{org}}) j_{\text{org}}^{\text{dep}}. \quad (45)$$

923 The respiration pathway used in the benthic decomposition is evaluated based on semi-empirical relationships  
924 obtained by 1-D early diagenesis models (see below). The degradation of organic matter in sediments is  
925 coupled to the availability of terminal electron acceptors, such as  $\text{O}_2$ ,  $\text{NO}_3^-$ , and  $\text{SO}_4^{2-}$  in the water column.  
926 The fraction of aerobic degradation in total sedimentary respiration,  $f_{\text{aero}}$ , is calculated based on oxygen  
927 exposure time ( $\tau_{\text{OET}}$ ):

$$f_{\text{aero}} = (1 - f_{\text{deni}})(1 - e^{-k\tau_{\text{OET}}}), \quad (46)$$

928 where  $f_{\text{deni}}$  denotes the fraction of denitrification and  $k$  is an empirical constant.  $\tau_{\text{OET}}$  is given by

$$\tau_{\text{OET}} = \frac{\text{OPD}}{SR}, \quad (47)$$

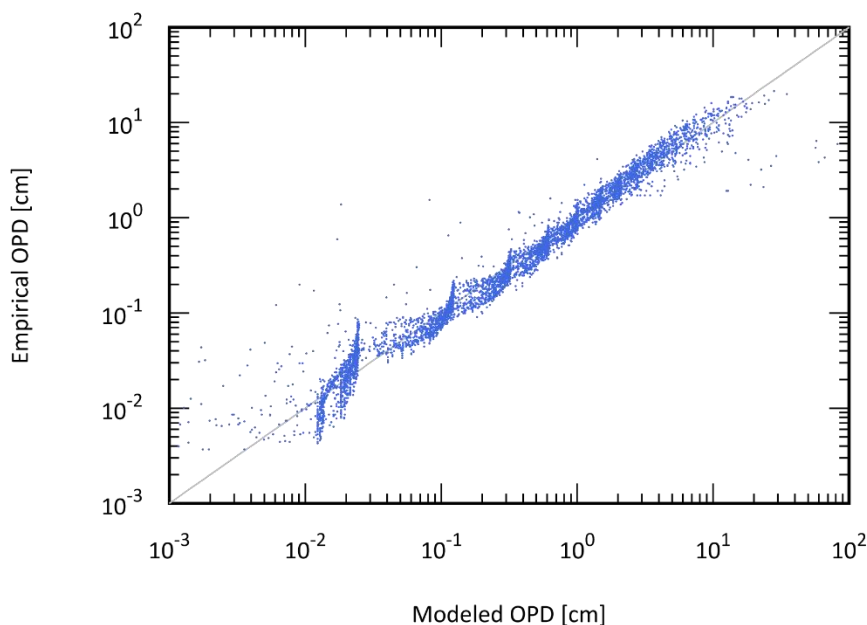
929 where OPD is the oxygen penetration depth (cm) and  $SR$  denotes a linear sedimentation rate ( $\text{cm yr}^{-1}$ ). In the  
930 CANOPS-GRB model OPD is calculated by a simplified parametric law obtained from a 1-D early-diagenetic  
931 model of C and  $\text{O}_2$ . We performed a series of experiments ( $n = 5,652$ ) in order to parameterize OPD as a  
932 polynomial function with the following variables: sedimentation rate  $SR$  ( $\text{cm yr}^{-1}$ ), bottom water  $\text{O}_2$   
933 concentration  $[\text{O}_2]_{\text{bw}}$  ( $\mu\text{M}$ ), depositional flux of POC  $j_{\text{org}}^{\text{dep}}$  ( $\text{mmol C cm}^{-2} \text{yr}^{-1}$ ) and bottom water temperature  
934  $T_{\text{bw}}$  ( $^{\circ}\text{C}$ ). The variables are allowed to vary over a parameter space spanning  $10^{-4} \text{ cm yr}^{-1} < SR < 10^1 \text{ cm yr}^{-1}$ ,  
935  $10^0 \mu\text{M} < [\text{O}_2]_{\text{bw}} < 10^3 \mu\text{M}$ ,  $10^{-4} \text{ mmol C cm}^{-2} \text{yr}^{-1} < j_{\text{org}}^{\text{dep}} < 10^1 \text{ mmol C cm}^{-2} \text{yr}^{-1}$ , and  $0 \text{ }^{\circ}\text{C} < T_{\text{bw}} < 30 \text{ }^{\circ}\text{C}$ .

$$\begin{aligned} \log \text{OPD} = & a_0 + a_1 \log SR + a_2 \log [\text{O}_2]_{\text{bw}} + a_3 \log j_{\text{org}}^{\text{dep}} + a_4 (\log SR)^2 \\ & + a_5 (\log [\text{O}_2]_{\text{bw}})^2 + a_6 (\log j_{\text{org}}^{\text{dep}})^2 + a_7 (\log SR)(\log [\text{O}_2]_{\text{bw}}), \\ & + a_8 (\log [\text{O}_2]_{\text{bw}})(\log j_{\text{org}}^{\text{dep}}) + a_9 (\log SR)(\log j_{\text{org}}^{\text{dep}}) + a_{10} T_{\text{bw}} \end{aligned} \quad (48)$$

936 where  $a_0 = -2.24869$ ,  $a_1 = 0.110645$ ,  $a_2 = 1.12569$ ,  $a_3 = -0.281005$ ,  $a_4 = 0.014827$ ,  $a_5 = -0.124721$ ,  $a_6 =$   
937  $0.0894604$ ,  $a_7 = 0.00279531$ ,  $a_8 = -0.127797$ ,  $a_9 = 0.0017995$ , and  $a_{10} = 0.0085171$ . This parametric fit  
938 provides a rapid means of obtaining OPD from a 1-D early diagenetic model of C and  $\text{O}_2$  (Fig. 8). Note that  
939 Eq. (48) is verified for  $[\text{O}_2]_{\text{bw}} > 1 \mu\text{M}$ . When bottom water  $\text{O}_2$  concentration is lower than  $1 \mu\text{M}$ , OPD is set at  
940 zero.



941



942

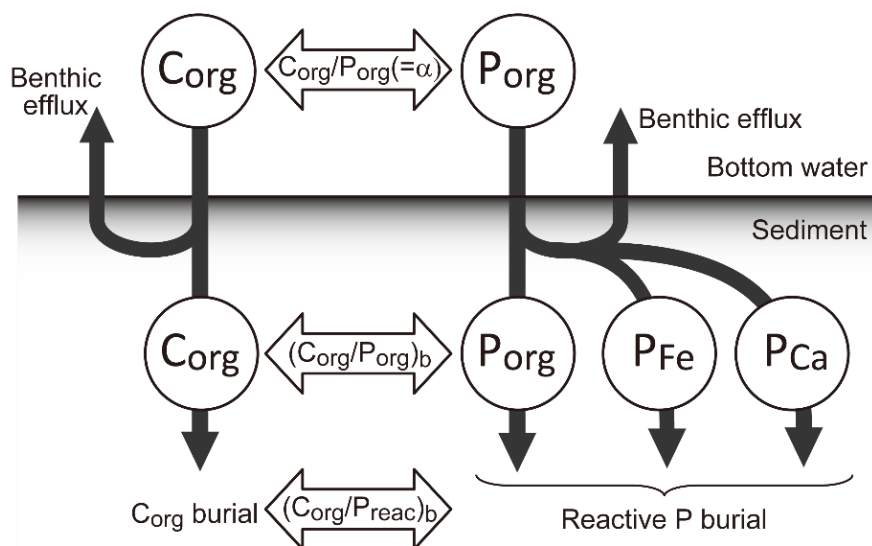
943 **Figure 8** The correlation between the simulated OPD and the OPD obtained from an empirical relationship of  
944 equation (48) ( $n = 5652$ ). Gray line denotes the 1:1 line.  $r^2 = 0.9595$ .

945

## 946 Phosphorus cycling

947 Marine P inventory is controlled not only by the riverine P input flux from land but also by the efficiency of  
948 P recycling in marine sediments (Van Cappellen and Ingall, 1994). Because the estimated P diffusive flux  
949 from seafloor sediments is much greater than the riverine P flux (Delaney, 1998; Hensen et al., 1998;  
950 McManus et al., 1997; Ruttenger, 2003; Wallmann, 2003a; Wallmann, 2010a), changes in diagenetic  
951 processes affecting P recycling and burial in marine sediments could have a significant impact on global  
952 oceanic biogeochemical cycles.

953



954

955 **Figure 9** Schematic of P burial in marine sediments. The primary source of P to the sediment is the deposition  
956 of organic matter, which represents the C:P ratio of primary producers,  $\alpha$ . Most of the deposited organic P is  
957 decomposed before burial and the DIP released to pore waters diffuses to the bottom water. A fraction of the  
958 liberated P is trapped by iron hydroxides or buried as authigenic minerals (e.g., carbonate fluorapatite).  
959 Phosphorus deposited in sediments is a subject of decomposition and sink-switching. Three reactive phases,  
960 organic P ( $P_{org}$ ), Fe-sorbed P ( $P_{Fe}$ ), and Ca-bound P ( $P_{Ca}$ ), are considered in the CANOPS-GRB model. The  
961 burial of these species are redox-dependent: burial efficiency is affected by bottom water  $O_2$  concentration.  
962 Because of the sink-switching, sedimentary  $C_{org}/P_{react}$ , rather than  $C_{org}/P_{org}$  ratios, provides a correct measure  
963 of the retention versus diffusive loss of remineralized P.  
964

965 A schematic of benthic P cycling is shown in Fig. 9. The majority of organic matter delivered to the sediment-  
966 water interface is regenerated (Jahnke, 1996), but a fraction of DIP released via respiration to pore waters is  
967 redistributed to other phases such as iron-hydroxide or carbonate fluorapatite within the sediments. This  
968 mechanism is known as ‘sink-switching’ (e.g., Anderson et al., 2001; Filippelli, 2001), and results in P burial  
969 other than organic P playing a more important role in the total P sink (Compton et al., 2000; Ruttenberg, 2003,  
970 1993a). Three different P pools are considered in the CANOPS-GRB model: organic P ( $P_{org}$ ), Fe-hydroxide-  
971 sorbed P ( $P_{Fe}$ ), and authigenic Ca-bound P ( $P_{Ca}$ ). The sum of these pools is defined as biologically reactive P  
972 ( $P_{react}$ ) (bioavailable in the ocean to fuel primary productivity). The marine C and P cycles are coupled not only  
973 through the  $C_{org}/P_{org}$  ratio of POM ( $\alpha$ ) but also through the  $C_{org}/P_{react}$  ratio of marine sediments. It is important  
974 to note that as argued by Anderson et al. (2001), the fundamental measure of the retention versus diffusive  
975 loss of remineralized P is not the sedimentary  $C_{org}/P_{org}$  ratio, but the ratio of  $C_{org}/P_{react}$ .



976

977 Field observations of marine and lacustrine sediments have revealed that the burial efficiency of P depends on  
 978 the redox conditions of bottom waters (Ingall and Jahnke, 1994): Phosphorus retention potential is suppressed  
 979 under anoxic bottom water conditions. Elevated  $C_{\text{org}}/P_{\text{reac}}$  ratios observed in permanently anoxic environments  
 980 suggest preferential regeneration of P relative to C under these conditions (Algeo and Ingall, 2007; Anderson  
 981 et al., 2001; Colman et al., 2000; Filippelli, 2001; Ingall and Jahnke, 1997). In the CANOPS-GRB model, P  
 982 benthic regeneration rate is calculated at each sediment segment based on the POP depositional flux density  
 983  $j_{\text{P}}^{\text{dep}} (=j_{\text{org}}^{\text{dep}}/\alpha)$  and P burial efficiency which is a function of both  $[O_2]_{\text{bw}}$  and  $SR$ . We assume the following  
 984 formulation for the  $C_{\text{org}}/P_{\text{org}}$  ratio of the buried organic phase, on the basis of previous studies (Slomp and Van  
 985 Cappellen, 2007; Van Cappellen and Ingall, 1994, 1996):

$$(C_{\text{org}}/P_{\text{org}})_{\text{b}} = \begin{cases} \frac{(C_{\text{org}}/P_{\text{org}})_{\text{b}}^{\text{oxic}} (C_{\text{org}}/P_{\text{org}})_{\text{b}}^{\text{anox}}}{(C_{\text{org}}/P_{\text{org}})_{\text{b}}^{\text{anox}} \frac{[O_2]_{\text{bw}}}{\text{oxic}} + \left(1 - \frac{[O_2]_{\text{bw}}}{\text{oxic}}\right) (C_{\text{org}}/P_{\text{org}})_{\text{b}}^{\text{oxic}}} f_{\tau} & \text{for } [O_2]_{\text{bw}} < \text{oxic} \\ (C_{\text{org}}/P_{\text{org}})_{\text{b}}^{\text{oxic}} f_{\tau} & \text{for } [O_2]_{\text{bw}} \geq \text{oxic} \end{cases}, \quad (49)$$

986 where  $(C_{\text{org}}/P_{\text{org}})_{\text{b}}^{\text{oxic}}$  and  $(C_{\text{org}}/P_{\text{org}})_{\text{b}}^{\text{anox}}$  denote organic C/P ratios for fully oxic and anoxic conditions, and  
 987  $\text{oxic} (=250 \mu\text{M})$  is a threshold value of  $[O_2]_{\text{bw}}$  below which preferential P regeneration occurs.  $(C_{\text{org}}/P_{\text{org}})_{\text{b}}^{\text{oxic}}$   
 988 is set to twice the value of the Redfield ratio, and  $(C_{\text{org}}/P_{\text{org}})_{\text{b}}^{\text{anox}}$  is an upper limit assumed for organic matter  
 989 buried under fully anoxic overlying waters, estimated as 40 times larger than the Redfield value on the basis  
 990 of previous studies on various ancient anoxic basin sediments (Ingall et al., 1993; Slomp and Van Cappellen,  
 991 2007). In Eq. (49), we also include the dependence of buried  $C_{\text{org}}/P_{\text{org}}$  ratio on  $SR$ , expressed as  $f_{\tau}$ . Modern  
 992 observations suggest that  $SR$  is a one of the major factors influencing the preservation versus remineralization  
 993 of sedimentary organic C and P. Organic C preservation in marine sediments tends to be enhanced at higher  
 994  $SR$ . In contrast, the  $C_{\text{org}}/P_{\text{org}}$  ratio of sedimentary organic matter shows a non-linear relationship with respect  
 995 to  $SR$  (Ingall and Cappellen, 1990) (Sect. 3.2.3), suggesting more complex behavior of benthic P cycling.  
 996 Specifically, in the pelagic deep ocean, preferential P regeneration is not observed, likely due to the long  
 997 timescale of diagenesis prior to burial (Ingall and Cappellen, 1990). In the CANOPS model,  $f_{\tau}$  is formulated  
 998 as follows:



$$f_{\tau} = 0.5 + 0.5 \exp\left(-\frac{0.001 \text{ cm}}{SR}\right). \quad (50)$$

Specifically, the  $C_{\text{org}}/P_{\text{org}}$  ratio approaches the Redfield value for oxygenated pelagic sediments.

The burial flux density of  $P_{\text{org}}$  can be calculated as the  $C_{\text{org}}$  burial flux density divided by  $(C_{\text{org}}/P_{\text{org}})_b$ :

$$j_{\text{Porg}}^b = \frac{j_{\text{org}}^{\text{b,ocn}}}{(C_{\text{org}}/P_{\text{org}})_b}. \quad (51)$$

The burial efficiency of  $P_{\text{org}}$  can be written as follows:

$$BE_{\text{Porg}} \equiv \frac{j_{\text{Porg}}^b}{j_{\text{P}}^{\text{dep}}} = \frac{j_{\text{Porg}}^b}{j_{\text{org}}^{\text{dep}}/\alpha} = \frac{\alpha BE_{\text{org}}}{j_{\text{org}}^b/j_{\text{Porg}}^b} = \frac{\alpha BE_{\text{org}}}{(C_{\text{org}}/P_{\text{org}})_b}, \quad (52)$$

where  $j_{\text{P}}^{\text{dep}}$  denotes the POP settling flux density to sediments, which is coupled to the C/P stoichiometry of POM ( $= j_{\text{org}}^{\text{dep}}/\alpha$ ).

Under oxic bottom water conditions, remineralized organic P can be trapped efficiently at the sediment-water interface by ferric iron phases. In contrast, under anoxic bottom water conditions, a lack of ferric iron phases allows most mineralized P to diffuse out of the sediment. This redox-dependent P burial is assumed to be linearly proportional to the  $[O_2]_{\text{bw}}$  (Slomp and Van Cappellen, 2007):

$$j_{\text{P-Fe}}^b = \begin{cases} BE_{\text{Porg}}^{\text{oxic}} \left( \frac{[O_2]_{\text{bw}}}{\text{oxic}} \right) j_{\text{Porg}}^{\text{dep}} & \text{for } [O_2]_{\text{bw}} < \text{oxic} \\ BE_{\text{Porg}}^{\text{oxic}} j_{\text{Porg}}^{\text{dep}} & \text{for } [O_2]_{\text{bw}} \geq \text{oxic} \end{cases}, \quad (53)$$

where  $BE_{\text{Porg}}^{\text{oxic}}$  denotes the burial efficiency of  $P_{\text{org}}$  under well-oxygenated bottom water conditions ( $[O_2]_{\text{bw}} > \text{oxic}$ ). We assume that the retention potential of  $P_{\text{Fe}}$  in oxic sediments is comparable to that of  $P_{\text{org}}$  (Ruttenberg, 1993b).

Some authors have also proposed that authigenic P burial, the dominant process for P burial today (Ruttenberg, 1993b), depends on the redox conditions of the bottom water (Slomp et al., 2002; Slomp and Van Cappellen, 2007). In the CANOPS-GRB model, we adopt the following redox dependence used by Slomp and Van Cappellen (2007):



$$j_{P-Ca}^b = \begin{cases} 2BE_{Porg}^{oxic} \left( a_{auth} + (1 - a_{auth}) \frac{[O_2]_{bw}}{oxic} \right) j_{Porg}^{dep} & \text{for } [O_2]_{bw} < oxic \\ 2BE_{Porg}^{oxic} j_{Porg}^{dep} & \text{for } [O_2]_{bw} \geq oxic \end{cases} \quad (54)$$

1018 We assume that  $P_{org}$ ,  $P_{Fe}$  and  $P_{Ca}$  account roughly for 25%, 25%, and 50%, respectively, of the total reactive  
 1019 P buried in oxygenated sediments (Ruttenberg, 1993b). Therefore, the burial efficiency of authigenic P phases  
 1020 is larger than that of  $P_{org}$  and  $P_{Fe}$  by a factor of 2. The redox-dependency of authigenic P burial is controlled  
 1021 by a parameter,  $a_{auth}$ . There is still great uncertainty as to the sensitivity of P retention efficiency of authigenic  
 1022 P phases to changing redox conditions. For instance, recent modeling study suggests that the burial of  
 1023 authigenic P is influenced not only by the redox state of bottom water, but also by the seawater chemistry  
 1024 (especially  $Ca^{2+}$ ) (Zhao et al., 2020). In our reference run, we set  $a_{auth}$  at 1, no redox-dependency for authigenic  
 1025 P burial.

## 1026 Nitrogen cycling

1027 The benthic denitrification rate is estimated with a semi-empirical relationship (Middelburg et al., 1996).  
 1028 Middelburg and colleagues performed a series of experiments ( $n = 2,000$ ) with a 1-D early diagenetic model  
 1029 of C-N-O<sub>2</sub> to parameterize benthic denitrification  $j_{deni}^{sed}$  ( $\mu\text{mol C cm}^{-2} \text{d}^{-1}$ ) as a polynomial function using  
 1030  $j_{org}^{dep}$  ( $\mu\text{mol C cm}^{-2} \text{d}^{-1}$ ),  $z$  (m), and bottom water concentrations of dissolved O<sub>2</sub> and NO<sub>3</sub><sup>-</sup> ( $\mu\text{M}$ ):

$$\log j_{deni}^{sed} = c_0 + c_1 \log j_{org}^{dep} + c_2 \left( \log j_{org}^{dep} \right)^2 + c_3 \log[NO_3^-]_{bw} \log[O_2]_{bw} \\ + c_4 \log[NO_3^-]_{bw} + c_5 \log[O_2]_{bw} + c_6 \log z + c_7 \log j_{org}^{dep} \log[O_2]_{bw} \quad (55)$$

1031 where  $c_0 = -2.2567$ ,  $c_1 = -0.1850$ ,  $c_2 = -0.2210$ ,  $c_3 = -0.3995$ ,  $c_4 = 1.2500$ ,  $c_5 = 0.4721$ ,  $c_6 = -0.0996$ ,  $c_7 = 0.4256$ .  
 1032 This polynomial function was obtained by examining a parameter space spanning  $50 \text{ m} < z < 6,000 \text{ m}$ ,  $10 \mu\text{M}$   
 1033  $< [O_2]_{bw} < 350 \mu\text{M}$ , and  $1 \mu\text{M} < [NO_3^-]_{bw} < 60 \mu\text{M}$ .  $j_{org}^{dep}$  was allowed to vary within 2 orders of magnitude  
 1034 at each water depth (Middelburg et al., 1996). As pointed out by Romaniello and Derry (2010), the predicted  
 1035 contribution of denitrification to total decomposition  $f_{deni}$  ( $= j_{denitr}^{sed} / j_{recy}^{sed}$ ) can sometimes exceed 100% for  
 1036  $[O_2]_{bw} < 10 \mu\text{M}$ . When the fraction of benthic denitrification to total decomposition exceeds 90%, benthic  
 1037 denitrification is limited in order to avoid unphysical values (Ozaki and Tajika, 2013; Romaniello and Derry,  
 1038 2010).

1039



1040 The burial flux density of  $N_{\text{org}}$  is calculated by molar ratio of C to N of buried sediments,  $(C_{\text{org}}/N_{\text{org}})_b$ , and the  
1041 burial flux of  $C_{\text{org}}$ :

$$j_{N_{\text{org}}}^b = \frac{j_{\text{org}}^{\text{b,ocn}}}{(C_{\text{org}}/N_{\text{org}})_b} \quad (56)$$

1042 We assumed an average ratio of 10, which is observed in the Washington and Mexico margin (Hartnett and  
1043 Devol, 2003; Hedges et al., 1999).

#### 1044 Sulfur cycling

1045 The fractions of MSR and methanogenesis to total decomposition of organic matter in marine sediment are  
1046 given by

$$f_{\text{MSR}} = (1 - f_{\text{aerobic}} - f_{\text{denitr}}) \frac{[\text{SO}_4^{2-}]_{\text{bw}}}{[\text{SO}_4^{2-}]_{\text{bw}} + K_{\text{MSR}}}, \quad (57)$$

$$f_{\text{meth}} = 1 - f_{\text{aero}} - f_{\text{deni}} - f_{\text{MSR}}. \quad (58)$$

1047 The production rate of hydrogen sulfide in sediment,  $j_{\text{H}_2\text{S}}^{\text{sed}}$  ( $\text{mol S m}^{-2} \text{yr}^{-1}$ ), is given by

$$j_{\text{H}_2\text{S}}^{\text{sed}} = \frac{1}{2} f_{\text{MSR}} j_{\text{recy}}^{\text{sed}} + j_{\text{AOM}}, \quad (59)$$

1048 where  $j_{\text{AOM}}$  denotes the production rate of sulfide via AOM:

$$j_{\text{AOM}} = \frac{1}{2} f_{\text{meth}} \frac{[\text{SO}_4^{2-}]_{\text{bw}}}{[\text{SO}_4^{2-}]_{\text{bw}} + K_{\text{MSR}}} j_{\text{recy}}^{\text{sed}}. \quad (60)$$

1049 Here we assume that AOM is proportional to the  $\text{CH}_4$  production rate with a sulfate-dependent term.

1050

1051 The rate of pyrite precipitation in sediments would be proportional to the sulfide production rate at the  
1052 sediment-water interface:

$$j_{\text{pyr}}^{\text{b, sed}} = e_{\text{pyr}} j_{\text{H}_2\text{S}}^{\text{sed}}, \quad (61)$$

1053 where the proportional coefficient,  $e_{\text{pyr}}$ , is the pyrite burial efficiency. The rate of MSR is a function of the  
1054 marine redox state,  $[\text{SO}_4^{2-}]$ , and the availability of degradable organic matter. In the well-oxygenated modern  
1055 oceans most sulfide produced in sediments is reoxidized and only a few per cent of total sulfide is buried as



1056 pyrite (Bowles et al., 2014; Canfield, 1991; Jørgensen, 1982; Lin and Morse, 1991; Turchyn and Schrag, 2004).  
 1057 It has been pointed out that efficient oxidation of sulfide is promoted by animal bioturbation (Berner and  
 1058 Westrich, 1985; Canfield and Farquhar, 2009). In contrast, the value of  $e_{\text{pyr}}$  for anoxic sediments is much  
 1059 greater due to the absence of bioturbation and enhanced sulfide production. We assume that  $e_{\text{pyr}}$  asymptotes  
 1060 toward unity with decreasing the bottom water  $[\text{O}_2]$  (Tarhan et al., 2015):

$$e_{\text{pyr}} = e_{\text{pyr}}^{\text{max}} - \left( e_{\text{pyr}}^{\text{max}} - e_{\text{pyr}}^* \right) \tanh[\text{O}_2]_{\text{bw}}, \quad (62)$$

1061 where  $e_{\text{pyr}}^{\text{max}}$  ( $= 1$  in our reference run) denotes the maximum pyrite precipitation efficiency in anoxic  
 1062 sediments. The reference value,  $e_{\text{pyr}}^*$ , was calibrated using a present-day control simulation such that the  
 1063 present-day seawater  $[\text{SO}_4^{2-}]$  is  $\sim 29$  mM. The obtained value of 0.117 is generally consistent with modern  
 1064 observations (Bottrell and Newton, 2006b; Tarhan et al., 2015; Turchyn and Schrag, 2006a) (see Sect. 3).  
 1065 Although our approach does not provide a mechanistic description of the complex process of pyrite  
 1066 precipitation, it is suitable for many purposes.

### 1067 Early diagenetic modeling for quantifying the OPD

1068 A simple 1-D early diagenetic model of C and  $\text{O}_2$  is employed to obtain the parameterization of OPD (Eq.  
 1069 (48)). The 100 cm thick sediment is vertically divided into 50 layers with an uneven grid. The grid size  
 1070 increases from the sediment-water interface ( $\Delta z = 0.25$  mm) to the maximum simulated sediment depth ( $\Delta z =$   
 1071 1.6 cm). The diagenetic model calculates transport and biogeochemical transformation processes at each grid  
 1072 point within these sediment columns as well as the sedimentary burial and recycling fluxes at the model  
 1073 boundaries. The one-dimensional mass conservation equation for POC (wt. %) and dissolved  $\text{O}_2$  is given by

$$\frac{\partial \text{POC}}{\partial t} = D_{\text{bio}} \frac{\partial^2 \text{POC}}{\partial z^2} - SR \frac{\partial \text{POC}}{\partial z} - k \text{POC}, \quad (63)$$

$$\frac{\partial [\text{O}_2]}{\partial t} = D_{\text{O}_2} \frac{\partial^2 [\text{O}_2]}{\partial z^2} - r_{\text{O}_2} k \text{POC} \left( \frac{\rho(1-\phi)}{1.2\phi} \right) \frac{[\text{O}_2]}{[\text{O}_2] + K_{\text{O}_2}}, \quad (64)$$

1074 where  $D_{\text{O}_2}$  is the diffusion coefficient of  $\text{O}_2$ ,  $SR$  is the sedimentation rate, and  $\phi$  is porosity, which is assumed  
 1075 to be constant over the entire sediment column for simplicity. Bioturbation is formulated as a diffusive process  
 1076 with a coefficient  $D_{\text{bio}}$ . The effective diffusion coefficient of  $\text{O}_2$  is then given by



$$D_{O_2} = \frac{D_{O_2}^{T=0} \times (1 + \nu_{O_2} T_{bw})}{\theta^2} + D_{bio}, \quad (65)$$

1077 where  $D_{O_2}^{T=0}$  denotes a tracer diffusion coefficient in seawater of 0°C,  $\nu_{O_2}$  is a coefficient for temperature  
 1078 dependence of molecular diffusion coefficient. The in situ diffusion coefficient is further corrected for  
 1079 tortuosity  $\theta$ , which is related to pore water resistivity and porosity via the following expressions (Berner, 1980;  
 1080 Colman and Holland, 2000; Tromp et al., 1995):

$$\theta^2 = \phi F \quad (66)$$

$$F = \phi^{-m} \quad (67)$$

1081 where  $F$  is the formation factor—defined as the ratio of bulk sediment resistivity to interstitial water  
 1082 resistivity—and  $m$  is an empirical constant, varying with sediment type. We assumed the average value for  
 1083 unconsolidated muds ( $m = 2.7$ ) in this work (Tromp et al., 1995). The particle mixing coefficient for  
 1084 bioturbation  $D_{bio}$  is formulated as a function of both sediment accumulation rate and bottom water  $O_2$   
 1085 concentration (Tromp et al., 1995; Wallmann, 2003b):

$$D_{bio} = 10^{1.63+0.85 \log SR} \frac{[O_2]_{bw}}{[O_2]_{bw} + K_{O_2}}. \quad (68)$$

1086 At the bottom of the sediment column, a no-flux condition was applied. The parameters used in the 1-D early  
 1087 diagenetic model are tabulated in Table 6.

1088

1089 Table 6: Parameters used in the 1-D early diagenetic model.

Parameters	Label	Value	Unit	Ref.
Porosity	$\phi$	0.8	–	
Dry bulk density	$\rho$	2.6	g cm <sup>-3</sup>	
O <sub>2</sub> :C ratio for aerobic respiration	$r_{O_2}$	1.4	mol mol <sup>-1</sup>	
Half-saturation constant for aerobic respiration	$K_{O_2}$	1	μM	
O <sub>2</sub> diffusion coefficient at 0°C	$D_{O_2}^{T=0}$	281	cm <sup>2</sup> yr <sup>-1</sup>	
Coefficient for a temperature dependence of molecular diffusion coefficient	$\nu_{O_2}$	0.06	°C <sup>-1</sup>	
Exponent for the formation factor	$m$	2.7	–	



1090

## 1091 2.4.5 Air-sea exchange

1092 To calculate the gas exchange of O<sub>2</sub>, H<sub>2</sub>S, NH<sub>3</sub>, and CH<sub>4</sub> across the air–sea interface, we employed a stagnant  
1093 film model (Liss and Slater, 1974). The flux of a gas X across the air–sea interface is controlled by the  
1094 difference in partial pressure between the atmosphere and surface waters, which can be described by the  
1095 following formula:

$$J_X^{\text{air-sea}} = v_X^{\text{pis}} ([X]_{\text{aq}} - [X]_{\text{sat}}), \quad (69)$$

1096 where  $v_X^{\text{pis}}$ ,  $[X]_{\text{aq}}$ , and  $[X]_{\text{sat}}$  denote piston velocity, the dissolved concentration of species X, and the saturation  
1097 concentration of species X, respectively. For O<sub>2</sub>, the saturation concentration is calculated based on solubility  
1098 (Garcia and Gordon, 1992; Sarmiento and Gruber, 2006) and partial pressure:

$$[\text{O}_2]_{\text{sat}} = \left( \frac{1000}{22.3916} e^l \right) \left( \frac{p\text{O}_2}{p\text{O}_2^*} \right), \quad (70)$$

1099 where

$$l = A_0 + A_1 T_s + A_2 T_s^2 + A_3 T_s^3 + A_4 T_s^4 + A_5 T_s^5 + S \times (B_0 + B_1 T_s + B_2 T_s^2 + B_3 T_s^3) + C_0 S^2, \quad (71)$$

$$T_s = \ln \left( \frac{298.15 - T}{273.15 + T} \right), \quad (72)$$

1100 with  $T$  in °C. The constants are  $A_0 = 2.00907$ ,  $A_1 = 3.22014$ ,  $A_2 = 4.0501$ ,  $A_3 = 4.94457$ ,  $A_4 = -0.256847$ ,  $A_5 =$   
1101  $3.88767$ ,  $B_0 = -6.24523 \times 10^{-3}$ ,  $B_1 = -7.3761 \times 10^{-3}$ ,  $B_2 = -1.0341 \times 10^{-2}$ ,  $B_3 = -8.17083 \times 10^{-3}$ , and  $C_0 = -$   
1102  $4.88682 \times 10^{-7}$ . The erroneous  $A_3 \times T_s^2$  term in the original equation (Garcia and Gordon, 1992) was left out  
1103 (Sarmiento and Gruber, 2006).

1104

1105 For CH<sub>4</sub>, H<sub>2</sub>S and NH<sub>3</sub>,  $[X]_{\text{sat}}$  is given by (Kharecha et al., 2005)

$$[X]_{\text{sat}} = K_X^{\text{Henry}} pX, \quad (73)$$

1106 where  $K_X^{\text{Henry}}$ , and  $pX$  denote Henry's law coefficient and the partial pressure of species X, respectively. The  
1107 temperature dependence of X's solubility is expressed as:



$$K_X^{\text{Henry}} = K_X^{\text{Henry}^\circ} \exp \left[ K_X^T \left( \frac{1}{T} - \frac{1}{298.15} \right) \right], \quad (74)$$

1108 where  $K_X^{\text{Henry}^\circ}$  denotes the Henry's law coefficient of species X at 25°C, and  $K_X^T$  is the temperature  
1109 dependence constant.

1110

1111  $[X]_{\text{aq}}$  is the dissolved concentration of X.  $[\text{H}_2\text{S}]_{\text{aq}}$  and  $[\text{NH}_3]_{\text{aq}}$  can be written as follows:

$$[\text{H}_2\text{S}]_{\text{aq}} = \frac{[\Sigma\text{H}_2\text{S}]}{1 + K_{\text{H}_2\text{S}}^{\text{dis}}/[\text{H}^+]} \quad (75)$$

$$[\text{NH}_3]_{\text{aq}} = \frac{[\Sigma\text{NH}_3]}{1 + [\text{H}^+]/K_{\text{NH}_3}^{\text{dis}}} \quad (76)$$

1112 where  $[\Sigma\text{H}_2\text{S}] = [\text{H}_2\text{S}] + [\text{HS}^-]$  and  $[\Sigma\text{NH}_3] = [\text{NH}_4^+] + [\text{NH}_3]$ .  $K_{\text{H}_2\text{S}}^{\text{dis}}$  and  $K_{\text{NH}_3}^{\text{dis}}$  are the dissociation constant,  
1113 defined as follows:

$$K_{\text{H}_2\text{S}}^{\text{dis}} = \frac{[\text{HS}^-][\text{H}^+]}{[\text{H}_2\text{S}]_{\text{aq}}}, \quad (77)$$

$$K_{\text{H}_2\text{S}}^{\text{dis}} = \frac{[\text{NH}_3]_{\text{aq}}[\text{H}^+]}{[\text{NH}_4^+]}. \quad (78)$$

1114 Given values of  $K_{\text{H}_2\text{S}}^{\text{dis}}$ ,  $K_{\text{NH}_3}^{\text{dis}}$  and  $p\text{H}$  (Millero et al., 1988; Yao and Millero, 1995),  $[\text{H}_2\text{S}]_{\text{aq}}$  and  $[\text{NH}_3]_{\text{aq}}$  can  
1115 be calculated.

1116

1117 In the CANOPS-GRB model, atmospheric concentrations of  $\text{H}_2\text{S}$  and  $\text{NH}_3$  are set at 0.  $\text{H}_2\text{S}$  and  $\text{NH}_3$  flow past  
1118 the surface layer of the ocean to the atmosphere are converted to an equal influx of  $\text{SO}_4^{2-}$  and  $\text{NO}_3^-$  to the  
1119 surface ocean. The parameters used in the stagnant film model are tabulated in Table 7.

1120

1121 If atmospheric  $\text{O}_2$  levels are lower than ~1% PAL spatial heterogeneity of the gas exchange flux is expected  
1122 (Olson et al., 2016); for example primary productivity (and  $\text{O}_2$  generation) would be more active in coastal  
1123 regions than open-ocean gyres. Because our ocean model resolves only two regions for the surface oceans  
1124 (low-mid latitude region L and high latitude region H), it tends to overestimate the oxidation of reductants in



1125 surface mixing layers. To mitigate this model limitation for the CH<sub>4</sub> degassing flux, the aerobic oxidation rate  
 1126 of CH<sub>4</sub> is decreased to  $1 \times 10^{-7}$  of the standard value in surface layers (Ozaki et al., 2019a).

1127

1128 Table 7: Parameters used in the air-sea exchange module of CANOPS-GRB.

Parameters	Label	Value	Unit	Ref.
Piston velocity of O <sub>2</sub>	$v_{O_2}^{pis}$	1,000	m yr <sup>-1</sup>	This study
Piston velocity of NH <sub>3</sub>	$v_{NH_3}^{pis}$	300	m yr <sup>-1</sup>	(WebBook, 2022)
Piston velocity of H <sub>2</sub> S	$v_{H_2S}^{pis}$	1072	m yr <sup>-1</sup>	(WebBook, 2022)
Piston velocity of CH <sub>4</sub>	$v_{CH_4}^{pis}$	1419	m yr <sup>-1</sup>	(WebBook, 2022)
Solubility of NH <sub>3</sub> at 25°C	$K_{NH_3}^{Henry^\circ}$	$5.6 \times 10^4$	mol m <sup>-3</sup> bar <sup>-1</sup>	
Solubility of H <sub>2</sub> S at 25°C	$K_{H_2S}^{Henry^\circ}$	100	mol m <sup>-3</sup> bar <sup>-1</sup>	
Solubility of CH <sub>4</sub> at 25°C	$K_{CH_4}^{Henry^\circ}$	1.4	mol m <sup>-3</sup> bar <sup>-1</sup>	
Temperature dependence of solubility of NH <sub>3</sub>	$K_{NH_3}^T$	4,100	K	
Temperature dependence of solubility of H <sub>2</sub> S	$K_{H_2S}^T$	2,100	K	
Temperature dependence of solubility of CH <sub>4</sub>	$K_{CH_4}^T$	1,600	K	
Sea surface pH at low-mid latitude region	$pH^l$	8.17	–	This study
Sea surface pH at high latitude region	$pH^h$	8.16	–	This study
Partial pressure of atmospheric NH <sub>3</sub>	$p_{NH_3}$	0	atm	This study
Partial pressure of atmospheric H <sub>2</sub> S	$p_{H_2S}$	0	atm	This study

1129

## 1130 2.5 Land model

### 1131 2.5.1 Net primary productivity

1132 Terrestrial NPP is scaled by global land biomass  $V$  normalized to the modern value:

$$J_{NPP}^{Ind} = V \times J_{NPP}^{Ind,*}, \quad (79)$$



1133 where the present value of terrestrial NPP is set at  $60 \text{ Gt C yr}^{-1}$  (Prentice et al., 2001). The global land biomass  
1134 is a function of atmospheric  $\text{O}_2$  levels:

$$V = f_{\text{UV}} f_{\text{fire}} f_{\text{O}_2}, \quad (80)$$

1135 where  $f_{\text{O}_2}$  represents the direct effect of atmospheric  $\text{O}_2$  concentration on the  $\text{C}_3$  plant growth, and  $f_{\text{fire}}$  denotes  
1136 the effect of fires on land biota (Bergman et al., 2004; Lenton and Watson, 2000b):

$$f_{\text{O}_2} = \max \{1.5 - 0.5 p\text{O}_2^{\text{PAL}}, 0\}, \quad (81)$$

$$f_{\text{fire}} = \frac{k_{\text{fire}}}{k_{\text{fire}} - 1 + \text{ignit}}. \quad (82)$$

1137 Here  $k_{\text{fire}}$  ( $= 3$ ; Lenton, 2013) is the fire frequency constant, and *ignit* is an ignition factor representing the fire  
1138 frequency as a function of oxygen (Lenton, 2013; Lenton et al., 2018; Lenton and Watson, 2000b):

$$\text{ignit} = \min \{ \max \{ c_1 p\text{O}_2 - c_2, 0 \}, c_3 \}, \quad (83)$$

1139 with  $c_1 = 48$ ,  $c_2 = 9.08$  and  $c_3 = 5$  (Lenton, 2013). CANOPS-GRB also includes an additional factor  $f_{\text{UV}}$   
1140 representing the effect of UV on the terrestrial biosphere as a function of atmospheric  $\text{O}_2$  levels (Ozaki and  
1141 Reinhard, 2021):

$$f_{\text{UV}} = \tanh \left( \frac{p\text{O}_2^{\text{PAL}}}{c_{\text{UV}}} \right), \quad (84)$$

1142 where  $c_{\text{UV}}$  is a model parameter, which, in our standard model is set at 1% PAL, meaning that terrestrial plant  
1143 activity is suppressed when atmospheric  $\text{O}_2$  is lower than a few % PAL.

## 1144 2.5.2 Terrestrial biogeochemical cycles

1145 Phosphorus weathering flux,  $J_{\text{P}}^{\text{w}}$  (Eq. (2)), is treated as a boundary condition. A fraction of weathered P is  
1146 ultimately buried as terrigenous organic matter (Eq. (3)), whereas the remaining fraction is delivered to the  
1147 ocean via rivers (Eq. (4)). In the CANOPS-GRB model, the reference value of  $J_{\text{P}}^{\text{r}}$  ( $= 0.155 \text{ Tmol P yr}^{-1}$ ) is  
1148 tuned so that the oceanic P level of the reference state is consistent with modern observations. The burial rate  
1149 of terrigenous organic matter (in terms of C) can be written as follows:



$$J_{\text{org}}^{\text{b,ld}} = \left( C_{\text{org}}/P_{\text{org}} \right)^{\text{ld}} J_{\text{p}}^{\text{b,ld}}, \quad (85)$$

1150 where  $(C_{\text{org}}/P_{\text{org}})^{\text{ld}}$  (= 1000) is the average C/P burial ratio of terrigenous organic matter (Bergman et al.,  
 1151 2004). In this study, the reference value of  $J_{\text{org}}^{\text{b,ld}}$  was set at 3 Tmol C yr<sup>-1</sup>. By combining Eqs. (3), (4), and  
 1152 (85) for the reference state, the proportional coefficient  $k_{11}$  of Eq. (3) is determined by the reference state, as  
 1153 follows:

$$k_{11} = \frac{J_{\text{org}}^{\text{b,ld,*}}}{J_{\text{org}}^{\text{b,ld,*}} + \left( C_{\text{org}}/P_{\text{org}} \right)^{\text{ld}} J_{\text{p}}^{\text{r,*}}} = 0.0189. \quad (86)$$

1154 The value of  $k_{11}$  is treated as a constant in this study.

1155

1156 Almost all organic matter produced by terrestrial NPP is decomposed before burial. The total decomposition  
 1157 rate is given by:

$$J_{\text{org}}^{\text{r,ld}} = J_{\text{NPP}}^{\text{ld}} - J_{\text{org}}^{\text{b,ld}}. \quad (87)$$

1158 CANOPS-GRB includes aerobic respiration and methanogenesis as respiration pathways for terrigenous matter,  
 1159 and the CH<sub>4</sub> flux from the terrestrial ecosystem to the atmosphere is evaluated with the assumption that it is  
 1160 proportional to the burial rate of terrigenous organic matter:

$$J_{\text{CH}_4}^{\text{ld}} = \left( \frac{J_{\text{org}}^{\text{b,ld}}}{J_{\text{org}}^{\text{b,ld,*}}} \right) J_{\text{CH}_4}^{\text{ld,*}}, \quad (88)$$

1161 where the reference value was set at 1 Tmol CH<sub>4</sub> yr<sup>-1</sup>. The net flux of CO<sub>2</sub>, O<sub>2</sub> and CH<sub>4</sub> from the terrestrial  
 1162 ecosystem to the atmosphere can be written, as follows:

$$J_{\text{CO}_2}^{\text{ld}} = \left( g_{\text{O}_2} + \frac{1}{2}(1+\delta)g_{\text{CH}_4} \right) J_{\text{org}}^{\text{r,ld}}, \quad (89)$$

$$J_{\text{O}_2}^{\text{ld}} = J_{\text{NPP}}^{\text{ld}} - \left( g_{\text{O}_2} + \delta g_{\text{CH}_4} \right) J_{\text{org}}^{\text{r,ld}}, \quad (90)$$

$$J_{\text{CH}_4}^{\text{ld}} = \frac{1}{2}(1-\delta)g_{\text{CH}_4} J_{\text{org}}^{\text{r,ld}}, \quad (91)$$



1163 where  $g_{O_2}$  and  $g_{CH_4}$  denote the fraction of organic matter decomposed by aerobic respiration and  
 1164 methanogenesis, respectively.  $\delta$  represents the fraction of methane that is consumed by aerobic methanotrophy  
 1165 that is a function of  $O_2$ :

$$\delta = \frac{M_{O_2}^{atm}}{M_{O_2}^{atm} + K'_{O_2}}, \quad (92)$$

1166 with  $K'_{O_2} = 0.273 \times 10^{18}$  mol (Goldblatt et al., 2006). A fraction of organic matter decomposed by  
 1167 methanogenesis,  $g_{CH_4}$ , can be calculated based on Eqs. (89) and (91). Then,  $g_{O_2}$  is determined from  $1 - g_{CH_4}$ .

### 1168 2.5.3 Weathering

1169 The oxidative weathering of continental crust is a major oxygen sink on geologic timescales, providing a  
 1170 fundamental control on atmospheric  $O_2$  levels. The weathering rate in the model is assumed to be proportional  
 1171 to sedimentary reservoir size and a global erosion factor,  $f_R$ , expressing the effect of continental  
 1172 denudation/erosion on terrestrial weathering:

$$J_{org}^w = f_R f_{orgw}^{O_2} \left( \frac{ORG}{ORG^*} \right) J_{org}^{w,*}, \quad (93)$$

$$J_{pyr}^w = f_R f_{pyrw}^{O_2} \left( \frac{PYR}{PYR^*} \right) J_{pyr}^{w,*}, \quad (94)$$

1173 where  $J_{org}^w$  and  $J_{pyr}^w$  denotes the oxidative weathering of organic carbon and pyrite, respectively, and  $f_{orgw}^{O_2}$   
 1174 and  $f_{pyrw}^{O_2}$  represent the  $O_2$  dependency. For the oxidative weathering of organic matter, previous  
 1175 biogeochemical models have adapted a  $(pO_2^{PAL})^{0.5}$  relationship (Bergman et al., 2004; Lasaga and Ohmoto,  
 1176 2002). In this study, we employ alternative empirical relationships based on results obtained from a 1-D  
 1177 weathering model (Bolton et al., 2006; Daines et al., 2017):

$$f_{orgw}^{O_2} = c_{orgw} \frac{pO_2^{PAL}}{pO_2^{PAL} + K_{orgw}}, \quad (95)$$

$$f_{pyrw}^{O_2} = c_{pyrw} \frac{pO_2^{PAL}}{pO_2^{PAL} + K_{pyrw}}, \quad (96)$$

1178 where  $K_{orgw}$  and  $K_{pyrw}$  denote half-saturation constants ( $K_{orgw} = 0.334$  and  $K_{pyrw} = 0.017$ ) and  $c_{orgw}$  and  $c_{pyrw}$   
 1179 are normalized constants ( $c_{orgw} = 1.334$  and  $c_{pyrw} = 1.017$ ), respectively. The Monod-type relationship captures

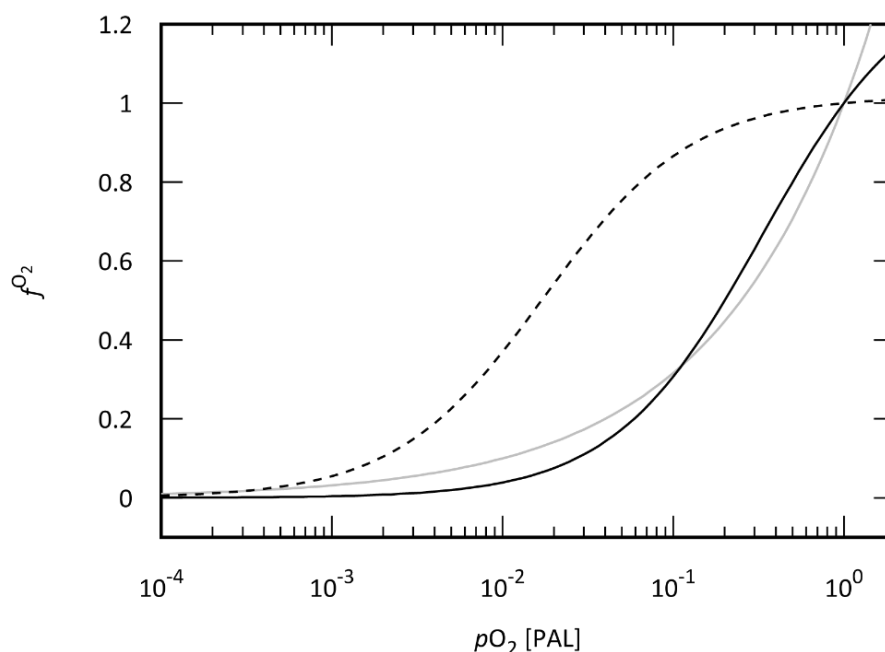


1180 the fact that the rate of oxidative weathering reaches its maximum as determined by the erosion rate under  
1181 highly oxygenated conditions (i.e., transport-limited regime). For example, due to the fast dissolution kinetics  
1182 of pyrite, oxidative weathering can be regarded as transport-limited under modern conditions (Bolton et al.,  
1183 2006) (Fig. 10). In the CANOPS-GRB model,  $J_{\text{org}}^{\text{w}*}$  is calibrated based on the global redox budget of the  
1184 reference run (see Sect. 2.2.5).

1185

1186 It is important to note that above equations ignore the possible importance of microbial activity and  
1187 temperature on the rate of oxidative weathering (Petsch et al., 2001; Soulet et al., 2021). Both represent  
1188 important topics for future research.

1189



1190

1191 **Figure 10**  $\text{O}_2$  dependency of the oxidative weathering rate of organic matter and pyrite sulfur. Gray line  
1192 denotes the  $(p\text{O}_2^{\text{PAL}})^{0.5}$  relationship assumed in previous biogeochemical models (Daines et al., 2017; Lasaga  
1193 and Ohmoto, 2002). Solid and dashed black lines represent the empirical Monod-type relationships for  
1194 oxidative weathering of organic matter and pyrite sulfur based on the results obtained from a 1-D weathering  
1195 model (Bolton et al., 2006; Daines et al., 2017), which are adopted in the standard model of the CANOPS-  
1196 GRB model. PAL = present atmospheric level.

1197



1198 The present riverine flux of sulfur,  $J_S^{r*}$ , is estimated at 2.6 Tmol S yr<sup>-1</sup> (Raiswell and Canfield, 2012),  
1199 representing the dominant source to the oceans. Riverine flux is written as the sum of the gypsum weathering  
1200 flux  $J_{\text{gyp}}^w$  and the oxidative weathering of pyrite  $J_{\text{pyr}}^w$  and depends directly or indirectly on the oxidation state  
1201 of the atmosphere:

$$J_S^r = J_{\text{gyp}}^w + J_{\text{pyr}}^w. \quad (97)$$

1202 Based on previous studies (Bergman et al., 2004; Berner, 2009; Markovic et al., 2015; Wortmann and Paytan,  
1203 2012), a 3:1 ratio in modern rivers of SO<sub>4</sub><sup>2-</sup> from gypsum versus pyrite weathering is assumed. Gypsum  
1204 weathering flux is assumed to be proportional to its sedimentary reservoir size,  $GYP$ , and  $f_R$ :

$$J_{\text{gyp}}^w = f_R \left( \frac{GYP}{GYP^*} \right) J_{\text{gyp}}^{w*}, \quad (98)$$

1205 where \* represents the present value.

1206

1207 In the previous version of the CANOPS (Ozaki et al., 2019a), oxidative weathering of pyrite was divided to  
1208 biogenic and abiotic weathering fluxes. In this study, we simplify this (Eq. (94)). Also, oxidative weathering  
1209 of Fe(II)-bearing minerals is ignored in this study, which simplifies the framework of the global O<sub>2</sub> budget  
1210 (Sect. 2.2.5).

#### 1211 2.5.4 Volcanic degassing

1212 Volcanic outgassing fluxes of carbon and sulfur are assumed to be proportional to their respective crustal  
1213 reservoir sizes:

$$J_{\text{org}}^m = \left( \frac{ORG}{ORG^*} \right) J_{\text{org}}^{m*}, \quad (99)$$

$$J_{\text{pyr}}^m = \left( \frac{PYR}{PYR^*} \right) J_{\text{pyr}}^{m*}, \quad (100)$$

$$J_{\text{gyp}}^m = \left( \frac{GYP}{GYP^*} \right) J_{\text{gyp}}^{m*}. \quad (101)$$

1214 We set the reference value of the volcanic outgassing flux of organic carbon,  $J_{\text{org}}^{m*}$ , at 1.25 Tmol C yr<sup>-1</sup>  
1215 (Bergman et al., 2004). The estimates of modern volcanic fluxes of sulfur fall within the range of ~0.3–3 Tmol



1216  $\text{S yr}^{-1}$  (Catling and Kasting, 2017; Kagoshima et al., 2015; Raiswell and Canfield, 2012; Walker and  
1217 Brimblecombe, 1985). We adopted a recent estimate of  $0.8 \text{ Tmol S yr}^{-1}$  (Kagoshima et al., 2015).

## 1218 2.5.5 Sedimentary reservoirs

1219 We extend the original model framework to the explicit calculation of the secular evolution of the sedimentary  
1220 reservoirs, linking the biogeochemical cycles in the ocean-atmosphere system to the rock cycle. The mass  
1221 balance equation for sedimentary organic carbon (*ORG*) can be written as follows:

$$\frac{dORG}{dt} = J_{\text{org}}^{\text{b}} - J_{\text{org}}^{\text{w}} - J_{\text{org}}^{\text{m}}, \quad (102)$$

1222 where  $J_{\text{org}}^{\text{b}}$  denotes the sum of the burial rate of marine and terrigenous organic matter ( $J_{\text{org}}^{\text{b,ocn}} + J_{\text{org}}^{\text{b,lnd}}$ ), the  
1223 primary source of sedimentary organic carbon. Primary outputs are oxidative weathering, volcanic outgassing  
1224 and metamorphism. Previous estimates of the present reservoir size of *ORG* fall in the range of 1000–1300  
1225 Emol ( $1 \text{ E} = 10^{18}$ ) (Berner, 1989; Garrels and Perry, 1974; Mackenzie et al., 1993). We assumed 1250 Emol  
1226 for the reference value of *ORG*.

1227

1228 The sedimentary reservoir sizes of pyrite sulfur (*PYR*) and gypsum sulfur (*GYP*) are also written as the balance  
1229 between the input (burial) and outputs (weathering and outgassing):

$$\frac{dPYR}{dt} = J_{\text{pyr}}^{\text{b}} - J_{\text{pyr}}^{\text{w}} - J_{\text{pyr}}^{\text{m}}, \quad (103)$$

$$\frac{dGYP}{dt} = J_{\text{gyp}}^{\text{b}} - J_{\text{gyp}}^{\text{w}} - J_{\text{gyp}}^{\text{m}}, \quad (104)$$

1230 where  $J_{\text{pyr}}^{\text{b}}$  represents the sum of pyrite precipitation rates in the water column and sediments,  $J_{\text{pyr}}^{\text{b,wc}} + J_{\text{pyr}}^{\text{b,sed}}$ .  
1231 Previous estimates of present reservoir sizes of *GYP* and *PYR* fall in the range of 77–300 Emol and 155–300  
1232 Emol (Berner, 2006; Bottrell and Newton, 2006a; Holser et al., 1989; Kump, 1989; Lasaga, 1989; Schlesinger  
1233 and Bernhardt, 2013; Sleep, 2005; Yaroshevsky, 2006), respectively. We adopted 200 Emol and 200 Emol for  
1234 *GYP\** and *PYR\**.



## 1235 2.6 Atmosphere model

### 1236 2.6.1 Hydrogen escape

1237 The rate of hydrogen escape is assumed to be diffusion-limited as it is today. Thus, the total concentration of  
1238 all H-bearing compounds in the lower stratosphere determines the rate of hydrogen escape (Walker, 1977).  
1239 For Proterozoic-Phanerozoic atmospheres, CH<sub>4</sub> appears to have been the dominant hydrogen-bearing species  
1240 in the stratosphere, and the flux,  $J_{\text{Hesc}}$  (mol yr<sup>-1</sup>), is calculated as

$$J_{\text{Hesc}} = sM_{\text{CH}_4}^{\text{atm}}, \quad (105)$$

1241 where  $M_{\text{CH}_4}^{\text{atm}}$  denotes the abundance of CH<sub>4</sub> in the atmosphere (mol) and  $s$  ( $= 3.7 \times 10^{-5}$  yr<sup>-1</sup>) is a proportional  
1242 coefficient (Goldblatt et al., 2006).

### 1243 2.6.2 Photochemistry

1244 CANOPS-GRB includes parameterized O<sub>2</sub>-O<sub>3</sub>-CH<sub>4</sub> photochemistry that allows quantification of the  
1245 abundances of atmospheric O<sub>2</sub> and CH<sub>4</sub>. The rate of oxidation of CH<sub>4</sub> is calculated by the following empirical  
1246 parameterization that was obtained from a 1-D photochemistry model (Claire et al., 2006):

$$J_{\text{CH}_4\text{ox}} = k_{\text{CH}_4\text{ox}} M_{\text{O}_2}^{\text{atm}} M_{\text{CH}_4}^{\text{atm}}, \quad (106)$$

1247 where  $M_{\text{O}_2}^{\text{atm}}$  and  $M_{\text{CH}_4}^{\text{atm}}$  denote the abundance of O<sub>2</sub> and CH<sub>4</sub> in the atmosphere (mol). The reaction rate  
1248  $k_{\text{CH}_4\text{ox}}$  (mol<sup>-1</sup> yr<sup>-1</sup>) is expressed as a polynomial function of the reservoir sizes of O<sub>2</sub> and CH<sub>4</sub> (Ozaki and  
1249 Reinhard, 2021):

$$\log k_{\text{CH}_4\text{ox}} = \alpha_0^j + \alpha_1^j \cdot \varphi_{\text{O}_2} + \alpha_2^j \cdot \varphi_{\text{O}_2}^2 + \alpha_3^j \cdot \varphi_{\text{O}_2}^3 + \alpha_4^j \cdot \varphi_{\text{O}_2}^4 + \alpha_5^j \cdot \varphi_{\text{O}_2}^5 + \alpha_6^j \cdot \varphi_{\text{O}_2}^6, \quad (107)$$

1250 where  $\alpha_i^j$  are fitting coefficients for given atmospheric CH<sub>4</sub> levels and  $\varphi_{\text{O}_2}$  is  $\log p\text{O}_2$  (in bar) (Supplementary  
1251 Table 4 of Ozaki and Reinhard, 2021). The oxidation rate was evaluated using Fig. 3 of Claire et al. (2006),  
1252 showing the oxidation rate as a function of  $p\text{O}_2$  and  $p\text{CH}_4$ . We took the relationship between  $k_{\text{CH}_4\text{ox}}$  and  $p\text{O}_2$   
1253 for  $p\text{CH}_4$  of  $10^{-6}$ ,  $10^{-5}$ ,  $10^{-4}$ ,  $10^{-3}$ ,  $2 \times 10^{-3}$  bar, and  $k_{\text{CH}_4\text{ox}}$  is calculated as a function of  $p\text{O}_2$  and  $p\text{CH}_4$  with a log-  
1254 linear interpolation method.



### 1255 2.6.3 Mass balance

1256 CANOPS-GRB accounts for the atmospheric concentrations of O<sub>2</sub> and CH<sub>4</sub>. The atmospheric concentration  
1257 of O<sub>2</sub> is determined by the biogenic source (from the ocean and terrestrial ecosystems) and the consumption  
1258 through the series of oxidation reaction (the continental weathering of kerogen and pyrite, volcanic outgassing,  
1259 and photochemical oxidation of methane):

$$\frac{dM_{\text{O}_2}^{\text{atm}}}{dt} = J_{\text{O}_2\uparrow}^{\text{air-sea}} + J_{\text{O}_2\uparrow}^{\text{air-land}} - \left( J_{\text{Hesc}} + 2J_{\text{CH}_4\text{ox}} \right) - \left( J_{\text{org}}^{\text{w}} + J_{\text{org}}^{\text{m}} \right) - 2 \left( J_{\text{pyr}}^{\text{w}} + J_{\text{pyr}}^{\text{m}} \right), \quad (108)$$

1260 where  $M_{\text{O}_2}^{\text{atm}}$  denotes the mass of O<sub>2</sub> in the atmosphere (moles), and the first and second term on the right  
1261 hand side represents the biogenic flux of O<sub>2</sub> from marine and terrestrial ecosystems. The third term denotes  
1262 O<sub>2</sub> consumption via photochemistry, and the fourth and fifth terms are the O<sub>2</sub> consumption via organic C and  
1263 pyrite S sub-cycles.

1264

1265 The abundance of CH<sub>4</sub> in the atmosphere,  $M_{\text{CH}_4}^{\text{atm}}$ , is determined by input from the ecosystems and the  
1266 consumption of CH<sub>4</sub> via photolysis, as well as by the hydrogen escape:

$$\frac{dM_{\text{CH}_4}^{\text{atm}}}{dt} = J_{\text{CH}_4\uparrow}^{\text{air-sea}} + J_{\text{CH}_4\uparrow}^{\text{air-land}} - \left( J_{\text{Hesc}} + J_{\text{CH}_4\text{ox}} \right). \quad (109)$$

1267 No abiotic CH<sub>4</sub> input via hydrothermal systems is included.



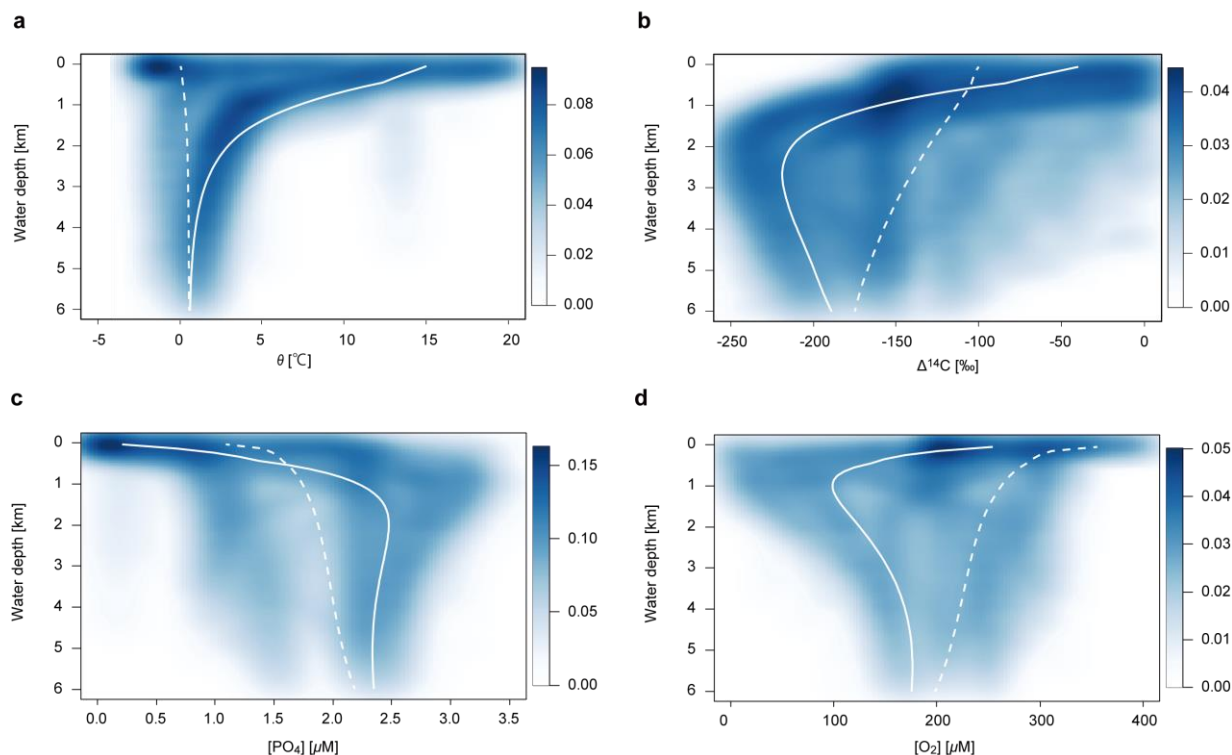
### 1268 **3 Validation against the modern global ocean**

1269 Here, a steady-state simulation mimicking the present-day condition was run to evaluate the overall  
1270 performance of CANOPS-GRB. To do this, the ocean model was run until reaching the steady state, assuming  
1271 the present atmospheric O<sub>2</sub> level and reference values of boundary fluxes (weathering and volcanic fluxes).  
1272 The simulated circulation and biogeochemistry for the modern global ocean was compared with modern  
1273 oceanographic observations from the Global Ocean Data Analysis Project (Key et al., 2015; Olsen et al., 2016).

#### 1274 **3.1 Distribution of circulation tracers**

1275 Comparisons of model output with circulation tracers, such as potential temperature ( $\theta$ ) and radiocarbon  
1276 ( $\Delta^{14}\text{C}$ ), permit a test of the physical exchange scheme. Figure 11 depicts the simulated patterns of physical  
1277 tracers with observational data. The physical circulation in the model generally agrees well with oceanic  
1278 observations, although we note that model temperatures for low-mid latitudes above 1,000 m water depth tend  
1279 to be higher than observed because temperature distribution in the real ocean is strongly controlled by vertical  
1280 structure and advective processes that are not captured in our simple circulation scheme. Despite this model  
1281 limitation, the modelled temperature distribution generally reproduces the observed distribution. The  $\Delta^{14}\text{C}$   
1282 minimum in the model for the low-mid latitude region corresponds well with observations. The modelled  
1283 background radiocarbon for young deep waters (about  $-150\pm 25\%$ ) is closer to the value for the Southern  
1284 Ocean (approximately  $-150\%$ ) than for North Atlantic deep waters (approximately  $-80\%$ ), and old deep  
1285 waters ( $-200\pm 15\%$ ) correspond to the South Pacific. We conclude that the simulated circulation tracers  
1286 generally match well with ocean data.

1287



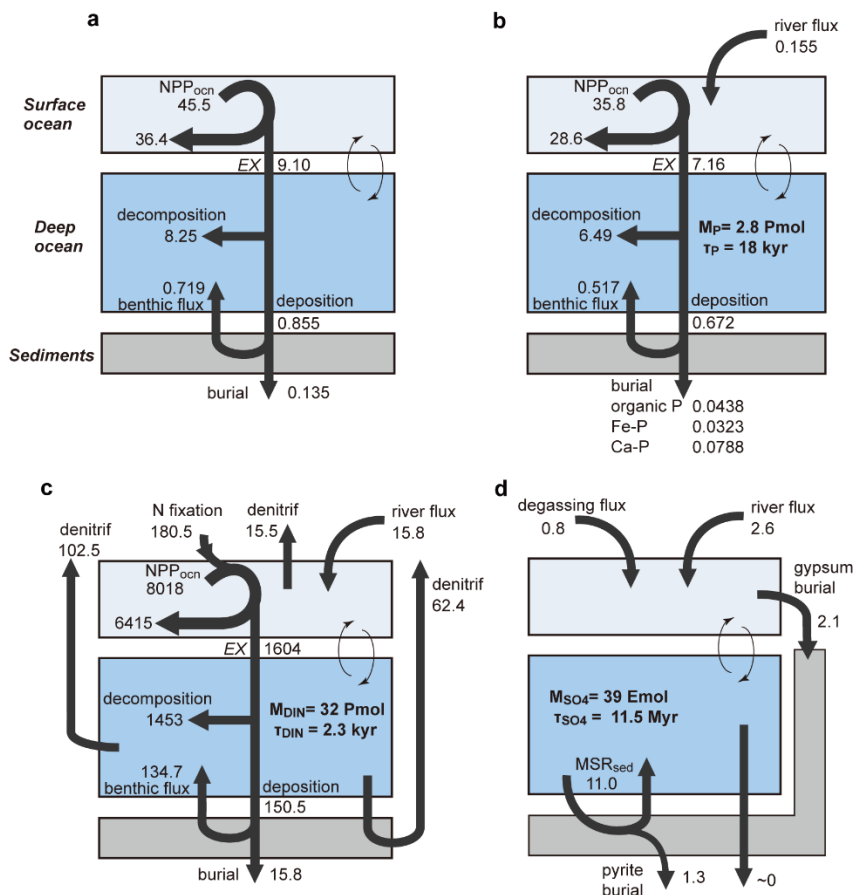
1288

1289 **Figure 11** Simulated steady state depth-profiles of (a) potential temperature,  $\theta$ , (b) radio carbon,  $\Delta^{14}\text{C}$ , (c)  
1290 DIP (dissolved inorganic phosphorus,  $\text{PO}_4^{3-}$ ), and (d) dissolved oxygen,  $\text{O}_2$ . Solid and dashed white lines  
1291 denote the simulated profiles for LD and HD region, respectively. Simulation results are compared with the  
1292 dataset from the Global Ocean Data Analysis Project (GLODAP) data base (GLODAPv2\_2019; Key et al.,  
1293 2015; Olsen et al., 2016). The color represents the density of observational points.

### 1294 3.2 Ocean biogeochemistry

1295 Having demonstrated that CANOPS-GRB's ocean circulation model does a reasonable job of representing  
1296 water mass exchange, we next assess the performance of the oceanic biogeochemistry model by comparing  
1297 its output to ocean biogeochemical data. Model-generated global fluxes and inventories of C, P, N and S cycles  
1298 are summarized in Fig. 12. Those compare well with independent observational estimates. Below, we provide  
1299 a brief discussion of globally-integrated biogeochemical flux estimates.

1300



1301

1302 **Figure 12** Schematics of the simulated material flow in the ocean for the reference run. **(a)** Organic carbon  
 1303 (in Gt C yr<sup>-1</sup>), **(b)** phosphorus (in Tmol P yr<sup>-1</sup>), **(c)** nitrogen (in Tg N yr<sup>-1</sup>), and **(d)** sulfur (in Tmol S yr<sup>-1</sup>).  
 1304  $NPP_{ocn}$  = oceanic net primary production.  $EX$  = export production.  $M_X$  = mass of X in the ocean.  $\tau_X$  = residence  
 1305 time of X in the ocean. Pmol = 10<sup>15</sup> mol.

### 1306 3.2.1 Distribution of nutrients and oxygen

1307 The simulated vertical profile of phosphate captures the characteristic features and values of observational  
 1308 data (Fig. 11c). More specifically, the distribution in the low-mid latitude region is more similar to that in the  
 1309 Pacific and Indian Ocean, and distribution of high-mid latitude region is similar to that in the Southern Ocean.  
 1310 This is a consequence of limiting high-latitude productivity (preformed DIP is 1.1  $\mu\text{M}$ ) which results in higher  
 1311 concentrations in the ocean interior. The model dissolved O<sub>2</sub> profile for low-mid latitude shows a minimum  
 1312 of approximately 100  $\mu\text{M}$  at water depth of 1,000 m, corresponding to the oxygen minimum zone (Fig. 11d).

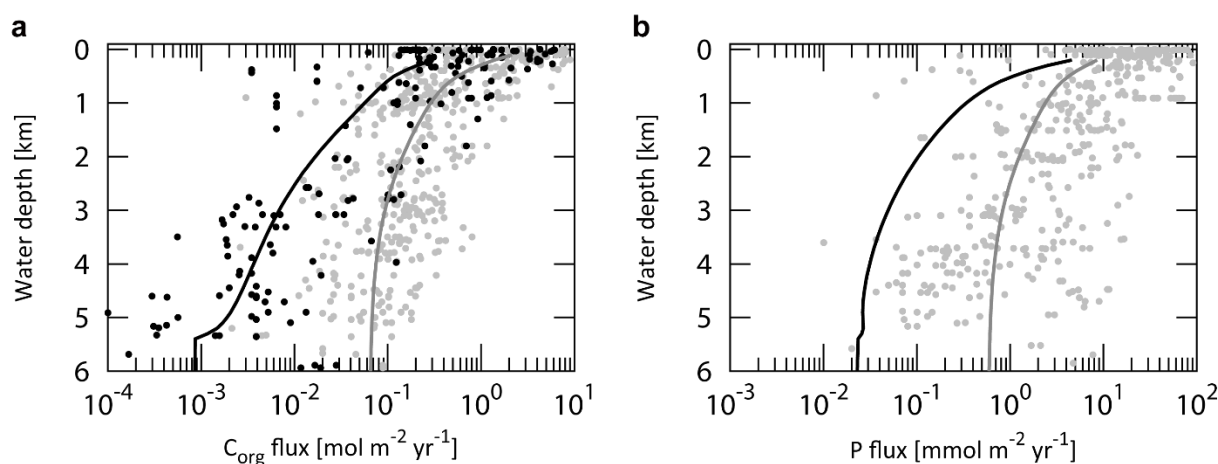


1313 In contrast, dissolved O<sub>2</sub> for high-mid latitude sector (HD) shows a monotonically decreasing trend. This is  
1314 because of oxygen consumption via POM decomposition during downwelling.

### 1315 3.2.2 Carbon cycling

1316 The marine export/new production in our model is 9.1 Gt C yr<sup>-1</sup> (8.36 Gt C yr<sup>-1</sup> at L and 0.74 Gt C yr<sup>-1</sup> at H).  
1317 This is consistent with previously estimated global values of 8.5–12 Gt C yr<sup>-1</sup> (Dunne et al., 2007a; Heinze et  
1318 al., 2009; Laws et al., 2000; Sarmiento and Gruber, 2006). In particular, our estimate is close to the mid-point  
1319 of the previously estimated range of 9.6±3.6 Gt C yr<sup>-1</sup> (Dunne et al., 2007b). This is a marked improvement  
1320 from earlier studies with box models which have underestimated marine new production by a factor of 2 or  
1321 more (Archer et al., 2000; Shaffer et al., 2008). Simulated global oceanic NPP is 45.5 Gt C yr<sup>-1</sup>. This is also  
1322 consistent with the previous estimated range of 44–65 Gt C yr<sup>-1</sup> (Berelson et al., 2007; Carr et al., 2006;  
1323 Prentice et al., 2001; Woodward, 2007).

1324



1325

1326 **Figure 13** Simulated steady-state depth-profiles of organic C and reactive P flux density for the LD region. In  
1327 (a), gray dots denote observations of depositional/settling flux density, whereas black dots represent  
1328 observations of burial flux density compiled from literature survey (Baturin, 2007; Betts and Holland, 1991;  
1329 Colman et al., 2000; Lutz et al., 2002). Gray and black solid lines denote the simulated POC depositional and  
1330 burial flux densities obtained from the reference run. (b) Gray dots denote the benthic P efflux density obtained  
1331 from literature survey (Colman et al., 2000; Hartnett and Devol, 2003; Hensen et al., 1998; Ingall and Jahnke,  
1332 1994, 1997; McManus et al., 1997; Schenau and De Lange, 2001; Zabel et al., 1998), whereas gray and black  
1333 solid lines represent the simulated benthic P efflux density and burial flux density of reactive P obtained from  
1334 the reference run.



1335

1336 The global marine POC flux depends largely on water depth. Model-generated fluxes compare well with  
1337 independent estimates of deposition, burial, and regeneration. The gray line in Fig. 13a shows the simulated  
1338 sinking flux density of POC in the water column for LD region, compared with observations (Archer et al.,  
1339 2002; Baturin, 2007; Betts and Holland, 1991; Lutz et al., 2002). The preferential consumption of labile  
1340 compounds ( $G_1$  and  $G_2$ ) during the settling process leads to a continuous decrease in reactivity and therefore,  
1341 remineralization rates from the surface ocean down to the deep. Our estimate lies well within the range of  
1342 observations. The model tends to give lower fluxes than observed above 2,000 m water depth, and higher  
1343 below 5,000 m water depth. This is probably because of the assumption of homogeneous productivity in the  
1344 surface ocean. In the real ocean, oceanic productivity is generally greater at the continental margins than in  
1345 the pelagic gyre regions (Lutz et al., 2002). This is a model limitation, but the simulated biological pump is  
1346 sufficient to describe the general characteristics of global ocean biogeochemistry.

1347

1348 Of total exported POC, 91% ( $8.25 \text{ Gt C yr}^{-1}$ ) is decomposed in the water column and the rest ( $0.85 \text{ Gt C yr}^{-1}$ )  
1349 sinks to the sediment surface (Fig. 12a). The simulated global POC depositional flux is comparable not only  
1350 with observational estimates of  $0.93 \text{ Gt C yr}^{-1}$  (Muller-Karger et al., 2005) and  $0.67 \pm 0.48 \text{ Gt C yr}^{-1}$  for off-  
1351 shore regions (Dunne et al., 2007b), but also with an estimate using EMIC ( $0.87 \text{ Gt C yr}^{-1}$ ) (Ridgwell and  
1352 Hargreaves, 2007). The depositional fluxes of  $C_{\text{org}}$  in marginal ( $<2,000 \text{ m}$ ) and deep-sea sediments ( $>2,000$   
1353  $\text{m}$ ) are estimated at  $0.58 \text{ Gt C yr}^{-1}$  and  $0.27 \text{ Gt C yr}^{-1}$ , respectively. These estimates are slightly lower than  
1354 previous estimates of  $0.62\text{--}1.98 \text{ Gt C yr}^{-1}$  and  $0.31\text{--}0.62 \text{ Gt C yr}^{-1}$  (Bohlen et al., 2012; Burdige, 2007; Dunne  
1355 et al., 2007a; Muller-Karger et al., 2005).

1356

1357 In our standard run, benthic remineralization removes 7.9% of the exported POC ( $0.72 \text{ Gt C yr}^{-1}$ ), equivalent  
1358 of 84% of the global POC sedimentation rate. As a result, only 1.5% ( $0.135 \text{ Gt C yr}^{-1}$  or  $11.3 \text{ Tmol C yr}^{-1}$ ) of  
1359 the global POC export production is ultimately buried in marine sediments. Our model demonstrates that much  
1360 (91%) of the total burial occurs on the continental margins ( $<2,000 \text{ m}$  water depth), where the settling flux  
1361 and burial efficiency are relatively high. Previous studies (Dunne et al., 2007b; Muller-Karger et al., 2005)  
1362 estimated a  $C_{\text{org}}$  burial rate of  $0.29 \pm 0.15 \text{ Gt C yr}^{-1}$  and  $>0.06 \pm 0.06 \text{ Gt C yr}^{-1}$  at the margin. Our estimate of

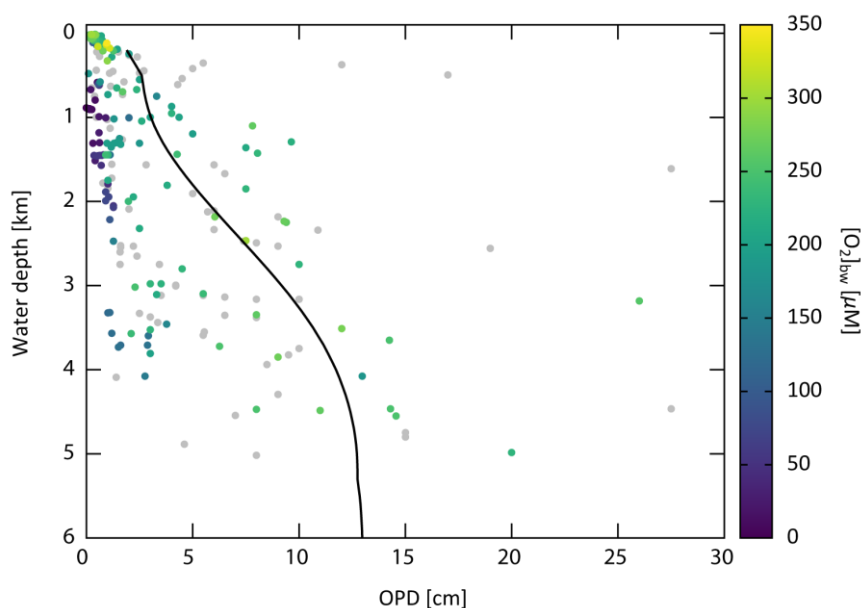


1363  $0.123 \text{ Gt C yr}^{-1}$  lies between these values, whereas our estimate for the deep sea,  $0.012 \text{ Gt C yr}^{-1}$ , is on the  
1364 lower end of previous estimates of  $0.012 \pm 0.02 \text{ Gt C yr}^{-1}$  (Dunne et al., 2007b) and  $0.017 \pm 0.005 \text{ Gt C yr}^{-1}$   
1365 (Hayes et al., 2021). Also, Hayes et al. (2021) and Sarmiento and Gruber (2006) estimated the burial rate  
1366 below 1,000 m as  $0.02 \pm 0.006 \text{ Gt C yr}^{-1}$ ; our estimate of  $0.019 \text{ Gt C yr}^{-1}$  is consistent with this. Combined with  
1367 the prescribed burial rate of terrigenous  $C_{\text{org}}$   $0.036 \text{ Gt C yr}^{-1}$  ( $3 \text{ Tmol C yr}^{-1}$ ), the total burial rate is calculated  
1368 to be  $0.17 \text{ Gt C yr}^{-1}$  ( $14.3 \text{ Tmol C yr}^{-1}$ ). This is somewhat higher than previous estimates (Bernier, 1982;  
1369 Burdige, 2005; Muller-Karger et al., 2005), but given the rather large uncertainty we consider it defensible.

1370

1371 Figure 14 shows OPD as a function of water depth. Although the benthic data could be biased towards highly  
1372 specific environments, such as sediments underlying upwelling areas and continental margins, our estimates  
1373 capture the general features of modern observations.

1374



1375

1376 **Figure 14** Oxygen penetration depth (OPD) as a function of water depth. Color dots denote the observational  
1377 data obtained from literature survey (Bradley et al., 2020; Devol and Christensen, 1993; Donis et al., 2016;  
1378 Gundersen and Jorgensen, 1990; Hartnett et al., 1998; Hedges et al., 1999; Hyacinthe et al., 2001; Martin and  
1379 Sayles, 2014; McManus et al., 2005; Morford and Emerson, 1999; Nierop et al., 2017; Pfeifer et al., 2002;  
1380 Rowe et al., 2008; Sachs et al., 2009). Colors represent the  $\text{O}_2$  concentration of bottom water (Gray dots  
1381 represents the unknown dissolved  $\text{O}_2$  concentration). The simulated OPD obtained from the reference run is  
1382 shown as a black line.



1383

### 1384 3.2.3 Phosphorus cycling

1385 The removal of phosphate from surface waters occurs through photosynthetic fixation by primary producers  
1386 and subsequent export in the form of POP into deeper waters, where it is largely remineralized back into DIP.  
1387 Through this process there is a vertical partitioning of DIP within the ocean with reduced surface  
1388 concentrations. Phosphorus export production is  $7.16 \text{ Tmol P yr}^{-1}$ , which is coupled with carbon according to  
1389 the POM compositional ratio (C:P = 106:1 for our standard model). The remineralization in the water column  
1390 ( $6.49 \text{ Tmol P yr}^{-1}$ ) and total sedimentation rate ( $0.672 \text{ Tmol P yr}^{-1}$ ) are also proportional to those of POC. In  
1391 contrast, the benthic DIP flux is decoupled from the carbon flux. Figure 13b shows modelled DIP benthic  
1392 efflux and burial flux together with observed fluxes. Some observational data showing a relatively large  
1393 abyssal (4–6 km) benthic flux are from upwelling regions in the South Atlantic (Hensen et al., 1998). The  
1394 deviation is therefore not critical for our globally averaged model. Our model gives the total benthic efflux of  
1395 DIP as  $0.517 \text{ Tmol P yr}^{-1}$ , which is roughly three times the riverine reactive P input rate. This is within the  
1396 range of previous estimates of  $0.05\text{--}1.25 \text{ Tmol P yr}^{-1}$  (Colman and Holland, 2000; Compton et al., 2000;  
1397 Wallmann, 2003b; Wallmann, 2010b).

1398

1399 The preservation efficiency (here defined as burial flux divided by the export flux) of P is 2.1%. This is higher  
1400 than that of organic carbon (1.5%), indicating that more P is trapped in marine sediments than might be  
1401 expected from Redfield stoichiometry. In oxic marine sediments, a fraction of the DIP released to pore waters  
1402 from POM decomposition can be absorbed by iron-oxyhydroxide or precipitated as authigenic fluorapatite  
1403 (Fig. 9). Therefore, the global averaged  $C_{\text{org}}/P_{\text{reac}}$  ratio of buried sediments is generally less than the Redfield  
1404 of 106 (approximately  $65 \pm 25$  based on observations; Algeo and Ingall, 2007). The modelled global average  
1405  $C_{\text{org}}/P_{\text{reac}}$  ratio of buried sediment is 73, consistent with this. The P burial fluxes of organic P, Fe-bound P and  
1406 authigenic P are estimated at  $0.044 \text{ Tmol P yr}^{-1}$ ,  $0.032 \text{ Tmol P yr}^{-1}$ , and  $0.079 \text{ Tmol P yr}^{-1}$ , respectively.

1407

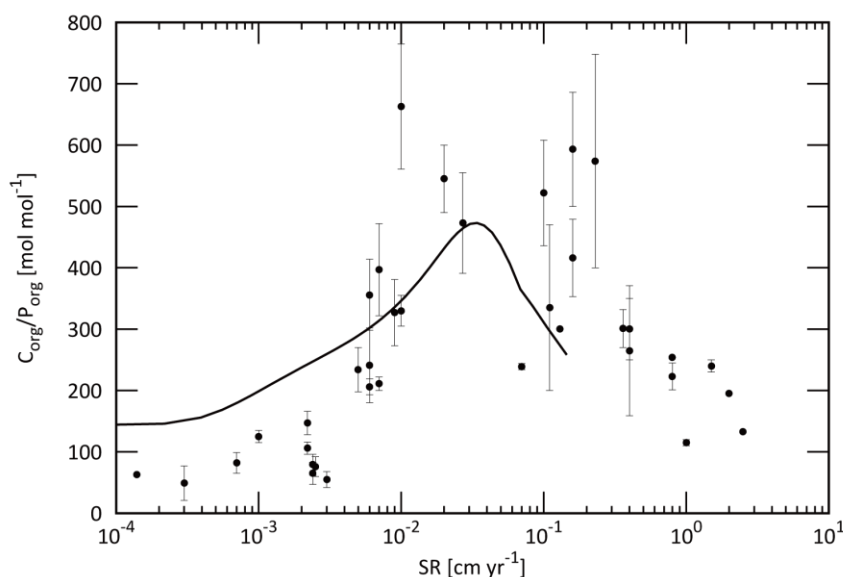
1408 The  $C_{\text{org}}/P_{\text{org}}$  ratio of burying organic matter shows a non-linear relationship with respect to sedimentation  
1409 rate. The observed  $C_{\text{org}}/P_{\text{org}}$  ratios are generally greater than the Redfield value of 106, especially for sediments



1410 in oxygen minimum zones (OMZs), which are characterized by a high depositional flux of organic matter  
1411 ( $C_{org}/P_{org}$  ratios up to 600 for the present open ocean) (Ingall and Cappellen, 1990). For example, the averaged  
1412  $C_{org}/P_{org}$  molar ratio at the Peru-Chile OMZ and Black Sea are 600, and the estimated burial ratio of sapropel  
1413 S1 of Mediterranean Sea is in the range of 400–800 (Slomp et al., 2002). This reflects the preferential  
1414 regeneration of P relative to C during microbial remineralization of marine organic matter and reflect the more  
1415 labile nature of P-biochemicals relative to most non-phosphorus containing organic carbon compounds.  
1416 Additional rationale for this observation is that P is preferentially targeted for remineralization to support  
1417 subsequent biological productivity as an essential and potentially limiting nutrient. Our model demonstrates  
1418 that we can reproduce the first-order relationship between  $C_{org}/P_{org}$  and sediment accumulation rate (Fig. 15).  
1419

1420 The modelled marine DIP inventory is  $2.75 \times 10^{15}$  mol, consistent with the observational estimate of around  
1421  $3 \times 10^{15}$  mol (e.g., Delaney, 1998; Guidry et al., 2000). Given the riverine reactive P input flux of  $0.155 \text{ Tmol}$   
1422  $\text{P yr}^{-1}$ , the phosphorus residence time is estimated at 18 kyr, which is also consistent with previous estimates  
1423 of 20 kyr or shorter (Benitez-Nelson, 2000; Ruttenberg, 2003).

1424



1425

1426 **Figure 15**  $C_{org}/P_{org}$  ratios of buried sediments as a function of sedimentation rate. Black dots represent the  
1427 observational data (Ingall and Cappellen, 1990). The simulated  $C_{org}/P_{org}$  ratios for the LD region obtained  
1428 from our reference run is shown as a black line.



1429

### 1430 **3.2.4 Nitrogen cycling**

1431 Nitrogen export production is  $1603 \text{ Tg N yr}^{-1}$ , which is coupled with carbon according to the C:N  
1432 stoichiometry of organic matter. Simulated N fixation required for the N balance in the ocean is  $180 \text{ Tg N yr}^{-1}$ ,  
1433 which is higher than the range of previous estimates of  $110\text{--}150 \text{ Tg N yr}^{-1}$  (Deutsch et al., 2007; Duce et al.,  
1434 2008; Fowler et al., 2013; Galloway et al., 2004; Gruber and Sarmiento, 1997; Karl et al., 2002; Luo et al.,  
1435 2012), while a recent study (Großkopf et al., 2012) suggests a higher value of  $\sim 180 \text{ Tg N yr}^{-1}$ . This discrepancy  
1436 is partly because atmospheric deposition is ignored in the CANOPS-GRB model, which contributes  $25.8 \text{ Tg N yr}^{-1}$   
1437 (Wang et al., 2019). Gruber and Sarmiento (2002) estimated the pre-industrial value of the total source  
1438 of N as  $188 \pm 44 \text{ Tg N yr}^{-1}$ . Our estimate of  $196 \text{ Tg N yr}^{-1}$  is within this range.

1439

1440 Nitrogen fluxes in an oxic water column are tightly coupled with the  $C_{\text{org}}$  fluxes, whereas decoupling appears  
1441 in suboxic environments. Simulated denitrification in the water column is  $102 \text{ Tg N yr}^{-1}$ , within the range of  
1442 the observational estimates ( $50\text{--}150 \text{ Tg N yr}^{-1}$ ) (Brandes and Devol, 2002; DeVries et al., 2012; DeVries et  
1443 al., 2013; Gruber, 2008; Gruber and Sarmiento, 2002; Oeschies et al., 2008; Wang et al., 2019). Modelled  
1444 benthic denitrification is  $62 \text{ Tg N yr}^{-1}$ , which is lower than the estimated range of  $90\text{--}300 \text{ Tg N yr}^{-1}$  (Brandes  
1445 and Devol, 2002; Devol, 2015; DeVries et al., 2012; DeVries et al., 2013; Eugster and Gruber, 2012; Wang  
1446 et al., 2019) by a factor of 1.5–5, suggesting that further efforts are required to improve representation of this  
1447 process. One possible explanation for this discrepancy is that our model is not sufficient to express benthic N  
1448 cycling because we ignore localized upwelling regions (such as the eastern Tropical Pacific and the Arabian  
1449 Sea) and coastal regions where benthic denitrification is significant POM decomposition pathway in favor of  
1450 globally averaged parameterizations. The separate treatment of continental shelves and margin sediments from  
1451 the pelagic ocean could improve this issue. We also ignore another denitrification mechanism: anaerobic  
1452 ammonium oxidation (anammox), which will often play an important role in the loss of fixed nitrogen in  
1453 marine sediments and pelagic anoxic zones (Karthäuser et al., 2021; Kuypers et al., 2005).

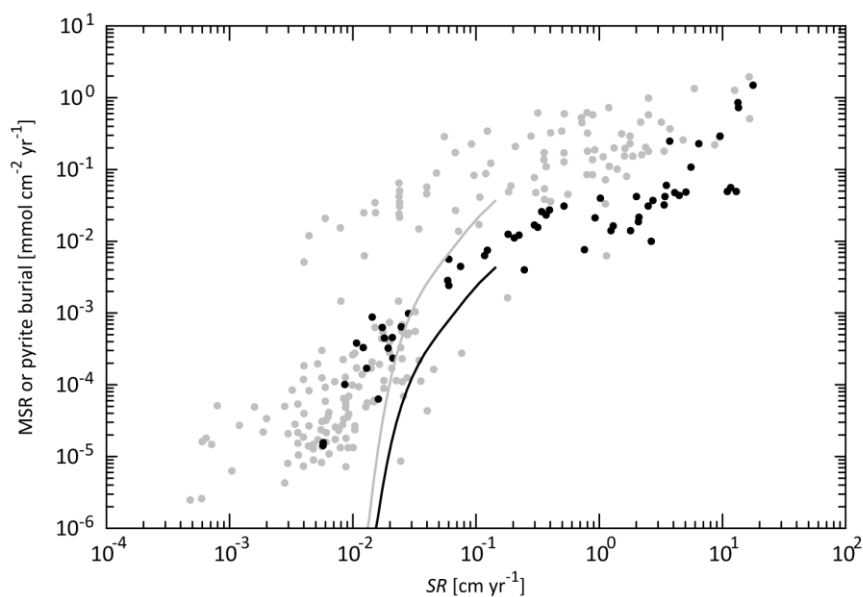
1454



1455 The modelled DIN inventory is  $4.5 \times 10^5$  Tg N. Given the total source flux of  $196 \text{ Tg N yr}^{-1}$ , the residence time  
1456 of DIN is estimated at 2.3 kyr.

### 1457 3.2.5 Sulfur cycling

1458 MSR is a major early diagenetic pathway of carbon oxidation in organic-rich sediments deposited below  
1459 oxygenated waters. For the standard run, aerobic oxidation is a dominant process in the water column, but  
1460 MSR contributes 37% of benthic degradation. CANOPS-GRB estimates a global rate of benthic sulfate  
1461 reduction at  $11 \text{ Tmol S yr}^{-1}$ . This is lower than the previously reported value of gross MSR ( $40\text{--}75 \text{ Tmol S yr}^{-1}$ ;  
1462 <sup>1</sup>; Canfield and Farquhar, 2009; Jørgensen and Kasten, 2006) but agrees better with net MSR (Bowles et al.,  
1463 2014). Bowles et al. (2014) have estimated global net MSR at  $6.2 \text{ Tmol S yr}^{-1}$  and  $11.3 \text{ Tmol S yr}^{-1}$  for  $z >$   
1464  $200 \text{ m}$  depth and  $z > 0 \text{ m}$  depth, respectively. Our estimate is within this range. MSR is most pronounced on  
1465 the shelf where high fluxes of organic matter to the seafloor lead to shallow OPD, high sulfide production,  
1466 and consequently high pyrite precipitation (Fig. 16).



1467

1468 **Figure 16** MSR and pyrite burial flux density as a function of sedimentation rate. Gray and black dots depict  
1469 observational data compilation of depth-integrated MSR flux density and pyrite burial flux density for normal  
1470 (oxic) marine sediments (Berner and Canfield, 1989; Canfield, 1989; Raiswell and Canfield, 2012). The unit  
1471 of sedimentation rate was converted from  $\text{g cm}^{-2} \text{ yr}^{-1}$  to  $\text{cm yr}^{-1}$  with assuming the dry bulk density of  $2.5 \text{ g}$   
1472  $\text{cm}^{-3}$  and porosity of 0.9. Solid lines are the results obtained from the reference run of the CANOPS-GRB  
1473 model.



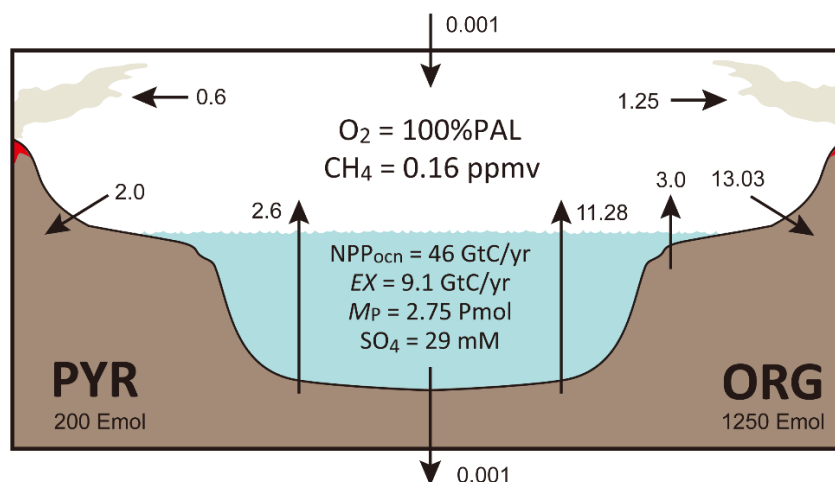
1474 In the CANOPS-GRB model, pyrite burial efficiency  $e_{\text{pyr}}$  (Sect. 2.3.4) for sediments underlying oxic bottom  
 1475 waters is set such that simulated seawater  $[\text{SO}_4^{2-}]$  of the reference run is consistent with the modern value of  
 1476 28.9 mM. The tuned value of 11.7% agrees well with observations suggesting that pyrite precipitation rate is  
 1477 about 10–20% of the rate of MSR (Fig. 16). Our reference value is also consistent with other estimates of  
 1478 11–20% (Bottrell and Newton, 2006a; Tarhan et al., 2015; Turchyn and Schrag, 2006b).

1479

1480 The sulfate inventory of our reference state is  $39 \times 10^{18}$  mol. Given the total source flux of  $3.4 \text{ Tmol S yr}^{-1}$ , the  
 1481 residence time of sulfate is 11.5 Myr.

### 1482 3.3 Global oxygen cycling

1483 The global  $\text{O}_2$  budget for our reference state is shown in Fig. 17. The simulated  $\text{O}_2$  inventory in the ocean-  
 1484 atmosphere system is  $38 \times 10^{18}$  mol (atmosphere =  $38 \times 10^{18}$  mol, ocean =  $0.23 \times 10^{18}$  mol). Organic carbon burial  
 1485 represents a major  $\text{O}_2$  source flux (marine =  $11.3 \text{ Tmol O}_2 \text{ equiv. yr}^{-1}$  and terrigenous =  $3 \text{ Tmol O}_2 \text{ equiv. yr}^{-1}$ ).  
 1486 Pyrite burial and hydrogen escape to space contribute  $2.6 \text{ Tmol O}_2 \text{ equiv. yr}^{-1}$  and  $0.001 \text{ Tmol O}_2 \text{ equiv. yr}^{-1}$ ,  
 1487 respectively. Given the total source/sink flux of  $16.9 \text{ Tmol O}_2 \text{ yr}^{-1}$ , the residence time of  $\text{O}_2$  in the ocean-  
 1488 atmosphere system of our reference state is estimated as 2.26 Myr, which is consistent with previous estimates  
 1489 of 2–4 Myr (Berner, 1989; Berner, 2004b; Garrels and Perry, 1974).



1490

1491 **Figure 17** Schematics of global redox ( $\text{O}_2$ ) budget for the reference run. Arrows represent the  $\text{O}_2$  flux in terms  
 1492 of  $10^{12} \text{ mol O}_2 \text{ equiv. yr}^{-1}$ . PAL = present atmospheric level. Pmol =  $10^{15} \text{ mol}$ . Emol =  $10^{18} \text{ mol}$ . ORG =  
 1493 sedimentary organic carbon. PYR = sedimentary pyrite sulfur.



## 1494 **4 Sensitivity experiment**

1495 Based on the results obtained above, we conclude that the CANOPS-GRB model is sufficient to describe basic  
1496 biogeochemical characteristics in the modern ocean-atmosphere system. As a next step, we assess the dynamic  
1497 response of the full model by performing sensitivity experiments with respect to P availability in surface  
1498 environments.

### 1499 **4.1 Dynamic response to changes in P weathering**

1500 Here, we conduct a sensitivity experiment with respect to the P weathering rate in order to see how the  
1501 atmospheric and oceanic O<sub>2</sub> levels respond to changes in P availability in the exogenic system over a wide  
1502 range of timescales. Specifically, we performed four simulations, varying the values of  $f_P$  in Eq. (2) over two  
1503 orders of magnitude. The reference state presented in the previous section is assumed for the initial condition,  
1504 and the full model is allowed to evolve freely for three billion model years. These experiments demonstrate  
1505 how P availability in surface environments affects global biogeochemical cycles and redox states of the  
1506 atmosphere and oceans over a diverse range of timescales.

1507

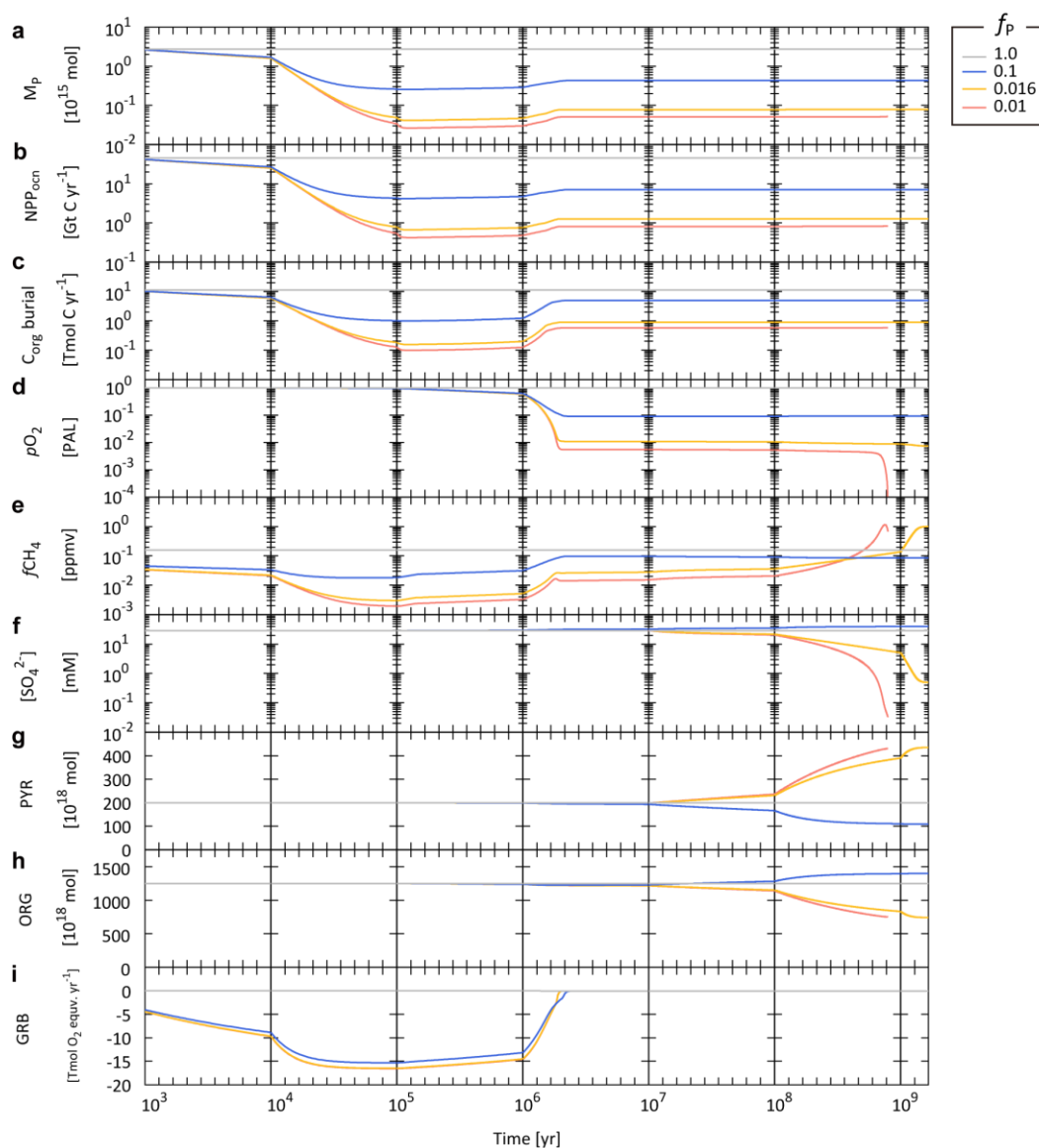
1508 The simulated transient response is shown in Fig. 18. As expected, lower P availability leads to lower oceanic  
1509 P inventory (Fig. 18a), resulting in suppressed biological productivity in the ocean (Fig. 18b). Given the  
1510 residence time of P in the ocean (20 kyr, see Sect. 3.2.4), these responses occur within 10<sup>5</sup> yr. The suppressed  
1511 biological productivity leads to a decline of burial rate of organic matter in sediments (Fig. 18c). Specifically,  
1512 10% and 1% of  $f_P$  give rise to the burial rate of marine C<sub>org</sub> of 1 Tmol C yr<sup>-1</sup> and 0.13 Tmol C yr<sup>-1</sup> at 10<sup>5</sup> yr,  
1513 respectively (cf. the reference value of 11.3 Tmol C yr<sup>-1</sup>).

1514

1515 On the timescales of 10<sup>5</sup>–10<sup>6</sup> yr, the system reaches a quasi-steady state, but there is still a large redox  
1516 imbalance due mainly to the suppression of C<sub>org</sub> burial (Fig. 18i). This gives rise to deoxygenation of the  
1517 atmosphere on a time scale of millions of years (Fig. 18d). Note that once the ocean interior becomes anoxic,  
1518 the enhanced P recycling and preservation of organic matter in anoxic marine sediments tend to buffer the  
1519 atmospheric deoxygenation (Figs. 18a and c). However, these passive responses do not alter the fundamental  
1520 behavior: lower P availability results in lower atmospheric O<sub>2</sub> levels. After atmospheric deoxygenation (>~4



1521 Myr), the system again reaches its quasi-steady state. Specifically,  $f_P$  values of 10% and 1% result in  
 1522 atmospheric  $O_2$  levels of 9% PAL and 0.6% PAL, respectively.



1523

1524 **Figure 18** Biogeochemical responses obtained from the CANOPS-GRB model with different values of P  
 1525 availability,  $f_P$ . (a) Oceanic phosphate inventory,  $M_P$ . (b) Oceanic net primary production ( $NPP_{ocn}$ ). (c) Burial  
 1526 rate of organic carbon ( $C_{org}$ ) in marine sediments. (d) Atmospheric partial pressure of  $O_2$ . PAL = present  
 1527 atmospheric level. (e) Atmospheric  $CH_4$  mixing ratio. (f) Sulfate concentration in the surface ocean layer. (g)  
 1528 Sedimentary reservoir size of pyrite sulfur,  $PYR$ . (h) Sedimentary reservoir size of organic carbon,  $ORG$ . (i)  
 1529 Global redox budget,  $GRB$ . For the  $f_P = 1\%$  run (black line), the calculation stopped when the atmospheric  $O_2$   
 1530 level decreased to  $\sim 10^{-5}$  PAL due to the numerical instability.



1531

1532 The following change is driven by the response of oceanic S cycle, which is characterized by the long residence  
1533 time of 11.5 Myr (see Sect. 3.2.6). Ocean anoxia promotes the MSR and subsequent precipitation of pyrite in  
1534 the ocean interior. However, our model demonstrates that the decline of seawater  $\text{SO}_4^{2-}$  on a timescale of tens  
1535 of millions of years is small (Fig. 18f), because the rate of MSR depends not only on the oceanic redox state  
1536 but on the availability of organic matter for the MSR. The significant reduction of seawater  $\text{SO}_4^{2-}$  occurs on  
1537 the longer timescales ( $>100$  Myr) for extremely low  $f_P$  scenarios (0.016 and 0.01), in which atmospheric  $\text{O}_2$   
1538 levels decrease to  $<1\%$  PAL. These scenarios also accompany with a growth of sedimentary S from gypsum  
1539 to pyrite (Fig. 18g).

1540

1541 On longer timescales, sedimentary reservoirs affect the redox state of the atmosphere and oceans. The present  
1542 result demonstrates that  $f_P$  of 1% finally leads to the catastrophic decrease in atmospheric  $\text{O}_2$  level at around  
1543 0.9 billion years (Fig. 18d). The simulation was stopped at this point due to the numerical instability. For other  
1544 scenarios, the system reaches a new steady state after roughly three billion model years.

1545

1546 Biogenic  $\text{CH}_4$  production tends to be enhanced in the anoxic oceans. However, the present result demonstrates  
1547 that  $\text{CH}_4$  degassing to the atmosphere is inhibited by both limited availability of organic matter for  
1548 methanogenesis and the anaerobic oxidation of  $\text{CH}_4$  by  $\text{SO}_4^{2-}$ . Once the seawater  $[\text{SO}_4^{2-}]$  decreases below 1  
1549 mM,  $\text{CH}_4$  can escape from oceans to the atmosphere, promoting the buildup of  $\text{CH}_4$  in the atmosphere.  
1550 Nevertheless, because of the limited biological activity, atmospheric  $\text{CH}_4$  levels are comparable to the modern  
1551 value ( $\sim 1$  ppmv) (Fig. 18e).

#### 1552 **4.2 $\text{O}_2$ budget for the less oxygenated scenario**

1553 Figure 19 shows the  $\text{O}_2$  budget of the less oxygenated state ( $f_P = 1.6\%$  scenario). Because P availability exerts  
1554 a primary control on biospheric  $\text{O}_2$  production, the strongly suppressed P delivery to the ocean leads to low  
1555 oceanic P levels and commensurately low biological productivity (0.08 Pmol and 1.3 Gt C  $\text{yr}^{-1}$ , respectively).  
1556 As a consequence, the atmospheric  $\text{O}_2$  level is low (0.75% PAL). In this scenario the ocean interior is globally  
1557 anoxic, and the preservation of organic C in marine sediments is enhanced. However, the suppressed biological

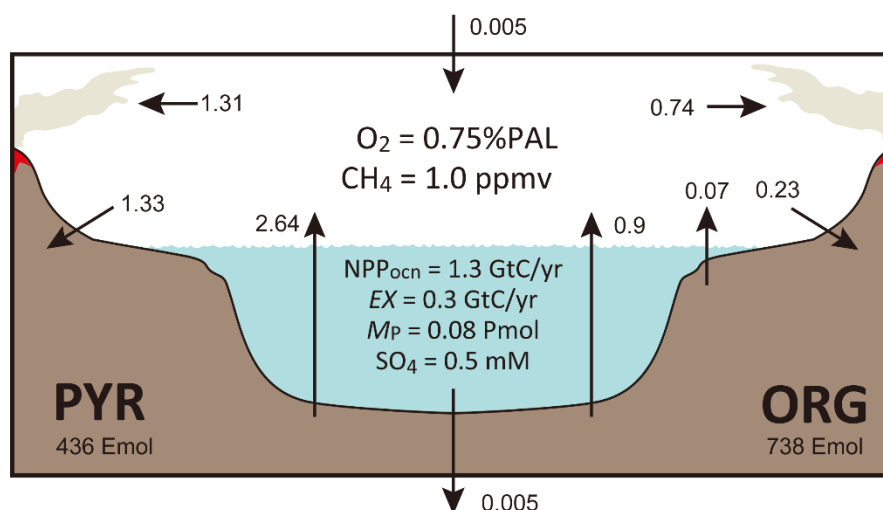


1558 productivity results in a low overall burial rate of organic C ( $0.9 \text{ Tmol O}_2 \text{ equiv. yr}^{-1}$ ; ~9% of the reference  
 1559 value). When combined with the burial rate of terrigenous organic C, total  $\text{O}_2$  production by the organic C  
 1560 sub-cycle is  $0.97 \text{ Tmol O}_2 \text{ equiv. yr}^{-1}$ . This  $\text{O}_2$  source is balanced by the sum of oxidative weathering and  
 1561 metamorphism. The role of the pyrite S sub-cycle in the global redox budget is also shown in Fig. 19. Most  
 1562 of the  $\text{SO}_4^{2-}$  entering the anoxic ocean is buried as pyrite, representing a major  $\text{O}_2$  source ( $2.64 \text{ Tmol O}_2 \text{ equiv.}$   
 1563  $\text{yr}^{-1}$ ). This  $\text{O}_2$  source is balanced by oxidation of sedimentary pyrite S through weathering ( $1.33 \text{ Tmol O}_2 \text{ equiv.}$   
 1564  $\text{yr}^{-1}$ ) and metamorphism ( $1.31 \text{ Tmol O}_2 \text{ equiv. yr}^{-1}$ ). In other words, the  $\text{O}_2$  budget for the weakly-oxygenated  
 1565 Earth system is largely controlled by the crustal S sub-cycle. This is in marked contrast to the well-oxygenated  
 1566 Earth system, on which the  $\text{O}_2$  budget is mainly controlled by organic C sub-cycle.

1567

1568 The present result demonstrates that low atmospheric  $\text{O}_2$  states (~1% PAL) can be achieved in scenarios where  
 1569 the availability of P is strongly limited. However, a slight decrease of  $f_P$  to 1% leads to the destabilization of  
 1570 global  $\text{O}_2$  budget, providing implications for the stability and evolution of atmospheric  $\text{O}_2$  levels during the  
 1571 Proterozoic. This point will be further systematically examined in future work.

1572



1573

1574 **Figure 19** Schematics of global redox ( $\text{O}_2$ ) budget for the  $f_P = 1.6\%$  ( $=10^{-1.8}$ ) run. Arrows represent the  $\text{O}_2$   
 1575 flux in terms of  $10^{12} \text{ mol O}_2 \text{ equiv. yr}^{-1}$ . PAL = present atmospheric level. Pmol =  $10^{15} \text{ mol}$ . Emol =  $10^{18} \text{ mol}$ .  
 1576 Gt C =  $10^{15} \text{ g C}$ . ORG = sedimentary organic C. PYR = sedimentary pyrite S.

1577



## 1578 **5 Discussion**

1579 The reference run under the present condition demonstrates generally good agreement with modern  
1580 observations (Sect. 3). The water circulation scheme provides an adequate representation of general ocean  
1581 circulation, resulting in robust and reliable tracer distributions that are comparable to the modern observations.  
1582 This provides a mechanistic foundation for simulating generalized ocean biogeochemical cycles. The ocean  
1583 biogeochemistry module includes a series of biogeochemical processes in oxic-anoxic-sulfidic environments.  
1584 The reference run gives rise to the distributions of nutrients and dissolved O<sub>2</sub> that capture fundamental  
1585 properties observed in the modern ocean. Integrated biogeochemical fluxes of the global ocean, such as  
1586 biological productivity, material flow in the water column, and burial into sediments are also consistent with  
1587 observational data. Some future developments to the N cycle may be needed, especially with regard to  
1588 denitrification (e.g., anammox, coastal benthic denitrification). Nevertheless, our ocean biogeochemical  
1589 model is adequate for representing the general property of the coupled C-N-P-O<sub>2</sub>-S cycles.

1590

1591 A new scheme for oxidative weathering of organic matter and pyrite sulfur, mass balance calculation of O<sub>2</sub> in  
1592 the atmosphere, and time evolution of sedimentary reservoirs are explicitly included in the CANOPS-GRB  
1593 model. These are a significant improvement from the previous versions of CANOPS (Lenton, 2020). The  
1594 simplified framework for the global O<sub>2</sub> budget is also useful to understand the response of complex  
1595 biogeochemical systems. The computational efficiency of our CANOPS-GRB model allows us to conduct  
1596 simulations over billions of model years with reasonable wall times (on the order of weeks), providing a useful  
1597 tool for exploring the wide range of topics about the oxygenation history of Earth's atmosphere.

1598

1599 Sensitivity experiments with respect to the terrestrial weathering rate of P were conducted in order to see how  
1600 the redox state of the ocean-atmosphere system responds to varying P availability in the surface system (Sect.  
1601 4). The CANOPS-GRB model appears to adequately simulate the biogeochemical dynamics over a wide range  
1602 of timescales and is applicable for quantitative assessment of the evolution and stability of Earth's O<sub>2</sub> cycling.  
1603 Perhaps even more importantly, our results encourage us to perform further systematic examinations with  
1604 Earth system models which have different complexities. Such an 'Earth system model intercomparison' would



1605 be a critical step towards better mechanistic understanding of the stability and dynamics of atmospheric O<sub>2</sub>  
1606 levels over Earth's history.

1607

1608 Due to a lack of explicit Fe cycling and anaerobic metabolisms (such as anoxygenic photosynthesis), the  
1609 current version of the model cannot be applicable for the simulation under the Archean-like weakly-  
1610 oxygenated ( $pO_2 < 10^{-5}$  PAL) conditions. These topics are left to future studies, but it would be an achievable  
1611 goal (Ozaki et al., 2018; Ozaki et al., 2019b; van de Velde et al., 2021). The model design presented here also  
1612 ignores the interaction between the surface system and the mantle (e.g., subduction) except for the degassing  
1613 of reducing gases from the mantle. We note, however, that the surface-mantle interaction would have exerted  
1614 a primary control on the long-term redox budget of Earth's surface system through the Earth's history  
1615 (Canfield, 2004; Eguchi et al., 2020; Hayes and Waldbauer, 2006) and may be important for the discussion  
1616 about the distant future (Ozaki and Reinhard, 2021). The importance of mantle and solid Earth controls on  
1617 surficial environments is a crucially important topic for future research.



## 1618 **6 Conclusions**

1619 A new Earth system box model was developed—CANOPS-GRB. The new code release provides an improved  
1620 description of the coupled C-N-P-O<sub>2</sub>-S biogeochemical cycles in the ocean-atmosphere-crust system, which  
1621 can be utilized to examine the dynamics and stability of Earth's O<sub>2</sub> cycle over a wide range of timescales. The  
1622 computational efficiency and simple model design of CANOPS-GRB make it relatively easy to modify  
1623 existing processes or add entirely new processes and components. CANOPS-GRB is thus a new and uniquely  
1624 flexible tool capable of providing a coherent mechanistic framework for quantifying the biogeochemical  
1625 cycles regulating Earth's O<sub>2</sub> cycle. CANOPS-GRB is also a useful tool for the development of more  
1626 comprehensive, low- to intermediate-complexity Earth system box models of biogeochemistry.

1627

1628 CANOPS-GRB will provide an important step forward when coupled to new and existing geochemical proxy  
1629 data. The accumulating geological/geochemical records have led to new hypothesis for the evolution of  
1630 atmospheric O<sub>2</sub> levels on Earth. CANOPS-GRB was designed to facilitate simulation of a wide range of past  
1631 conditions so as to permit more explicit testing of hypothesis about the function of biogeochemical cycles and  
1632 its effect on the redox budget through Earth history. Through the model-data synergy, CANOPS-GRB has a  
1633 great potential to provide an integrated, quantitative, and statistically informative picture of biogeochemical  
1634 states, opening new perspectives on a wide range of scientific questions in research seeking to understand the  
1635 Earth's chemical evolution, and in particular the cause-and-effect relationships with evolving biosphere.

1636

1637 CANOPS-GRB also provides significant steps forward in our predictive understanding of the links between  
1638 geology, biogeochemistry, and the evolution of Earth's biosphere. It will allow for a fundamentally new and  
1639 more precise quantitative understanding of evolving atmospheric biosignatures (O<sub>2</sub>, O<sub>3</sub>, CH<sub>4</sub>) on Earth, and  
1640 will broaden the interpretive power of Earth system evolution in the search for life beyond our planet.  
1641 CANOPS-GRB could be a central piece for developing a more robust tool for diagnosing atmospheric  
1642 biosignatures for future analysis of extrasolar worlds. In sum, it is anticipated that CANOPS-GRB will have  
1643 many applications for problems linking the coupled evolution of life and the atmosphere on Earth and  
1644 habitable rocky exoplanets.

1645



1646

1647 **Code availability.** The bulk of CANOPS-GRB is written in Fortran as a stand-alone model. The model code  
1648 can be found at GitHub (doi:10.5281/zenodo.5893804). This model is still undergoing regular development  
1649 and it is recommended that potential users contact the corresponding author (Kazumi Ozaki;  
1650 kazumi.ozaki@sci.toho-u.ac.jp) to obtain the latest version. The CANOPS-GRB code is provided freely but  
1651 with the requirement that prospective users contact the corresponding author with their research plans to avoid  
1652 parallel projects emerging.

1653

1654 **Author contributions.** KO designed the study, wrote the code, and ran model simulations. DBC and CTR  
1655 contributed to code debugging. KO wrote the manuscript, with inputs from DBC, CTR, and ET.

1656

1657 **Competing interests.** The authors declare that they have no conflict of interest.

1658

1659 **Acknowledgements.** This work was supported by JSPS KAKENHI Grant Number JP16K05618, 19K21055,  
1660 and JP20K04066. CTR acknowledges the NASA Exobiology Program (Grant Number 80NSSC19K0461) and  
1661 the NASA Interdisciplinary Consortia for Astrobiology Research (ICAR) (Grant Number 80NSSC21K0594).

1662



## 1663 References

- 1664 Alcott, L. J., Mills, B. J. W., and Poulton, S. W.: Stepwise Earth oxygenation is an inherent property of global  
1665 biogeochemical cycling, *Science*, 366, 1333-1337, 2019.
- 1666 Algeo, T. J. and Ingall, E.: Sedimentary C<sub>org</sub>:P ratios, paleocean ventilation, and Phanerozoic atmospheric pO<sub>2</sub>,  
1667 *Palaeogeogr. Palaeoclimatol. Palaeoecol.*, 256, 130-155, 2007.
- 1668 Anderson, L. D., Delaney, M. L., and Faul, K. L.: Carbon to phosphorus ratios in sediments: Implications for  
1669 nutrient cycling, *Glob. Biogeochem. Cycles*, 15, 65-79, 2001.
- 1670 Archer, D., Kheshgi, H., and Maier-Reimer, E.: Dynamics of fossil fuel CO<sub>2</sub> neutralization by marine CaCO<sub>3</sub>,  
1671 *Glob. Biogeochem. Cycles*, 12, 259-276, 1998.
- 1672 Archer, D. E., Eshel, G., Winguth, A., Broecker, W., Pierrehumbert, R., Tobis, M., and Jacob, R.: Atmospheric  
1673 pCO<sub>2</sub> sensitivity to the biological pump in the ocean, *Glob. Biogeochem. Cycles*, 14, 1219-1230, 2000.
- 1674 Archer, D. E., Morford, J. L., and Emerson, S. R.: A model of suboxic sedimentary diagenesis suitable for  
1675 automatic tuning and gridded global domains, *Glob. Biogeochem. Cycles*, 16, 17-11-17-21, 2002.
- 1676 Armstrong, R. A., Lee, C., Hedges, J. I., Honjo, S., and Wakeham, S. G.: A new, mechanistic model for  
1677 organic carbon fluxes in the ocean based on the quantitative association of POC with ballast minerals,  
1678 *Deep Sea Research Part II: Topical Studies in Oceanography*, 49, 219-236, 2001.
- 1679 Arndt, S., Regnier, P., Godderis, Y., and Donnadieu, Y.: GEOCLIM *reloaded* (v 1.0): a new coupled earth  
1680 system model for past climate change, *Geoscientific Model Development*, 4, 451-481, 2011.
- 1681 Baturin, G. N.: Issue of the relationship between primary productivity of organic carbon in ocean and  
1682 phosphate accumulation (Holocene-Late Jurassic), *Lithology and Mineral Resources*, 42, 318-348, 2007.
- 1683 Beal, E. J., Claire, M. W., and House, C. H.: High rates of anaerobic methanotrophy at low sulfate  
1684 concentrations with implications for past and present methane levels, *Geobiology*, 9, 131-139, 2011.
- 1685 Belcher, C. M. and McElwain, J. C.: Limits for combustion in low O<sub>2</sub> redefine paleoatmospheric predictions  
1686 for the Mesozoic, *Science*, 321, 1197-1200, 2008.
- 1687 Bellefroid, E. J., Hood, A. v. S., Hoffman, P. F., Thomas, M. D., Reinhard, C. T., and Planavsky, N. J.:  
1688 Constraints on Paleoproterozoic atmospheric oxygen levels, *Proc. Natl Acad. Sci. USA*, 115, 8104-8109,  
1689 2018.
- 1690 Benitez-Nelson, C. R.: The biogeochemical cycling of phosphorus in marine systems, *Earth-Science Reviews*,  
1691 51, 109-135, 2000.
- 1692 Berelson, W. M.: The Flux of Particulate Organic Carbon Into the Ocean Interior: A Comparison of Four U.S.  
1693 JGOFS Regional Studies, *Oceanography*, 14, 2001a.
- 1694 Berelson, W. M.: Particle settling rates increase with depth in the ocean, *Deep Sea Research Part II: Topical  
1695 Studies in Oceanography*, 49, 237-251, 2001b.
- 1696 Berelson, W. M., Balch, W. M., Najjar, R., Feely, R. A., Sabine, C., and Lee, K.: Relating estimates of CaCO<sub>3</sub>  
1697 production, export, and dissolution in the water column to measurements of CaCO<sub>3</sub> rain into sediment  
1698 traps and dissolution on the sea floor: A revised global carbonate budget, *Glob. Biogeochem. Cycles*, 21,  
1699 2007.
- 1700 Bergman, N. M., Lenton, T. M., and Watson, A. J.: COPSE: A new model of biogeochemical cycling over  
1701 Phanerozoic time, *Am. J. Sci.*, 304, 397-437, 2004.
- 1702 Berner, R. A.: Biogeochemical cycles of carbon and sulfur and their effect on atmospheric oxygen over  
1703 phanerozoic time, *Palaeogeogr. Palaeoclimatol. Palaeoecol.*, 75, 97-122, 1989.



- 1704 Berner, R. A.: Burial of organic carbon and pyrite sulfur in the modern ocean; its geochemical and  
1705 environmental significance, *Am. J. Sci.*, 282, 451-473, 1982.
- 1706 Berner, R. A.: *Early diagenesis: A theoretical approach*, Princeton University Press, Princeton, 1980.
- 1707 Berner, R. A.: GEOCARBSULF: A combined model for Phanerozoic atmospheric O<sub>2</sub> and CO<sub>2</sub>, *Geochim.*  
1708 *Cosmochim. Acta*, 70, 5653-5664, 2006.
- 1709 Berner, R. A.: A model for calcium, magnesium and sulfate in seawater over Phanerozoic time, *Am. J. Sci.*,  
1710 304, 438-453, 2004a.
- 1711 Berner, R. A.: Phanerozoic atmospheric oxygen: New results using the GEOCARBSULF model, *Am. J. Sci.*,  
1712 309, 603-606, 2009.
- 1713 Berner, R. A.: *The Phanerozoic Carbon Cycle: CO<sub>2</sub> and O<sub>2</sub>*, Oxford University Press, 2004b.
- 1714 Berner, R. A. and Canfield, D. E.: A new model for atmospheric oxygen over Phanerozoic time, *Am. J. Sci.*,  
1715 289, 333-361, 1989.
- 1716 Berner, R. A. and Westrich, J. T.: Bioturbation and the early diagenesis of carbon and sulfur, *Am. J. Sci.*, 285,  
1717 193-206, 1985.
- 1718 Betts, J. N. and Holland, H. D.: The oxygen content of ocean bottom waters, the burial efficiency of organic  
1719 carbon, and the regulation of atmospheric oxygen, *Palaeogeogr. Palaeoclimatol. Palaeoecol.*, 97, 5-18,  
1720 1991.
- 1721 Bohlen, L., Dale, A. W., and Wallmann, K.: Simple transfer functions for calculating benthic fixed nitrogen  
1722 losses and C:N:P regeneration ratios in global biogeochemical models, *Glob. Biogeochem. Cycles*, 26,  
1723 n/a-n/a, 2012.
- 1724 Bolton, E. W., Berner, R. A., and Petsch, S. T.: The Weathering of Sedimentary Organic Matter as a Control  
1725 on Atmospheric O<sub>2</sub>: II. Theoretical Modeling, *Am. J. Sci.*, 306, 575-615, 2006.
- 1726 Bottrell, S. H. and Newton, R. J.: Reconstruction of changes in global sulfur cycling from marine sulfate  
1727 isotopes, *Earth-Science Reviews*, 75, 59-83, 2006a.
- 1728 Bottrell, S. H. and Newton, R. J.: Reconstruction of changes in global sulfur cycling from marine sulfate  
1729 isotopes, *Earth-Science Reviews*, 75, 59-83, 2006b.
- 1730 Boudreau, B. P.: A method-of-lines code for carbon and nutrient diagenesis in aquatic sediments, *Computers*  
1731 *& Geosciences*, 22, 479-496, 1996.
- 1732 Bowles, M. W., Mogollón, J. M., Kasten, S., Zabel, M., and Hinrichs, K.-U.: Global rates of marine sulfate  
1733 reduction and implications for sub-sea-floor metabolic activities, *Science*, 344, 889-891, 2014.
- 1734 Bradley, J. A., Arndt, S., Amend, J. P., Burwicz, E., Dale, A. W., Egger, M., and LaRowe, D. E.: Widespread  
1735 energy limitation to life in global subseafloor sediments, *Science Advances*, 6, eaba0697, 2020.
- 1736 Brandes, J. A. and Devol, A. H.: A global marine-fixed nitrogen isotopic budget: Implications for Holocene  
1737 nitrogen cycling, *Glob. Biogeochem. Cycles*, 16, GB001856, 2002.
- 1738 Broecker, W. S. and Peng, T.-H.: *Tracers in the sea*, Eldigio Pr, New York, 1982.
- 1739 Burdige, D. J.: Burial of terrestrial organic matter in marine sediments: A re-assessment, *Glob. Biogeochem.*  
1740 *Cycles*, 19, 2005.
- 1741 Burdige, D. J.: Preservation of Organic Matter in Marine Sediments: Controls, Mechanisms, and an Imbalance  
1742 in Sediment Organic Carbon Budgets?, *Chemical Reviews*, 107, 467-485, 2007.
- 1743 Canfield, D. E.: The evolution of the Earth surface sulfur reservoir, *Am. J. Sci.*, 304, 839-861, 2004.



- 1744 Canfield, D. E.: Organic Matter Oxidation in Marine Sediments. In: Interactions of C, N, P and S  
1745 Biogeochemical Cycles and Global Change, Wollast, R., Mackenzie, F. T., and Chou, L. (Eds.), Springer  
1746 Berlin Heidelberg, Berlin, 1993.
- 1747 Canfield, D. E.: Sulfate reduction and oxic respiration in marine sediments: implications for organic carbon  
1748 preservation in euxinic environments, *Deep Sea Research Part A. Oceanographic Research Papers*, 36,  
1749 121-138, 1989.
- 1750 Canfield, D. E.: Sulfate reduction in deep-sea sediments, *Am. J. Sci.*, 291, 177-188, 1991.
- 1751 Canfield, D. E. and Farquhar, J.: Animal evolution, bioturbation, and the sulfate concentration of the oceans,  
1752 *Proc. Natl Acad. Sci. USA*, 106, 8123-8127, 2009.
- 1753 Canfield, D. E., Zhang, S., Frank, A. B., Wang, X., Wang, H., Su, J., Ye, Y., and Frei, R.: Highly fractionated  
1754 chromium isotopes in Mesoproterozoic-aged shales and atmospheric oxygen, *Nature Commun.*, 9, 2871,  
1755 2018.
- 1756 Carr, M.-E., Friedrichs, M. A. M., Schmeltz, M., Noguchi Aita, M., Antoine, D., Arrigo, K. R., Asanuma, I.,  
1757 Aumont, O., Barber, R., Behrenfeld, M., Bidigare, R., Buitenhuis, E. T., Campbell, J., Ciotti, A., Dierssen,  
1758 H., Dowell, M., Dunne, J., Esaias, W., Gentili, B., Gregg, W., Groom, S., Hoepffner, N., Ishizaka, J.,  
1759 Kameda, T., Le Quéré, C., Lohrenz, S., Marra, J., Mélin, F., Moore, K., Morel, A., Reddy, T. E., Ryan, J.,  
1760 Scardi, M., Smyth, T., Turpie, K., Tilstone, G., Waters, K., and Yamanaka, Y.: A comparison of global  
1761 estimates of marine primary production from ocean color, *Deep Sea Research Part II: Topical Studies in*  
1762 *Oceanography*, 53, 741-770, 2006.
- 1763 Catling, D. C. and Kasting, J. F.: *Atmospheric Evolution on Inhabited and Lifeless Worlds*, Cambridge  
1764 University Press, Cambridge, 2017.
- 1765 Catling, D. C. and Zahnle, K. J.: The Archean atmosphere, *Science Advances*, 6, eaax1420, 2020.
- 1766 Cha, H. J., Lee, C. B., Kim, B. S., Choi, M. S., and Ruttenger, K. C.: Early diagenetic redistribution and  
1767 burial of phosphorus in the sediments of the southwestern East Sea (Japan Sea), *Marine Geology*, 216,  
1768 127-143, 2005.
- 1769 Claire, M. W., Catling, D. C., and Zahnle, K. J.: Biogeochemical modelling of the rise in atmospheric oxygen,  
1770 *Geobiology*, 4, 239-269, 2006.
- 1771 Cole, D. B., Ozaki, K., and Reinhard, C. T.: Atmospheric Oxygen Abundance, Marine Nutrient Availability,  
1772 and Organic Carbon Fluxes to the Seafloor, *Glob. Biogeochem. Cycles*, 36, e2021GB007052, 2022.
- 1773 Cole, D. B., Reinhard, C. T., Wang, X., Gueguen, B., Halverson, G. P., Gibson, T., Hodgskiss, M. S. W.,  
1774 McKenzie, N. R., Lyons, T. W., and Planavsky, N. J.: A shale-hosted Cr isotope record of low atmospheric  
1775 oxygen during the Proterozoic, *Geology*, 44, 555-558, 2016.
- 1776 Colman, A. S. and Holland, H. D.: The global diagenetic flux of phosphorus from marine sediments to the  
1777 oceans: redox sensitivity and the control of atmospheric oxygen levels. In: *Marine authigenesis: from*  
1778 *global to microbial*, Glenn, C. R., Prevot-Lucas, L., and Lucas, J. (Eds.), SEPM (Society for Sedimentary  
1779 Geology), 2000.
- 1780 Colman, A. S., Holland, H. D., Glenn, C. R., Prévôt-Lucas, L., and Lucas, J.: The Global Diagenetic Flux of  
1781 Phosphorus from Marine Sediments to the Oceans: Redox Sensitivity and the Control of Atmospheric  
1782 Oxygen Levels. In: *Marine Authigenesis: From Global to Microbial*, SEPM Society for Sedimentary  
1783 Geology, 2000.



- 1784 Compton, J., Mallinson, D., Glenn, C. R., Filippelli, G., Follmi, K., Shields, G. A., and Zanin, Y.: Variations  
1785 in the global phosphorus cycle. In: *Marine authigenesis: from global to microbial*, Glenn, C. R., Prevot-  
1786 Lucas, L., and Lucas, J. (Eds.), SEPM (Society for Sedimentary Geology), 2000.
- 1787 Crichton, K. A., Wilson, J. D., Ridgwell, A., and Pearson, P. N.: Calibration of temperature-dependent ocean  
1788 microbial processes in the cGENIE.muffin (v0.9.13) Earth system model, *Geosci. Model Dev.*, 14, 125-  
1789 149, 2021.
- 1790 Crockford, P. W., Hayles, J. A., Bao, H., Planavsky, N. J., Bekker, A., Fralick, P. W., Halverson, G. P., Bui,  
1791 T. H., Peng, Y., and Wing, B. A.: Triple oxygen isotope evidence for limited mid-Proterozoic primary  
1792 productivity, *Nature*, 559, 613-616, 2018.
- 1793 Daines, S. J., Mills, B. J. W., and Lenton, T. M.: Atmospheric oxygen regulation at low Proterozoic levels by  
1794 incomplete oxidative weathering of sedimentary organic carbon, *Nature Commun.*, 8, 14379, 2017.
- 1795 Dale, A. W., Meyers, S. R., Aguilera, D. R., Arndt, S., and Wallmann, K.: Controls on organic carbon and  
1796 molybdenum accumulation in Cretaceous marine sediments from the Cenomanian–Turonian interval  
1797 including Oceanic Anoxic Event 2, *Chem. Geol.*, 324–325, 28-45, 2012.
- 1798 Delaney, M. L.: Phosphorus accumulation in marine sediments and the oceanic phosphorus cycle, *Glob.*  
1799 *Biogeochem. Cycles*, 12, 563-572, 1998.
- 1800 Dellwig, O., Leipe, T., März, C., Glockzin, M., Pollehne, F., Schnetger, B., Yakushev, E. V., Böttcher, M. E.,  
1801 and Brumsack, H.-J.: A new particulate Mn–Fe–P-shuttle at the redoxcline of anoxic basins, *Geochim.*  
1802 *Cosmochim. Acta*, 74, 7100-7115, 2010.
- 1803 Derry, L. A.: Causes and consequences of mid-Proterozoic anoxia, *Geophys. Res. Lett.*, 42, 2015GL065333,  
1804 2015.
- 1805 Des Marais, D. J., Harwit, M. O., Jucks, K. W., Kasting, J. F., Lin, D. N., Lunine, J. I., Schneider, J., Seager,  
1806 S., Traub, W. A., and Woolf, N. J.: Remote Sensing of Planetary Properties and Biosignatures on  
1807 Extrasolar Terrestrial Planets, *Astrobiology*, 2, 153-181, 2002.
- 1808 Deutsch, C., Sarmiento, J. L., Sigman, D. M., Gruber, N., and Dunne, J. P.: Spatial coupling of nitrogen inputs  
1809 and losses in the ocean, *Nature*, 445, 163, 2007.
- 1810 Devol, A. and Christensen, J. P.: Benthic fluxes and nitrogen cycling in sediments of the continental margin  
1811 of the eastern North Pacific, *Journal of Marine Research*, 51, 345-372, 1993.
- 1812 Devol, A. H.: Denitrification, Anammox, and N<sub>2</sub> Production in Marine Sediments, *Ann. Rev. Mar. Sci.*, 7,  
1813 403-423, 2015.
- 1814 DeVries, T., Deutsch, C., Primeau, F., Chang, B., and Devol, A.: Global rates of water-column denitrification  
1815 derived from nitrogen gas measurements, *Nat. Geosci.*, 5, 547, 2012.
- 1816 DeVries, T., Deutsch, C., Rafter, P. A., and Primeau, F.: Marine denitrification rates determined from a global  
1817 3-D inverse model, *Biogeosciences*, 10, 2481-2496, 2013.
- 1818 Doney, S. C., Lindsay, K., Caldeira, K., Campin, J. M., Drange, H., Dutay, J. C., Follows, M., Gao, Y.,  
1819 Gnanadesikan, A., Gruber, N., Ishida, A., Joos, F., Madec, G., Maier-Reimer, E., Marshall, J. C., Matear,  
1820 R. J., Monfray, P., Mouchet, A., Najjar, R., Orr, J. C., Plattner, G. K., Sarmiento, J., Schlitzer, R., Slater,  
1821 R., Totterdell, I. J., Weirig, M. F., Yamanaka, Y., and Yool, A.: Evaluating global ocean carbon models:  
1822 The importance of realistic physics, *Glob. Biogeochem. Cycles*, 18, GB3017, 2004.
- 1823 Donis, D., McGinnis, D. F., Holtappels, M., Felden, J., and Wenzhofer, F.: Assessing benthic oxygen fluxes  
1824 in oligotrophic deep sea sediments (HAUSGARTEN observatory), *Deep-Sea Research Part I-*  
1825 *Oceanographic Research Papers*, 111, 1-10, 2016.



- 1826 Duce, R. A., LaRoche, J., Altieri, K., Arrigo, K. R., Baker, A. R., Capone, D. G., Cornell, S., Dentener, F.,  
1827 Galloway, J., Ganeshram, R. S., Geider, R. J., Jickells, T., Kuypers, M. M., Langlois, R., Liss, P. S., Liu,  
1828 S. M., Middelburg, J. J., Moore, C. M., Nickovic, S., Oschlies, A., Pedersen, T., Prospero, J., Schlitzer, R.,  
1829 Seitzinger, S., Sorensen, L. L., Uematsu, M., Ulloa, O., Voss, M., Ward, B., and Zamora, L.: Impacts of  
1830 Atmospheric Anthropogenic Nitrogen on the Open Ocean, *Science*, 320, 893-897, 2008.
- 1831 Dunne, J. P., Sarmiento, J. L., and Gnanadesikan, A.: A synthesis of global particle export from the surface  
1832 ocean and cycling through the ocean interior and on the seafloor, *Glob. Biogeochem. Cycles*, 21, n/a-n/a,  
1833 2007a.
- 1834 Dunne, J. P., Sarmiento, J. L., and Gnanadesikan, A.: A synthesis of global particle export from the surface  
1835 ocean and cycling through the ocean interior and on the seafloor, *Glob. Biogeochem. Cycles*, 21, GB4006,  
1836 2007b.
- 1837 Eguchi, J., Seales, J., and Dasgupta, R.: Great Oxidation and Lomagundi events linked by deep cycling and  
1838 enhanced degassing of carbon, *Nat. Geosci.*, 13, 71-76, 2020.
- 1839 Etheridge, D. M., Steele, L. P., Francey, R. J., and Langenfelds, R. L.: Atmospheric methane between 1000  
1840 A.D. and present: Evidence of anthropogenic emissions and climatic variability, *J. Geophys. Res.*, 103,  
1841 15979-15993, 1998.
- 1842 Eugster, O. and Gruber, N.: A probabilistic estimate of global marine N-fixation and denitrification, *Glob.*  
1843 *Biogeochem. Cycles*, 26, 2012.
- 1844 Föllmi, K. B.: The phosphorus cycle, phosphogenesis and marine phosphate-rich deposits, *Earth-Science*  
1845 *Reviews*, 40, 55-124, 1996.
- 1846 Fakhraee, M., Planavsky, N. J., and Reinhard, C. T.: The role of environmental factors in the long-term  
1847 evolution of the marine biological pump, *Nat. Geosci.*, 13, 812-816, 2020.
- 1848 Fiebig, J., Woodland, A. B., D'Alessandro, W., and Püttmann, W.: Excess methane in continental  
1849 hydrothermal emissions is abiogenic, *Geology*, 37, 495-498, 2009.
- 1850 Filippelli, G. M.: Carbon and phosphorus cycling in anoxic sediments of the Saanich Inlet, British Columbia,  
1851 *Marine Geology*, 174, 307-321, 2001.
- 1852 Fowler, D., Coyle, M., Skiba, U., Sutton, M. A., Cape, J. N., Reis, S., Sheppard, L. J., Jenkins, A., Grizzetti,  
1853 B., Galloway, J. N., Vitousek, P., Leach, A., Bouwman, A. F., Butterbach-Bahl, K., Dentener, F.,  
1854 Stevenson, D., Amann, M., and Voss, M.: The global nitrogen cycle in the twenty-first century, *Phil. Trans.*  
1855 *R. Soc. B*, 368, 2013.
- 1856 Francois, R., Honjo, S., Krishfield, R., and Manganini, S.: Factors controlling the flux of organic carbon to  
1857 the bathypelagic zone of the ocean, *Glob. Biogeochem. Cycles*, 16, 1087, 2002.
- 1858 Froelich, P. N., Klinkhammer, G. P., Bender, M. L., Luedtke, N. A., Heath, G. R., Cullen, D., Dauphin, P.,  
1859 Hammond, D., Hartman, B., and Maynard, V.: Early oxidation of organic matter in pelagic sediments of  
1860 the eastern equatorial Atlantic: suboxic diagenesis, *Geochim. Cosmochim. Acta*, 43, 1075-1090, 1979.
- 1861 Galbraith, E. D. and Martiny, A. C.: A simple nutrient-dependence mechanism for predicting the  
1862 stoichiometry of marine ecosystems, *Proc. Natl Acad. Sci. USA*, 112, 8199-8204, 2015.
- 1863 Galloway, J. N., Dentener, F. J., Capone, D. G., Boyer, E. W., Howarth, R. W., Seitzinger, S. P., Asner, G. P.,  
1864 Cleveland, C. C., Green, P. A., Holland, E. A., Karl, D. M., Michaels, A. F., Porter, J. H., Townsend, A.  
1865 R., and Vöosmarty, C. J.: Nitrogen Cycles: Past, Present, and Future, *Biogeochemistry*, 70, 153-226, 2004.
- 1866 Garcia, H. E. and Gordon, L. I.: Oxygen solubility in seawater: Better fitting equations, *Limnology and*  
1867 *Oceanography*, 37, 1307-1312, 1992.



- 1868 Garrels, R. M. and Lerman, A.: Phanerozoic cycles of sedimentary carbon and sulfur, *Proc. Natl Acad. Sci.*  
1869 USA, 78, 4652-4656, 1981.
- 1870 Garrels, R. M. and Perry, J. E. A.: *Cycling of carbon, sulfur, and oxygen through geologic time*, Wiley-  
1871 Interscience, New York, 1974.
- 1872 Goldblatt, C., Lenton, T. M., and Watson, A. J.: Bistability of atmospheric oxygen and the Great Oxidation,  
1873 *Nature*, 443, 683-686, 2006.
- 1874 Graham, W. F. and Duce, R. A.: Atmospheric pathways of the phosphorus cycle, *Geochim. Cosmochim. Acta*,  
1875 43, 1195-1208, 1979.
- 1876 Großkopf, T., Mohr, W., Baustian, T., Schunck, H., Gill, D., Kuypers, M. M. M., Lavik, G., Schmitz, R. A.,  
1877 Wallace, D. W. R., and LaRoche, J.: Doubling of marine dinitrogen-fixation rates based on direct  
1878 measurements, *Nature*, 488, 361, 2012.
- 1879 Gruber, N.: Chapter 1 - The Marine Nitrogen Cycle: Overview and Challenges. In: *Nitrogen in the Marine*  
1880 *Environment (2nd Edition)*, Academic Press, San Diego, 2008.
- 1881 Gruber, N. and Sarmiento, J. L.: Biogeochemical/physical interactions in elemental cycles. In: *THE SEA:*  
1882 *Biological-Physical Interactions in the Oceans*, Robinson, A. R., McCarthy, J. J., and Rothschild, B. J.  
1883 (Eds.), John Wiley and Sons, New York, 2002.
- 1884 Gruber, N. and Sarmiento, J. L.: Global patterns of marine nitrogen fixation and denitrification, *Glob.*  
1885 *Biogeochem. Cycles*, 11, 235-266, 1997.
- 1886 Guidry, M. W., Mackenzie, F. T., and Arvidson, R. S.: Role of tectonics in phosphorus distribution and cycling.  
1887 In: *Marine Authigenesis: From Global to Microbial*, Glenn, C. R., Prevot-Lucas, L., and Lucas, J. (Eds.),  
1888 *SEPM*, 2000.
- 1889 Gundersen, J. K. and Jorgensen, B. B.: Microstructure of diffusive boundary layers and the oxygen uptake of  
1890 the sea floor, *Nature*, 345, 604, 1990.
- 1891 Halevy, I., Peters, S. E., and Fischer, W. W.: Sulfate Burial Constraints on the Phanerozoic Sulfur Cycle,  
1892 *Science*, 337, 331-334, 2012.
- 1893 Handoh, I. C. and Lenton, T. M.: Periodic mid-Cretaceous oceanic anoxic events linked by oscillations of the  
1894 phosphorus and oxygen biogeochemical cycles, *Glob. Biogeochem. Cycles*, 17, 1092, 2003.
- 1895 Hartnett, H. E. and Devol, A. H.: Role of a strong oxygen-deficient zone in the preservation and degradation  
1896 of organic matter: a carbon budget for the continental margins of northwest Mexico and Washington State,  
1897 *Geochim. Cosmochim. Acta*, 67, 247-264, 2003.
- 1898 Hartnett, H. E., Keil, R. G., Hedges, J. I., and Devol, A. H.: Influence of oxygen exposure time on organic  
1899 carbon preservation in continental margin sediments, *Nature*, 391, 572-575, 1998.
- 1900 Hayes, C. T., Costa, K. M., Anderson, R. F., Calvo, E., Chase, Z., Demina, L. L., Dutay, J.-C., German, C. R.,  
1901 Heimbürger-Boavida, L.-E., Jaccard, S. L., Jacobel, A., Kohfeld, K. E., Kravchishina, M. D., Lippold, J.,  
1902 Mekik, F., Missiaen, L., Pavia, F. J., Paytan, A., Pedrosa-Pamies, R., Petrova, M. V., Rahman, S.,  
1903 Robinson, L. F., Roy-Barman, M., Sanchez-Vidal, A., Shiller, A., Tagliabue, A., Tessin, A. C., van Hulten,  
1904 M., and Zhang, J.: Global Ocean Sediment Composition and Burial Flux in the Deep Sea, *Glob.*  
1905 *Biogeochem. Cycles*, 35, e2020GB006769, 2021.
- 1906 Hayes, J. M. and Waldbauer, J. R.: The carbon cycle and associated redox processes through time, *Phil. Trans.*  
1907 *R. Soc. B*, 361, 931-950, 2006.
- 1908 Hedges, J. I., Hu, F. S., Devol, A. H., Hartnett, H. E., Tsamakis, E., and Keil, R. G.: Sedimentary organic  
1909 matter preservation; a test for selective degradation under oxic conditions, *Am. J. Sci.*, 299, 529-555, 1999.



- 1910 Heinze, C., Kriest, I., and Maier-Reimer, E.: Age offsets among different biogenic and lithogenic components  
1911 of sediment cores revealed by numerical modeling, *Paleoceanography*, 24, n/a-n/a, 2009.
- 1912 Henrichs, S. M. and Reeburgh, W. S.: Anaerobic mineralization of marine sediment organic matter: Rates and  
1913 the role of anaerobic processes in the oceanic carbon economy, *Geomicrobiology Journal*, 5, 191-237,  
1914 1987.
- 1915 Hensen, C., Landenberger, H., Zabel, M., and Schulz, H. D.: Quantification of diffusive benthic fluxes of  
1916 nitrate, phosphate, and silicate in the southern Atlantic Ocean, *Glob. Biogeochem. Cycles*, 12, 193-210,  
1917 1998.
- 1918 Hitchcock, D. R. and Lovelock, J. E.: Life detection by atmospheric analysis, *Icarus*, 7, 149-159, 1967.
- 1919 Holland, H. D.: *The Chemistry of the Atmosphere and Oceans*, John Wiley & Sons, New York, 1978.
- 1920 Holser, W. T., Maynard, J. B., and Cruikshank, K. M.: Modelling the natural cycle of sulphur through  
1921 Phanerozoic time. In: *Evolution of the Global Biogeochemical Sulphur Cycle*, Brimblecombe, P. and Lein,  
1922 A. Y. (Eds.), John Wiley & Sons Ltd, New York, 1989.
- 1923 Honjo, S.: Material fluxes and modes of sedimentation in the mesopelagic and bathypelagic zones, *Journal of*  
1924 *Marine Research*, 38, 53-97, 1980.
- 1925 Honjo, S. and Manganini, S. J.: Annual biogenic particle fluxes to the interior of the North Atlantic Ocean;  
1926 studied at 34°N 21°W and 48°N 21°W, *Deep Sea Research Part II: Topical Studies in Oceanography*, 40,  
1927 587-607, 1993.
- 1928 Hotinski, R. M., Kump, L. R., and Najjar, R. G.: Opening Pandora's Box: The impact of open system modeling  
1929 on interpretations of anoxia, *Paleoceanography*, 15, 267-279, 2000.
- 1930 Hyacinthe, C., Anschutz, P., Carbonel, P., Jouanneau, J. M., and Jorissen, F. J.: Early diagenetic processes in  
1931 the muddy sediments of the Bay of Biscay, *Marine Geology*, 177, 111-128, 2001.
- 1932 Ingall, E. and Jahnke, R.: Evidence for enhanced phosphorus regeneration from marine sediments overlain by  
1933 oxygen depleted waters, *Geochim. Cosmochim. Acta*, 58, 2571-2575, 1994.
- 1934 Ingall, E. and Jahnke, R.: Influence of water-column anoxia on the elemental fractionation of carbon and  
1935 phosphorus during sediment diagenesis, *Marine Geology*, 139, 219-229, 1997.
- 1936 Ingall, E. D., Bustin, R. M., and Van Cappellen, P.: Influence of water column anoxia on the burial and  
1937 preservation of carbon and phosphorus in marine shales, *Geochim. Cosmochim. Acta*, 57, 303-316, 1993.
- 1938 Ingall, E. D. and Cappellen, P. V.: Relation between sedimentation rate and burial of organic phosphorus and  
1939 organic carbon in marine sediments, *Geochim. Cosmochim. Acta*, 54, 373-386, 1990.
- 1940 Ittekkot, V.: The abiotically driven biological pump in the ocean and short-term fluctuations in atmospheric  
1941 CO<sub>2</sub> contents, *Global and Planetary Change*, 8, 17-25, 1993.
- 1942 Jørgensen, B. B.: Mineralization of organic matter in the sea bed—the role of sulphate reduction, *Nature*, 296,  
1943 643, 1982.
- 1944 Jørgensen, B. B. and Kasten, S.: *Sulfur cycling and methane oxidation*. 2006.
- 1945 Jahnke, R. A.: The global ocean flux of particulate organic carbon: Areal distribution and magnitude, *Glob.*  
1946 *Biogeochem. Cycles*, 10, 71-88, 1996.
- 1947 Joos, F., Sarmiento, J. L., and Siegenthaler, U.: Estimates of the effect of Southern Ocean iron fertilization on  
1948 atmospheric CO<sub>2</sub> concentrations, *Nature*, 349, 772-775, 1991.
- 1949 Kagoshima, T., Sano, Y., Takahata, N., Maruoka, T., Fischer, T. P., and Hattori, K.: Sulphur geodynamic  
1950 cycle, *Sci Rep*, 5, 8330, 2015.



- 1951 Karl, D., Michaels, A., Bergman, B., Capone, D., Carpenter, E., Letelier, R., Lipschultz, F., Paerl, H., Sigman,  
1952 D., and Stal, L.: Dinitrogen fixation in the world's oceans. In: *The Nitrogen Cycle at Regional to Global*  
1953 *Scales*, Boyer, E. W. and Howarth, R. W. (Eds.), Springer Netherlands, Dordrecht, 2002.
- 1954 Karl, D. M., Beversdorf, L., Björkman, K. M., Church, M. J., Martinez, A., and Delong, E. F.: Aerobic  
1955 production of methane in the sea, *Nat. Geosci.*, 1, 473-478, 2008.
- 1956 Karthäuser, C., Ahmerkamp, S., Marchant, H. K., Bristow, L. A., Hauss, H., Iversen, M. H., Kiko, R., Maerz,  
1957 J., Lavik, G., and Kuypers, M. M. M.: Small sinking particles control anammox rates in the Peruvian  
1958 oxygen minimum zone, *Nature Commun.*, 12, 3235, 2021.
- 1959 Kashiyama, Y., Ozaki, K., and Tajika, E.: Impact of the Evolution of Carbonate Ballasts on Marine  
1960 Biogeochemistry in the Mesozoic and Associated Changes in Energy Delivery to Subsurface Waters,  
1961 *Paleontological Research*, 15, 89-99, 2011.
- 1962 Katsev, S. and Crowe, S. A.: Organic carbon burial efficiencies in sediments: The power law of mineralization  
1963 revisited, *Geology*, 43, 607-610, 2015.
- 1964 Key, R. M., Olsen, A., van Heuven, S., Lauvset, S. K., Velo, A., Lin, X., Schirnick, C., Kozyr, A., Tanhua,  
1965 T., Hoppema, M., Jutterström, S., Steinfeldt, R., Jeansson, E., Ishii, M., Perez, F. F., and Suzuki, T.: Global  
1966 Ocean Data Analysis Project, Version 2 (GLODAPv2). Carbon Dioxide Information Analysis Center, Oak  
1967 Ridge Nat Lab, 2015.
- 1968 Kharecha, P., Kasting, J., and Siefert, J.: A coupled atmosphere–ecosystem model of the early Archean Earth,  
1969 *Geobiology*, 3, 53-76, 2005.
- 1970 Klaas, C. and Archer, D. E.: Association of sinking organic matter with various types of mineral ballast in the  
1971 deep sea: Implications for the rain ratio, *Glob. Biogeochem. Cycles*, 16, 63-61-63-14, 2002.
- 1972 Knox, F. and McElroy, M. B.: Changes in atmospheric CO<sub>2</sub>: Influence of the marine biota at high latitude, *J.*  
1973 *Geophys. Res.*, 89, 4629-4637, 1984.
- 1974 Krissansen-Totton, J., Garland, R., Irwin, P., and Catling, D. C.: Detectability of Biosignatures in Anoxic  
1975 Atmospheres with the James Webb Space Telescope: A TRAPPIST-1e Case Study, *The Astronomical*  
1976 *Journal*, 156, 114, 2018.
- 1977 Kump, L. R.: Chemical stability of the atmosphere and ocean, *Palaeogeogr. Palaeoclimatol. Palaeoecol.*, 75,  
1978 123-136, 1989.
- 1979 Kump, L. R.: The rise of atmospheric oxygen, *Nature*, 451, 277-278, 2008.
- 1980 Kuypers, M. M. M., Lavik, G., Woebken, D., Schmid, M., Fuchs, B. M., Amann, R., Jørgensen, B. B., and  
1981 Jetten, M. S. M.: Massive nitrogen loss from the Benguela upwelling system through anaerobic ammonium  
1982 oxidation, *Proc. Natl Acad. Sci. USA*, 102, 6478-6483, 2005.
- 1983 Kuznetsov, I., Neumann, T., and Burchard, H.: Model study on the ecosystem impact of a variable C:N:P ratio  
1984 for cyanobacteria in the Baltic Proper, *Ecological Modelling*, 219, 107-114, 2008.
- 1985 Laakso, T. A. and Schrag, D. P.: Regulation of atmospheric oxygen during the Proterozoic, *Earth Planet. Sci.*  
1986 *Lett.*, 388, 81-91, 2014.
- 1987 Larsson, U., Hajdu, S., Walve, J., and Elmgren, R.: Baltic Sea nitrogen fixation estimated from the summer  
1988 increase in upper mixed layer total nitrogen, *Limnology and Oceanography*, 46, 811-820, 2001.
- 1989 Lasaga, A. C.: A new approach to isotopic modeling of the variation of atmospheric oxygen through the  
1990 Phanerozoic, *Am. J. Sci.*, 289, 411-435, 1989.
- 1991 Lasaga, A. C. and Ohmoto, H.: The oxygen geochemical cycle: dynamics and stability, *Geochim. Cosmochim.*  
1992 *Acta*, 66, 361-381, 2002.



- 1993 Laws, E. A., Falkowski, P. G., Smith, W. O., Ducklow, H., and McCarthy, J. J.: Temperature effects on export  
1994 production in the open ocean, *Glob. Biogeochem. Cycles*, 14, 1231-1246, 2000.
- 1995 Ledwell, J. R., Watson, A. J., and Law, C. S.: Mixing of a tracer in the pycnocline, *J. Geophys. Res.*, 103,  
1996 21499-21529, 1998.
- 1997 Lenton, T. M.: Fire Feedbacks on Atmospheric Oxygen. In: *Fire Phenomena and the Earth System*, 2013.
- 1998 Lenton, T. M.: On the use of models in understanding the rise of complex life, *Interface Focus*, 10, 20200018,  
1999 2020.
- 2000 Lenton, T. M., Dahl, T. W., Daines, S. J., Mills, B. J. W., Ozaki, K., Saltzman, M. R., and Porada, P.: Earliest  
2001 land plants created modern levels of atmospheric oxygen, *Proc. Natl Acad. Sci. USA*, 113, 9704-9709,  
2002 2016.
- 2003 Lenton, T. M., Daines, S. J., and Mills, B. J. W.: COPSE reloaded: An improved model of biogeochemical  
2004 cycling over Phanerozoic time, *Earth-Science Reviews*, 178, 1-28, 2018.
- 2005 Lenton, T. M. and Watson, A. J.: Redfield revisited: 1. Regulation of nitrate, phosphate, and oxygen in the  
2006 ocean, *Glob. Biogeochem. Cycles*, 14, 225-248, 2000a.
- 2007 Lenton, T. M. and Watson, A. J.: Redfield revisited: 2. What regulates the oxygen content of the atmosphere?,  
2008 *Glob. Biogeochem. Cycles*, 14, 249-268, 2000b.
- 2009 Lin, S. and Morse, J. W.: Sulfate reduction and iron sulfide mineral formation in Gulf of Mexico anoxic  
2010 sediments, *Am. J. Sci.*, 291, 55-89, 1991.
- 2011 Liss, P. S. and Slater, P. G.: Flux of Gases across the Air-Sea Interface, *Nature*, 247, 181-184, 1974.
- 2012 Lord, N. S., Ridgwell, A., Thorne, M. C., and Lunt, D. J.: An impulse response function for the “long tail” of  
2013 excess atmospheric CO<sub>2</sub> in an Earth system model, *Glob. Biogeochem. Cycles*, 30, 2-17, 2016.
- 2014 Lovelock, J. E.: Gaia as seen through the atmosphere, *Atmospheric Environment*, 6, 579-580, 1972.
- 2015 Lovelock, J. E.: A Physical Basis for Life Detection Experiments, *Nature*, 207, 568-570, 1965.
- 2016 Lovelock, J. E.: Thermodynamics and the recognition of alien biospheres, *Proceedings of the Royal Society  
2017 of London. Series B. Biological Sciences*, 189, 167-181, 1975.
- 2018 Lumpkin, R. and Speer, K.: Global Ocean Meridional Overturning, *Journal of Physical Oceanography*, 37,  
2019 2550-2562, 2007.
- 2020 Luo, Y. W., Doney, S. C., Anderson, L. A., Benavides, M., Berman-Frank, I., Bode, A., Bonnet, S., Boström,  
2021 K. H., Böttjer, D., Capone, D. G., Carpenter, E. J., Chen, Y. L., Church, M. J., Dore, J. E., Falcón, L. I.,  
2022 Fernández, A., Foster, R. A., Furuya, K., Gómez, F., Gundersen, K., Hynes, A. M., Karl, D. M., Kitajima,  
2023 S., Langlois, R. J., LaRoche, J., Letelier, R. M., Marañón, E., McGillicuddy Jr, D. J., Moisaner, P. H.,  
2024 Moore, C. M., Mouriño-Carballido, B., Mulholland, M. R., Needoba, J. A., Orcutt, K. M., Poulton, A. J.,  
2025 Rahav, E., Raimbault, P., Rees, A. P., Riemann, L., Shiozaki, T., Subramaniam, A., Tyrrell, T., Turk-Kubo,  
2026 K. A., Varela, M., Villareal, T. A., Webb, E. A., White, A. E., Wu, J., and Zehr, J. P.: Database of  
2027 diazotrophs in global ocean: abundance, biomass and nitrogen fixation rates, *Earth Syst. Sci. Data*, 4, 47-  
2028 73, 2012.
- 2029 Lutz, M., Dunbar, R., and Caldeira, K.: Regional variability in the vertical flux of particulate organic carbon  
2030 in the ocean interior, *Glob. Biogeochem. Cycles*, 16, 11-11-11-18, 2002.
- 2031 Lyons, T. W. and Gill, B. C.: Ancient Sulfur Cycling and Oxygenation of the Early Biosphere, *Elements*, 6,  
2032 93-99, 2010.
- 2033 Lyons, T. W., Reinhard, C. T., and Planavsky, N. J.: The rise of oxygen in Earth's early ocean and atmosphere,  
2034 *Nature*, 506, 307-315, 2014.



- 2035 Mackenzie, F. T., Ver, L. M., Sabine, C., Lane, M., and Lerman, A.: C, N, P, S Global Biogeochemical Cycles  
2036 and Modeling of Global Change. In: Interactions of C, N, P and S Biogeochemical Cycles and Global  
2037 Change, Wollast, R., Mackenzie, F. T., and Chou, L. (Eds.), Springer Berlin Heidelberg, Berlin,  
2038 Heidelberg, 1993.
- 2039 Maier-Reimer, E.: Geochemical cycles in an ocean general circulation model. Preindustrial tracer distributions,  
2040 *Glob. Biogeochem. Cycles*, 7, 645-677, 1993.
- 2041 Markovic, S., Paytan, A., and Wortmann, U. G.: Pleistocene sediment offloading and the global sulfur cycle,  
2042 *Biogeosciences*, 12, 3043-3060, 2015.
- 2043 Martin, J. H., Knauer, G. A., Karl, D. M., and Broenkow, W. W.: VERTEX: carbon cycling in the northeast  
2044 Pacific, *Deep Sea Research Part A. Oceanographic Research Papers*, 34, 267-285, 1987.
- 2045 Martin, W. R. and Sayles, F. L.: The Recycling of Biogenic Material at the Sea Floor. In: *Treatise on*  
2046 *Geochemistry (Second Edition)*, Turekian, K. K. (Ed.), Elsevier, Oxford, 2014.
- 2047 Mayor, M. and Queloz, D.: A Jupiter-mass companion to a solar-type star, *Nature*, 378, 355-359, 1995.
- 2048 McManus, J., Berelson, W. M., Coale, K. H., Johnson, K. S., and Kilgore, T. E.: Phosphorus regeneration in  
2049 continental margin sediments, *Geochim. Cosmochim. Acta*, 61, 2891-2907, 1997.
- 2050 McManus, J., Berelson, W. M., Klinkhammer, G. P., Hammond, D. E., and Holm, C.: Authigenic uranium:  
2051 Relationship to oxygen penetration depth and organic carbon rain, *Geochim. Cosmochim. Acta*, 69, 95-  
2052 108, 2005.
- 2053 Meadows, V. S.: Reflections on O<sub>2</sub> as a Biosignature in Exoplanetary Atmospheres, *Astrobiology*, 17, 1022-  
2054 1052, 2017.
- 2055 Meadows, V. S., Reinhard, C. T., Arney, G. N., Parenteau, M. N., Schwieterman, E. W., Domagal-Goldman,  
2056 S. D., Lincowski, A. P., Stapelfeldt, K. R., Rauer, H., DasSarma, S., Hegde, S., Narita, N., Deitrick, R.,  
2057 Lustig-Yaeger, J., Lyons, T. W., Siegler, N., and Grenfell, J. L.: Exoplanet Biosignatures: Understanding  
2058 Oxygen as a Biosignature in the Context of Its Environment, *Astrobiology*, 18, 630-662, 2018.
- 2059 Middelburg, J. J., Soetaert, K., and Herman, P. M. J.: Empirical relationships for use in global diagenetic  
2060 models, *Deep Sea Research Part I: Oceanographic Research Papers*, 44, 327-344, 1997.
- 2061 Middelburg, J. J., Soetaert, K., Herman, P. M. J., and Heip, C. H. R.: Denitrification in marine sediments: A  
2062 model study, *Glob. Biogeochem. Cycles*, 10, 661-673, 1996.
- 2063 Millero, F. J.: *Chemical Oceanography*, Taylor & Francis Group CRC Press, Boca Raton, 2006.
- 2064 Millero, F. J.: The oxidation of H<sub>2</sub>S in Black Sea waters, *Deep Sea Research Part A. Oceanographic Research*  
2065 *Papers*, 38, S1139-S1150, 1991.
- 2066 Millero, F. J., Plese, T., and Fernandez, M.: The dissociation of hydrogen-sulfide in seawater, *Limnology and*  
2067 *Oceanography*, 33, 269-274, 1988.
- 2068 Morford, J. L. and Emerson, S.: The geochemistry of redox sensitive trace metals in sediments, *Geochim.*  
2069 *Cosmochim. Acta*, 63, 1735-1750, 1999.
- 2070 Muller-Karger, F. E., Varela, R., Thunell, R., Luerssen, R., Hu, C., and Walsh, J. J.: The importance of  
2071 continental margins in the global carbon cycle, *Geophys. Res. Lett.*, 32, 2005.
- 2072 National Academies of Sciences, E. and Medicine: *An Astrobiology Strategy for the Search for Life in the*  
2073 *Universe*, The National Academies Press, Washington, DC, 2019.
- 2074 Nierop, K. G. J., Reichart, G.-J., Veld, H., and Sinninghe Damsté, J. S.: The influence of oxygen exposure  
2075 time on the composition of macromolecular organic matter as revealed by surface sediments on the Murray  
2076 Ridge (Arabian Sea), *Geochim. Cosmochim. Acta*, 206, 40-56, 2017.



- 2077 Oguz, T., Ducklow, H. W., and Malanotte-Rizzoli, P.: Modeling distinct vertical biogeochemical structure of  
2078 the Black Sea: Dynamical coupling of the oxic, suboxic, and anoxic layers, *Glob. Biogeochem. Cycles*,  
2079 14, 1331-1352, 2000.
- 2080 Oguz, T., Murray, J. W., and Callahan, A. E.: Modeling redox cycling across the suboxic–anoxic interface  
2081 zone in the Black Sea, *Deep Sea Research Part I: Oceanographic Research Papers*, 48, 761-787, 2001.
- 2082 Olsen, A., Key, R. M., van Heuven, S., Lauvset, S. K., Velo, A., Lin, X., Schirnick, C., Kozyr, A., Tanhua,  
2083 T., Hoppema, M., Jutterström, S., Steinfeldt, R., Jeansson, E., Ishii, M., Pérez, F. F., and Suzuki, T.: The  
2084 Global Ocean Data Analysis Project version 2 (GLODAPv2) – an internally consistent data product for  
2085 the world ocean, *Earth Syst. Sci. Data*, 8, 297-323, 2016.
- 2086 Olson, S. L., Reinhard, C. T., and Lyons, T. W.: Limited role for methane in the mid-Proterozoic greenhouse,  
2087 *Proc. Natl Acad. Sci. USA*, 113, 11447-11452, 2016.
- 2088 Oshlies, A., Schulz, K. G., Riebesell, U., and Schmittner, A.: Simulated 21st century's increase in oceanic  
2089 suboxia by CO<sub>2</sub>-enhanced biotic carbon export, *Glob. Biogeochem. Cycles*, 22, GB4008, 2008.
- 2090 Ozaki, K. and Reinhard, C. T.: The future lifespan of Earth's oxygenated atmosphere, *Nat. Geosci.*, 14, 138-  
2091 142, 2021.
- 2092 Ozaki, K., Reinhard, C. T., and Tajika, E.: A sluggish mid-Proterozoic biosphere and its effect on Earth's  
2093 redox balance, *Geobiology*, 17, 3-11, 2019a.
- 2094 Ozaki, K. and Tajika, E.: Biogeochemical effects of atmospheric oxygen concentration, phosphorus  
2095 weathering, and sea-level stand on oceanic redox chemistry: Implications for greenhouse climates, *Earth  
2096 Planet. Sci. Lett.*, 373, 129-139, 2013.
- 2097 Ozaki, K., Tajika, E., Hong, P. K., Nakagawa, Y., and Reinhard, C. T.: Effects of primitive photosynthesis on  
2098 Earth's early climate system, *Nat. Geosci.*, 11, 55-59, 2018.
- 2099 Ozaki, K., Tajima, S., and Tajika, E.: Conditions required for oceanic anoxia/euxinia: Constraints from a one-  
2100 dimensional ocean biogeochemical cycle model, *Earth Planet. Sci. Lett.*, 304, 270-279, 2011.
- 2101 Ozaki, K., Thompson, K. J., Simister, R. L., Crowe, S. A., and Reinhard, C. T.: Anoxygenic photosynthesis  
2102 and the delayed oxygenation of Earth's atmosphere, *Nature Commun.*, 10, 3026, 2019b.
- 2103 Pallud, C. and Van Cappellen, P.: Kinetics of microbial sulfate reduction in estuarine sediments, *Geochim.  
2104 Cosmochim. Acta*, 70, 1148-1162, 2006.
- 2105 Petsch, S. T. and Berner, R. A.: Coupling the geochemical cycles of C, P, Fe, and S; the effect on atmospheric  
2106 O<sub>2</sub> and the isotopic records of carbon and sulfur, *Am. J. Sci.*, 298, 246-262, 1998.
- 2107 Petsch, S. T., Eglinton, T. I., and Edwards, K. J.: <sup>14</sup>C-Dead Living Biomass: Evidence for Microbial  
2108 Assimilation of Ancient Organic Carbon During Shale Weathering, *Science*, 292, 1127-1131, 2001.
- 2109 Pfeifer, K., Hensen, C., Adler, M., Wenzhfer, F., Weber, B., and Schulz, H. D.: Modeling of subsurface calcite  
2110 dissolution, including the respiration and reoxidation processes of marine sediments in the region of  
2111 equatorial upwelling off Gabon, *Geochim. Cosmochim. Acta*, 66, 4247-4259, 2002.
- 2112 Planavsky, N. J., Cole, D. B., Isson, T. T., Reinhard, C. T., Crockford, P. W., Sheldon, N. D., and Lyons, T.  
2113 W.: A case for low atmospheric oxygen levels during Earth's middle history, *Emerging Topics in Life  
2114 Sciences*, 2, 149-159, 2018.
- 2115 Planavsky, N. J., Cole, D. B., Reinhard, C. T., Diamond, C., Love, G. D., Luo, G., Zhang, S., Konhauser, K.  
2116 O., and Lyons, T. W.: No evidence for high atmospheric oxygen levels 1,400 million years ago, *Proc. Natl  
2117 Acad. Sci. USA*, 113, E2550-E2551, 2016.



- 2118 Prentice, I. C., Farquhar, G. D., Fasham, M. J. R., Goulden, M. L., Heimann, M., Jaramillo, V. J., Kheshgi, H.  
2119 S., Le Quere, C., Scholes, R. J., and Wallace, D. W. R.: The carbon cycle and atmospheric carbon dioxide.  
2120 In: *Climate Change 2001: the Scientific Basis*, Houghton, J. T., Ding, Y., Griggs, D. J., Noguer, N., van  
2121 der Linden, P. J., Xiaosu, D., Maskell, K., and Johnson, C. A. (Eds.), Cambridge University Press, New  
2122 York, 2001.
- 2123 Quigg, A., Finkel, Z. V., Irwin, A. J., Rosenthal, Y., Ho, T.-Y., Reinfelder, J. R., Schofield, O., Morel, F. M.  
2124 M., and Falkowski, P. G.: The evolutionary inheritance of elemental stoichiometry in marine  
2125 phytoplankton, *Nature*, 425, 291-294, 2003.
- 2126 Raiswell, R. and Canfield, D. E.: The Iron Biogeochemical Cycle Past and Present, *Geochemical Perspectives*,  
2127 1, 1-2, 2012.
- 2128 Raynaud, D., Jouzel, J., Barnola, J. M., Chappellaz, J., Delmas, R. J., and Lorius, C.: The Ice Record of  
2129 Greenhouse Gases, *Science*, 259, 926-934, 1993.
- 2130 Redfield, A. C., Ketchum, B. H., and Richards, F. A.: The influence of organisms on the composition of sea-  
2131 water. In: *The Sea*, Hill, M. N. (Ed.), Interscience Publishers, New York, 1963.
- 2132 Reimers, C. E., Jahnke, R. A., and McCorkle, D. C.: Carbon fluxes and burial rates over the continental slope  
2133 and rise off central California with implications for the global carbon cycle, *Glob. Biogeochem. Cycles*, 6,  
2134 199-224, 1992.
- 2135 Reinhard, C. T., Olson, S. L., Kirtland Turner, S., Pälke, C., Kanzaki, Y., and Ridgwell, A.: Oceanic and  
2136 atmospheric methane cycling in the cGENIE Earth system model – release v0.9.14, *Geosci. Model Dev.*,  
2137 13, 5687-5706, 2020.
- 2138 Reinhard, C. T., Olson, S. L., Schwieterman, E. W., and Lyons, T. W.: False Negatives for Remote Life  
2139 Detection on Ocean-Bearing Planets: Lessons from the Early Earth, *Astrobiology*, 17, 287-297, 2017a.
- 2140 Reinhard, C. T., Planavsky, N. J., Gill, B. C., Ozaki, K., Robbins, L. J., Lyons, T. W., Fischer, W. W., Wang,  
2141 C., Cole, D. B., and Konhauser, K. O.: Evolution of the global phosphorus cycle, *Nature*, 541, 386-389,  
2142 2017b.
- 2143 Ridgwell, A. and Hargreaves, J. C.: Regulation of atmospheric CO<sub>2</sub> by deep-sea sediments in an Earth system  
2144 model, *Glob. Biogeochem. Cycles*, 21, GB2008, 2007.
- 2145 Romaniello, S. J. and Derry, L. A.: An intermediate-complexity model for simulating marine biogeochemistry  
2146 in deep time: Validation against the modern global ocean, *Geochem. Geophys. Geosyst.*, 11, Q08001, 2010.
- 2147 Rowe, G. T., Morse, J., Nunnally, C., and Boland, G. S.: Sediment community oxygen consumption in the  
2148 deep Gulf of Mexico, *Deep Sea Research Part II: Topical Studies in Oceanography*, 55, 2686-2691, 2008.
- 2149 Ruttenger, K. C.: The Global Phosphorus Cycle. In: *Treatise on Geochemistry*, Turekian, K. K. (Ed.),  
2150 Pergamon, Oxford, 2003.
- 2151 Ruttenger, K. C.: Reassessment of the oceanic residence time of phosphorus, *Chem. Geol.*, 107, 405-409,  
2152 1993a.
- 2153 Ruttenger, K. C.: Reassessment of the oceanic residence time of phosphorus, *Chem. Geol.*, 107, 405-409,  
2154 1993b.
- 2155 Sachs, O., Sauter, E. J., Schlüter, M., Rutgers van der Loeff, M. M., Jerosch, K., and Holby, O.: Benthic  
2156 organic carbon flux and oxygen penetration reflect different plankton provinces in the Southern Ocean,  
2157 *Deep Sea Research Part I: Oceanographic Research Papers*, 56, 1319-1335, 2009.
- 2158 Sagan, C., Thompson, W. R., Carlson, R., Gurnett, D., and Hord, C.: A search for life on Earth from the  
2159 Galileo spacecraft, *Nature*, 365, 715-721, 1993.



- 2160 Sarmiento, J. L. and Gruber, N.: Ocean biogeochemical dynamics, Princeton University Press, 2006.
- 2161 Sarmiento, J. L. and Toggweiler, J. R.: A new model for the role of the oceans in determining atmospheric  
2162  $P_{CO_2}$ , *Nature*, 308, 621-624, 1984.
- 2163 Schenau, S. J. and De Lange, G. J.: Phosphorus regeneration vs. burial in sediments of the Arabian Sea, *Marine*  
2164 *Chemistry*, 75, 201-217, 2001.
- 2165 Schlesinger, W. H. and Bernhardt, E. S.: The Global Cycles of Sulfur and Mercury. In: *Biogeochemistry*  
2166 (Third Edition), Academic Press, Boston, 2013.
- 2167 Schwieterman, E. W., Kiang, N. Y., Parenteau, M. N., Harman, C. E., DasSarma, S., Fischer, T. M., Arney,  
2168 G. N., Hartnett, H. E., Reinhard, C. T., Olson, S. L., Meadows, V. S., Cockell, C. S., Walker, S. I., Grenfell,  
2169 J. L., Hegde, S., Rugheimer, S., Hu, R., and Lyons, T. W.: Exoplanet Biosignatures: A Review of Remotely  
2170 Detectable Signs of Life, *Astrobiology*, 18, 663-708, 2018.
- 2171 Shaffer, G.: Phosphate pumps and shuttles in the Black Sea, *Nature*, 321, 515-517, 1986.
- 2172 Shaffer, G., Malskær Olsen, S., and Pepke Pedersen, J. O.: Presentation, calibration and validation of the low-  
2173 order, DCESS Earth System Model (Version 1), *Geosci. Model Dev.*, 1, 17-51, 2008.
- 2174 Shaffer, G. and Sarmiento, J. L.: Biogeochemical cycling in the global ocean: 1. A new, analytical model with  
2175 continuous vertical resolution and high-latitude dynamics, *J. Geophys. Res.*, 100, 2659-2672, 1995.
- 2176 Sharoni, S. and Halevy, I.: Geologic controls on phytoplankton elemental composition, *Proc. Natl Acad. Sci.*  
2177 *USA*, 119, e2113263118, 2022.
- 2178 Siegenthaler, U. and Wenk, T.: Rapid atmospheric  $CO_2$  variations and ocean circulation, *Nature*, 308, 624-  
2179 626, 1984.
- 2180 Sleep, N. H.: Dioxygen over geological time. In: *Metal ions in biological systems*, Sigel, A., Sigel, H., and  
2181 Sigel, R. K. O. (Eds.), Taylor & Francis Group, Boca Raton, 2005.
- 2182 Slomp, C. P., Thomson, J., and de Lange, G. J.: Enhanced regeneration of phosphorus during formation of the  
2183 most recent eastern Mediterranean sapropel (S1), *Geochim. Cosmochim. Acta*, 66, 1171-1184, 2002.
- 2184 Slomp, C. P. and Van Cappellen, P.: The global marine phosphorus cycle: sensitivity to oceanic circulation,  
2185 *Biogeosciences*, 4, 155-171, 2007.
- 2186 Sloyan, B. M.: Spatial variability of mixing in the Southern Ocean, *Geophys. Res. Lett.*, 32, L18603, 2005.
- 2187 Soulet, G., Hilton, R. G., Garnett, M. H., Roylands, T., Klotz, S., Croissant, T., Dellinger, M., and Le  
2188 Bouteiller, C.: Temperature control on  $CO_2$  emissions from the weathering of sedimentary rocks, *Nat.*  
2189 *Geosci.*, 14, 665-671, 2021.
- 2190 Southam, J. R., Peterson, W. H., and Brass, G. W.: Dynamics of anoxia, *Palaeogeogr. Palaeoclimatol.*  
2191 *Palaeoecol.*, 40, 183-198, 1982.
- 2192 Steefel, C. I. and MacQuarrie, K. T. B.: Approaches to modeling of reactive transport in porous media,  
2193 *Reviews in Mineralogy and Geochemistry*, 34, 85-129, 1996.
- 2194 Suess, E.: Particulate organic carbon flux in the oceans—surface productivity and oxygen utilization, *Nature*,  
2195 288, 260-263, 1980.
- 2196 Tang, D., Shi, X., Wang, X., and Jiang, G.: Extremely low oxygen concentration in mid-Proterozoic shallow  
2197 seawaters, *Precambrian Res.*, 276, 145-157, 2016.
- 2198 Tarhan, L. G., Droser, M. L., Planavsky, N. J., and Johnston, D. T.: Protracted development of bioturbation  
2199 through the early Palaeozoic Era, *Nat. Geosci.*, 8, 865, 2015.
- 2200 Tarpgaard, I. H., Røy, H., and Jørgensen, B. B.: Concurrent low- and high-affinity sulfate reduction kinetics  
2201 in marine sediment, *Geochim. Cosmochim. Acta*, 75, 2997-3010, 2011.



- 2202 The LUVOIR Team: Mission Concept Study Final Report. In: arXiv e-prints, 2019.
- 2203 Tostevin, R., Turchyn, A. V., Farquhar, J., Johnston, D. T., Eldridge, D. L., Bishop, J. K. B., and McIlvin, M.:  
2204 Multiple sulfur isotope constraints on the modern sulfur cycle, *Earth Planet. Sci. Lett.*, 396, 14-21, 2014.
- 2205 Tromp, T. K., Van Cappellen, P., and Key, R. M.: A global model for the early diagenesis of organic carbon  
2206 and organic phosphorus in marine sediments, *Geochim. Cosmochim. Acta*, 59, 1259-1284, 1995.
- 2207 Tsunogai, S. and Noriki, S.: Particulate fluxes of carbonate and organic carbon in the ocean. Is the marine  
2208 biological activity working as a sink of the atmospheric carbon?, *Tellus B: Chemical and Physical*  
2209 *Meteorology*, 43, 265-266, 1991.
- 2210 Turchyn, A. V. and Schrag, D. P.: Cenozoic evolution of the sulfur cycle: Insight from oxygen isotopes in  
2211 marine sulfate, *Earth Planet. Sci. Lett.*, 241, 763-779, 2006a.
- 2212 Turchyn, A. V. and Schrag, D. P.: Cenozoic evolution of the sulfur cycle: Insight from oxygen isotopes in  
2213 marine sulfate, *Earth Planet. Sci. Lett.*, 241, 763-779, 2006b.
- 2214 Turchyn, A. V. and Schrag, D. P.: Oxygen Isotope Constraints on the Sulfur Cycle over the Past 10 Million  
2215 Years, *Science*, 303, 2004-2007, 2004.
- 2216 Turnewitsch, R. and Pohl, C.: An estimate of the efficiency of the iron- and manganese-driven dissolved  
2217 inorganic phosphorus trap at an oxic/euxinic water column redoxcline, *Glob. Biogeochem. Cycles*, 24,  
2218 GB4025, 2010.
- 2219 Tyrrell, T.: The relative influences of nitrogen and phosphorus on oceanic primary production, *Nature*, 400,  
2220 525-531, 1999.
- 2221 Van Cappellen, P. and Ingall, E. D.: Benthic phosphorus regeneration, net primary production, and ocean  
2222 anoxia: A model of the coupled marine biogeochemical cycles of carbon and phosphorus,  
2223 *Paleoceanography*, 9, 677-692, 1994.
- 2224 Van Cappellen, P. and Ingall, E. D.: Redox Stabilization of the Atmosphere and Oceans by Phosphorus-  
2225 Limited Marine Productivity, *Science*, 271, 493-496, 1996.
- 2226 Van Cappellen, P. and Wang, Y.: Cycling of iron and manganese in surface sediments; a general theory for  
2227 the coupled transport and reaction of carbon, oxygen, nitrogen, sulfur, iron, and manganese, *Am. J. Sci.*,  
2228 296, 197-243, 1996.
- 2229 van de Velde, S. J., Hülse, D., Reinhard, C. T., and Ridgwell, A.: Iron and sulfur cycling in the cGENIE.muffin  
2230 Earth system model (v0.9.21), *Geosci. Model Dev.*, 14, 2713-2745, 2021.
- 2231 Volk, T. and Hoffert, M. I.: Ocean carbon pumps: Analysis of relative strengths and efficiencies in ocean-  
2232 driven atmospheric CO<sub>2</sub> changes. In: *The Carbon Cycle and Atmospheric CO<sub>2</sub>: Natural Variations Archean*  
2233 *to Present*, 1985.
- 2234 Walker, J. C. G.: *Evolution of the atmosphere*, Macmillan, New York, 1977.
- 2235 Walker, J. C. G. and Brimblecombe, P.: Iron and sulfur in the pre-biologic ocean, *Precambrian Res.*, 28, 205-  
2236 222, 1985.
- 2237 Wallmann, K.: Feedbacks between oceanic redox states and marine productivity: A model perspective focused  
2238 on benthic phosphorus cycling, *Glob. Biogeochem. Cycles*, 17, 1084, 2003a.
- 2239 Wallmann, K.: Feedbacks between oceanic redox states and marine productivity: A model perspective focused  
2240 on benthic phosphorus cycling, *Glob. Biogeochem. Cycles*, 17, n/a-n/a, 2003b.
- 2241 Wallmann, K.: Phosphorus imbalance in the global ocean?, *Glob. Biogeochem. Cycles*, 24, GB4030, 2010a.
- 2242 Wallmann, K.: Phosphorus imbalance in the global ocean?, *Glob. Biogeochem. Cycles*, 24, n/a-n/a, 2010b.



- 2243 Wang, W.-L., Moore, J. K., Martiny, A. C., and Primeau, F. W.: Convergent estimates of marine nitrogen  
2244 fixation, *Nature*, 566, 205-211, 2019.
- 2245 WebBook, N. C.: NIST Chemistry WebBook. 2022.
- 2246 Westrich, J. T. and Berner, R. A.: The role of sedimentary organic matter in bacterial sulfate reduction: The  
2247 G model tested, *Limnology and Oceanography*, 29, 236-249, 1984.
- 2248 Wheat, C. G., Feely, R. A., and Mottl, M. J.: Phosphate removal by oceanic hydrothermal processes: An  
2249 update of the phosphorus budget in the oceans, *Geochim. Cosmochim. Acta*, 60, 3593-3608, 1996.
- 2250 Wheat, C. G., McManus, J., Mottl, M. J., and Giambalvo, E.: Oceanic phosphorus imbalance: Magnitude of  
2251 the mid-ocean ridge flank hydrothermal sink, *Geophys. Res. Lett.*, 30, 2003.
- 2252 Woodward, F. I.: Global primary production, *Current Biology*, 17, R269-R273, 2007.
- 2253 Wortmann, U. G. and Paytan, A.: Rapid Variability of Seawater Chemistry Over the Past 130 Million Years,  
2254 *Science*, 337, 334-336, 2012.
- 2255 Yakushev, E. V. and Neretin, L. N.: One-dimensional modeling of nitrogen and sulfur cycles in the aphotic  
2256 zones of the Black and Arabian Seas, *Glob. Biogeochem. Cycles*, 11, 401-414, 1997.
- 2257 Yakushev, E. V., Pollehne, F., Jost, G., Kuznetsov, I., Schneider, B., and Umlauf, L.: Analysis of the water  
2258 column oxic/anoxic interface in the Black and Baltic seas with a numerical model, *Marine Chemistry*, 107,  
2259 388-410, 2007.
- 2260 Yamanaka, Y. and Tajika, E.: The role of the vertical fluxes of particulate organic matter and calcite in the  
2261 oceanic carbon cycle: Studies using an ocean biogeochemical general circulation model, *Glob.  
2262 Biogeochem. Cycles*, 10, 361-382, 1996.
- 2263 Yao, W. and Millero, F.: The chemistry of the anoxic waters in the Framvaren Fjord, Norway, *Aquatic  
2264 Geochemistry*, 1, 53-88, 1995.
- 2265 Yaroshevsky, A. A.: Abundances of chemical elements in the Earth's crust, *Geochem. Int.*, 44, 48-55, 2006.
- 2266 Zabel, M., Dahmke, A., and Schulz, H. D.: Regional distribution of diffusive phosphate and silicate fluxes  
2267 through the sediment–water interface: the eastern South Atlantic, *Deep Sea Research Part I:  
2268 Oceanographic Research Papers*, 45, 277-300, 1998.
- 2269 Zhang, S., Wang, X., Wang, H., Bjerrum, C. J., Hammarlund, E. U., Dahl, T. W., and Canfield, D. E.: Reply  
2270 to Planavsky et al.: Strong evidence for high atmospheric oxygen levels 1,400 million years ago, *Proc.  
2271 Natl Acad. Sci. USA*, 113, E2552-E2553, 2016.
- 2272 Zhao, M., Zhang, S., Tarhan, L. G., Reinhard, C. T., and Planavsky, N.: The role of calcium in regulating  
2273 marine phosphorus burial and atmospheric oxygenation, *Nature Commun.*, 11, 2232, 2020.
- 2274
- 2275